Skoltech

Skolkovo Institute of Science and Technology

Skolkovo Institute of Science and Technology

SIMULATION OF THE MECHANISMS OF SOLID-SOLID PHASE TRANSITIONS

Doctoral Thesis

by

ARTEM I. SAMTSEVICH

DOCTORAL PROGRAM IN MATERIALS SCIENCE AND ENGINEERING

Supervisor
Professor Artem R. Oganov

Moscow - 2021

I hereby declare that the work presented in this thesis was carried out by myself at Skolkovo Institute of Science and Technology, Moscow, except where due acknowledgment is made, and has not been submitted for any other degree.

<div align="center">
Candidate (Artem I. Samtsevich)
Supervisor (Prof. Artem R. Oganov)
</div>

ABSTRACT

Solid-solid transitions are common in nature and important for basic science and technology. Thus, it is crucial to understand these processes at the atomic level. Due to the lack of experimental data about kinetics, modeling these processes on an atomic level is a hot topic in computational chemistry. The simulation techniques must be used to understand such events. From the chemical point of view, such transformations are the transitions between basins on a high-dimensional free energy landscape (FES). For this reason, the exploration of the FES requires large computational resources for such methods as molecular dynamics and Monte Carlo, which are inefficient for studying phase transitions and other activated processes, forcing scientists to develop new approaches or upgrade the existing ones.

Generally, transition state theory (TST) helps one to estimate the reaction rate constants for particular transformation and harmonic approximation to TST transforms this problem into another one - seeking first-order saddle points on the FES, which are called transition states (TS). If two structures are known, the chain-of-states methods help to locate TS and the nudged elastic band (NEB) and NEB-based methods are the most common of them. However, these methods have a problem — if the initial pathway is not close to the minimum energy pathway (MEP), the NEB optimization will highly likely not converge to the correct pathway. Generation of the initial pathway transforms to another problem of mapping crystal structures onto each other, which can be done by purely geometrical methods or by the recently proposed topological method. Both approaches are complementary to each other and generate a diverse set of mappings. When the mappings are defined, the initial pathways can be generated and optimized by the chain-of-states method. Among all optimized pathways, the MEP should be chosen. All these steps are merged into the workflow implemented in the USPEX code.

The following transitions on an atomic level have been investigated using the proposed workflow: from $Pnma$-CrN to newly predicted hard $P\bar{6}m2$-CrN phase, from $Pmmn$-CaCO$_3$ (postaragonite) phase to $P2_1/c$-CaCO$_3$, from $I4_1/amd$-WB (α-WB) to newly predicted $P\bar{4}2_1m$-WB and andalusite – kyanite – sillimanite transitions in Al$_2$SiO$_5$.

LIST OF PUBLICATIONS

Thesis work

1. Kvashnin, A. G., Oganov, A. R., **Samtsevich, A. I.**, & Allahyari, Z. (2017). Computational search for novel hard chromium-based materials. **The journal of physical chemistry letters**, 8(4), 755-764.

2. Lobanov, Sergey S., Xiao Dong, Naira S. Martirosyan, **Artem I. Samtsevich**, Vladan Stevanovic, Pavel N. Gavryushkin, Konstantin D. Litasov et al. "Raman spectroscopy and X-ray diffraction of sp^3-$CaCO_3$ at lower mantle pressures." **Physical Review B** 96, no. 10 (2017): 104101.

3. Kvashnin, A. G., & **Samtsevich, A. I.** (2020). Phase Transitions in Tungsten Monoborides. **JETP Letters**, 111, 343-349.

4. **Samtsevich A. I.**, Oganov, A. R. (2021). Mechanisms of phase transitions in Al_2SiO_5 phases. **Zapiski RMO (Proceedings of the Russian Mineralogical Society) [Accepted]**

Other publications

1. Khrapov, N. P., Rozen, V. V., **Samtsevich, A. I.**, Posypkin, M. A., Sukhomlin, V. A., & Oganov, A. R. (2018). Using virtualization to protect the proprietary material science applications in volunteer computing. Open Engineering, 8(1), 57-60.

2. Tantardini, C., Michalchuk, A. A., **Samtsevich, A. I.**, Rota, C., & Kvashnin, A. G. (2020). The Volumetric Source function: Looking inside van der Waals interactions. **Scientific reports**, 10(1), 1-10.

ACKNOWLEDGMENTS

PERSONAL CONTRIBUTION

The idea of using the topological approach for mapping structures onto each other belongs to the author's supervisor, Prof. Artem R. Oganov and Prof. Vladislav Blatov. The author implemented the code for the topology-based initial pathway generation. The author adapted this implementation to be used as a part of the VCNEB method in the USPEX code.

The author adopted a geometrical approach for the initial pathway generation to be used as a part of the VCNEB method in the USPEX code.

Topology-based and geometrical approaches for the initial pathway generation have been combined with the VCNEB method in USPEX code as a workflow by the author under the supervision of Prof. Artem R. Oganov.

The author used the implemented method and performed all the calculations of phase transitions in considered solids.

All the discussed results in Chapter 4 are analyzed by the author under the supervision of Prof. Artem R. Oganov.

THESIS OUTLINE

The first Chapter of the Thesis introduces the reader to the rare events and phase transitions in solids. Mainly, it presents a literature review of the studies dedicated to the calculations and experimental investigations of phase transitions. Beside that, it presents different ways to describe the physical mechanism of the transition events and their types.

Next, Chapter 2 provides a complete picture of the mathematical interpretation of the phase transitions, particularly describing phase transition on energy landscape and introducing the transition state theory that is massively used. At the end of the chapter, I show how these approaches provide the basis for phase transitions simulation.

Then, Chapter 3 familiarizes the reader with the progress in existing simulation techniques, appropriate for investigating the phase transitions in solids. The end states the research problem addressed in the Thesis.

Chapter 4 thoroughly depicts all the steps of the developed and adapted methods. The chapter describes the general methodology for the minimal energy pathway search, which consists of three steps. First, it describes how two crystal structures can be mapped onto each other by the geometrical and topological approaches. The first method operates with lattice parameters and atomic positions. The second method presents structures as a periodic graph of interatomic contacts and searches for the optimal topological transformation of the initial structure into the final one. When the mapping is defined, it is presented how to generate the initial pathway. After that, the description goes to the final step, which is the pathway optimization performed with the variable cell nudged elastic band (VCNEB) method. At the end of the chapter, the workflow that generalizes all presented methods and describes the transition mechanism on an atomic level is presented.

Chapter 5 presents the results of the proposed workflow. This part of the Thesis starts with the whole scheme of the developed method. Then, it provides the outcomes of the usage of each step, described above, relative to the chosen solid-solid phase transitions: from $Pnma$-CrN to newly predicted hard $P\bar{6}m2$-CrN phase, from $Pmmn$-CaCO$_3$ (postaragonite) phase to $P2_1/c$-CaCO$_3$, from $I4_1/amd$-WB (α-WB) to newly predicted $P\bar{4}2_1m$-WB and andalusite – kyanite – sillimanite transitions in Al$_2$SiO$_5$. After that, all the results are discussed.

Finally, Chapter 6 sums up the conclusions corroborated by the analysis from the previous parts of the Thesis. Besides, this Chapter sheds some light on the existing and emerging problems of presented approaches and proposes possible solutions. Based on all of the information above, I derive several conclusions and suggest a couple of ideas for further improvement.

Table of Contents

1 INTRODUCTION

1.1 Phase transition as a rare event

By "rare event" we mean any dynamical phenomenon occurring with a very low frequency. Interestingly, rare events are seen in many contexts: queue overflow in queuing theory [1], biochemical switching [2], extinction of diseases [3], or populations [4], slow chemical reactions [5], first-order phase transitions [6] and journeys deep into labyrinths [7]. In the fields of condensed matter physics and materials science, there are so many activated processes that can be called "rare events" – for example, crystallization [8,9], chemical reactions in solution, protein folding, isomerization, enzymatic reactions, diffusion in porous media, structural phase transitions and many more processes. The main common feature of all these processes is that they happen on a long time scale compared to the molecular timescale. Experimental observation of these processes on an atomic level is not possible at this moment because the dynamical evolution of a system consists of wandering within a potential basin, punctuated by occasional transitions to other potential basins. Furthermore, these transitions are infrequent in the sense that the average time between events is many ($\sim 10^{10}$-10^{15}) atomic vibration periods. Knowing the mechanisms and the kinetics of these processes has fundamental importance and can provide fruitful insights into practical applications.
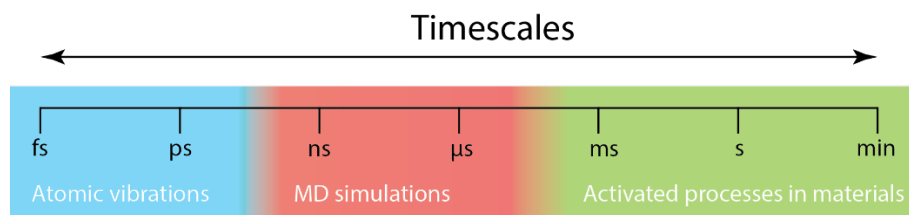
Figure 1.1. Timescale gap between atomic vibrations, the activated processes that govern many materials properties and what can be simulated directly with molecular dynamics (MD).

The gap between atomic vibration time and the activated processes of interest for materials is schematically shown in Figure 1.1. The central region on figure illustrates the well-known molecular dynamics (MD) approach and its timescale. The main problem in activated processes can be described by a good illustration depicted in Figure 1.2. The configurational space of a prototypical system has two energy basins A and B and each of these basins corresponds to a specific region of the long-lived state on the configurational space. The system blindly wanders, forming the basin A and spends the majority of its time there. Only when the system acquires kinetic energy that is large enough to cross over the energy barrier, it will reach another long-lived region, i.e. basin B. For equilibrium statistics, only regions A and B are relevant. In the case of $A \rightarrow B$ dynamics, the most important becomes the buffer region separating A from B. Once the buffer region is crossed, all kinetic energy of the system, which is large compared to $k_B T$, is transferred to different degrees of freedom. As a result, the system

will be very fast relaxed into another long-lived region. Therein, the system again fluctuates within microstates and forms the basin B.
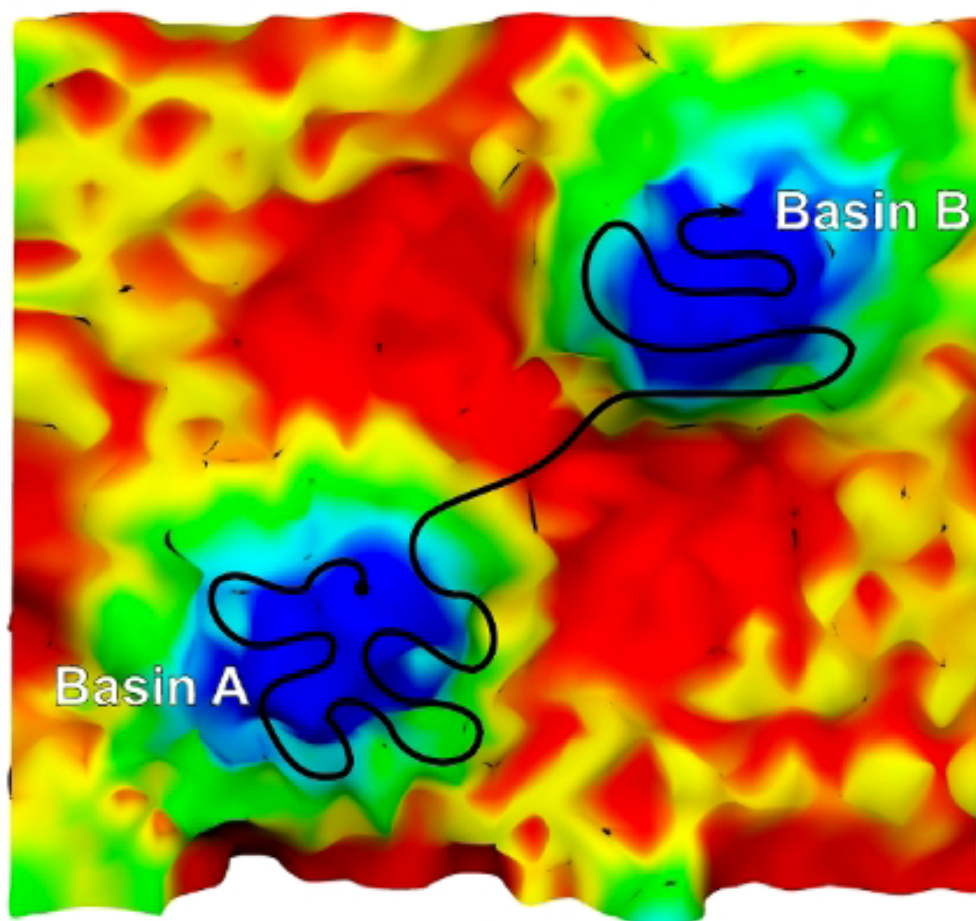
Figure 1.2. Schematic representation of a configuration space with two basins of long-lived states A and B (blue regions). The system spends the majority of the time wandering within basins A and B. The dynamical trajectory of a system corresponds to the fleeting cross over from A to B. Blue, green, yellow, and red colors are ordered in an ascending energy scale (Reprinted from Ref [10]).

Energy transfer between different degrees of freedom plays an important role in barrier crossing dynamics [11]. As shown in Figure 1.3, the periods of time that system wanders within each of basins A and B, are not equal. Also, these periods are distinctly longer than the period of time needed to cross over, so the transitions occur only rarely. In condensed matter physics, the bottlenecks of configurational space correspond to the nucleation of a new phase. Another example of a rare event in condensed matter physics is the atom hopping between different interstitial sites in a solid. The energy required to locally distort the lattice structure fully determines the nature of the bottleneck. The distortion of the lattice causes the opening of possible pathways between interstitial sites.
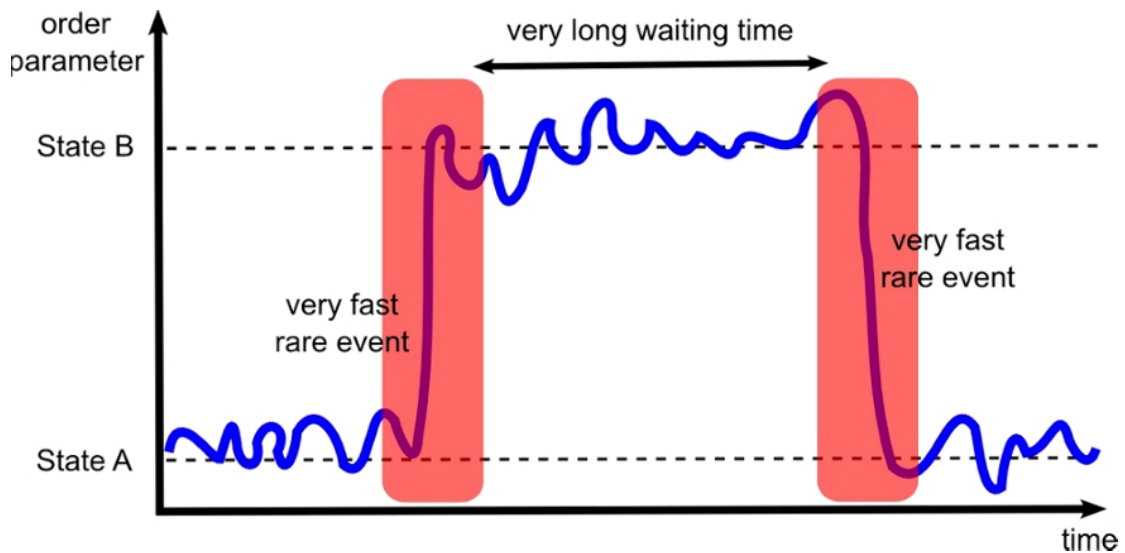
Figure 1.3. Time evolution of a dynamical trajectory of system crossing from state A to state B. Residence times spent in the states are very long compared to the time needed to switch between states. A and B can be distinguished using an order parameter like the coordination number of an atom (Reprinted from Ref [10]).

1.2 Solid Phase Transitions

Phase transitions attract scientists to unravel the essence and nature of these processes. We can see the discontinuous change of material properties during phase transitions, such as volume, density, elasticity, electric, magnetic, optical, etc. Phase transitions in solids are accompanied by a change of its structure, which means a change of atomic coordinates, occupied positions, lattice parameters and, as a result, the space group of the structure. Understanding the mechanisms of these transformations plays a key role in discovering new phases with new (maybe extraordinary) properties. Thus, solid-solid phase transition is still one of the most interesting areas for research in materials science and condensed matter physics.

Several theories exist, which allow us to understand and describe the essence of these processes. Based on the transition's specific aspects, all approaches for the phase transition investigation can be divided into three branches: thermodynamic, structural and kinetic, as illustrated in Figure 1.4.
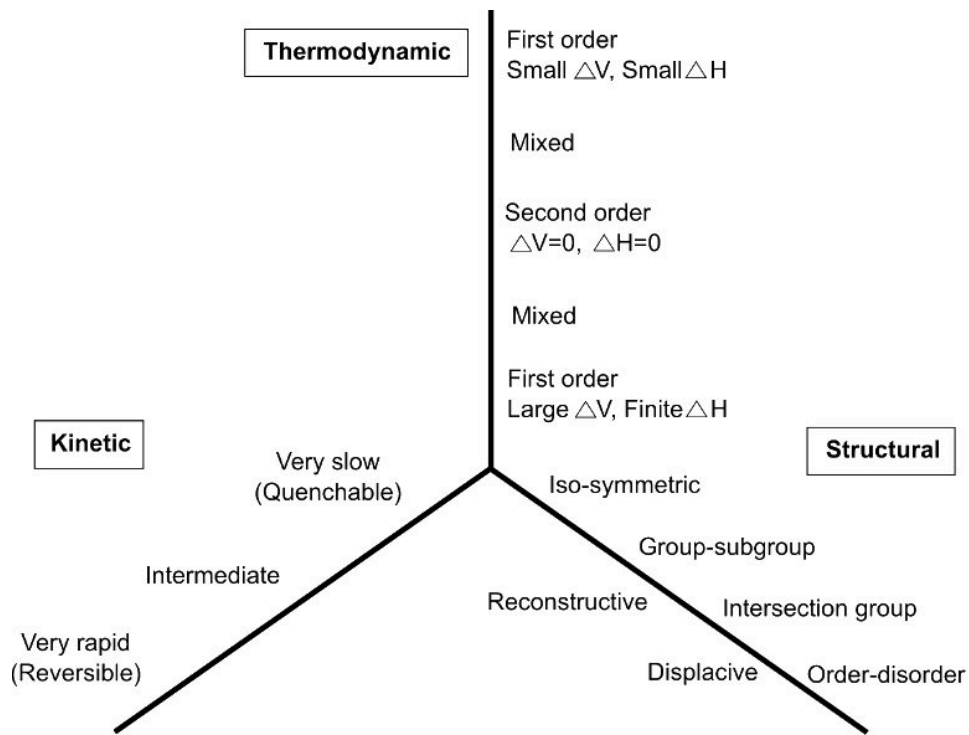
Figure 1.4 Different aspects of classification of phase transitions (reprinted from Ref. [12]).

Thermodynamic approach

A thermodynamically stable phase can be pushed out of stability by changing one or several external parameters, such as temperature, pressure, electric or magnetic fields or even some mechanical forces. The resulting stress on the system causes changes in its structure and induces a transformation. Herein, we refer to the Ehrenfest study [13], which introduced the order of phase transition.

The *order of phase transitions* is determined by the lowest derivative of the free energy that is discontinuous during the transition. At a *first-order phase transition,* at least one of the first derivatives of the Gibbs free energy G experiences a discontinuous change. At a *second-order phase transition*, the first derivatives of the energy, like volume and entropy, experience a continuous variation. At the same time, at least one of Gibbs free energy's second derivatives exhibits a discontinuity. Logically, a discontinuity appears for the first time at the *n*-th derivative at a *phase transition of n_{th} order*. However, examples of transitions with orders higher than two are unknown).

For example, as first-order transitions are classified many phase transitions in gases, liquids and solids. These transitions involve a discontinuous change in density or volume (the first derivative of the free energy with respect to pressure). Another type is continuous in the first derivative but exhibits discontinuity in a second derivative of the free energy, thus named second-order phase transitions. An example of second order phase transition is the ferromagnetic-paramagnetic phase transitions. Here, the magnetization, which is the first derivative of the free energy with respect to the applied

magnetic field strength, increases continuously from zero below the Curie temperature, the magnetic susceptibility, the second derivative of the free energy with the field, changes discontinuously.

The approach proposed by Ehrenfest has become very useful for the phase transitions classification. However, some limitations were unknown at the time of theory formulation, as in the cases of continuous transformations, when the derivative of free energy diverges. For instance, in some ferromagnetic transitions, the heat capacity diverges to infinity [14].

Ehrenfest's classification is based on macroscopic measured variables and purely thermodynamic arguments. It does not take into account consideration of the interatomic interactions and structures of the substances and ignores the singularity of the free energy in case of continuous (2nd order) transitions, which has been solved by the extension made by Pippard [15,16]. Also, Roy has reviewed these classifications systematically in 1973 [17]. He has identified four principal approaches to the problem by classifying phase transitions based on kinetic, thermodynamic classification, thermochemical, and structural considerations.

Kinetic approach

The kinetic approach starts from the early work of Le Chatelier and is focused on the activation energy and the transition rate. The kinetic approach can be used only for the consideration of transition between polymorphs of a given compound. Herein, phase transitions can be divided into two categories. The first – sluggish phase transitions are characterized by very high activation energy. A large hysteresis characterizes these transitions and the speed of the transition is very low. The second type of transition is called rapid or non-quenchable. According to this, various behaviors are possible: if the transition is irreversible and proceeds in only one direction, it is monotropic behavior. In case if the transition is reversible, this is enantiotropic behavior. Finally, I refer to the more detailed review of kinetics approaches [12].

However, no real classification scheme can be based on this parameter since it does not treat any basic property of either of the two phases. Moreover, as experimental capabilities grow, what is regarded as 'non-quenchable' today may be established to be quenchable tomorrow. However, some recent research on this aspect has pointed out that with the right combination of the structural as well as the kinetic aspect an acceptable criterion of classification may emerge.

Structural approach

The structural approach can be applied to the polymorphic phases before and after the transformation. The experimental evidence of atomic motions or other processes that occur during the transition cannot be obtained. This approach has been proposed by Buerger [18] and according to his study, phase transitions can be classified as:

(1) **Reconstructive phase transitions**: The atoms are rearranged and chemical bonds are broken during the transition. Such transformations are always first-order transitions.

Thermodynamically, first-order free energy derivatives (entropy and volume) are discontinuous as a result of the change in the atomic environment at the transition. The activation energies of such kind of transitions are high. Such transitions occur in metals, alloys and insulating materials [19].

(2) **Displacive phase transitions**: Atoms experience small shifts and without breakage of the bond network. Here, symmetry space groups of reactant and product structures have a direct group-subgroup relationship and the required activation energy tends to be low. Displacive transitions can be first- or second-order phase transitions. Such transformations are often found in shape-memory alloys [20–22], giant magnetocaloric materials [23,24] and others.

(3) **Order–disorder transitions**: Different kinds of atoms that statistically occupy the same crystallographic point orbit in a crystal become ordered in different orbits or vice versa. Alternatively, molecules that statistically take several orientations become ordered in one orientation.

Frequently, what category of a phase transition must be assigned is a tricky question. However, the qualitative kind of the classification does not always permit a clear assignment. There is no consensus in the literature, of how exactly displacive transitions should be determined and how they should be delimited on the one hand from reconstructive and order-disordered transitions on the other hand. For example, martensitic transitions widely occur in alloys, ceramics, minerals and inorganic compounds, and related transitions [25,26]. Despite their diffusionless and continuous character, all of these transitions display coordination changes and significant structural distortions [27]. Thus, in the literature, they are classified as reconstructive or as displacive [28]. The atomistic description does not play a key role in understanding the transition type since the distinction between transformation types is rather related to a phenomenological understanding. By all means, presented classification is not unambiguous.

The kinetic and structural approaches are not as strict and accurate as the thermodynamic approach. The unclear criterion in the two qualitative approaches always raises some discrepancy among different studies when defining phase transitions. However, these categorization methods are still meaningful as they provide a phenomenological description of the phase transition.

The approaches described above have a number of limitations that can be avoided by considering the latent heat. According to this, all transitions are divided into two categories similar to the classification made by Ehrenfest [29–31]. The transition is termed first-order, if it involves a change in the latent heat [32]. During the transition, the system either absorbs or releases a large amount of energy without variation in the temperature. In reality, there is no an instantaneous transfer of energy between environment and system. First-order phase transition is associated with *phase*

coexistence. It means that part of the system already has completed the transition to the new phase, while another part still has not. Such a transformation mechanism is known to involve a *nucleation and growth* process. Pressure-induced phase transitions in the solid-state belong to this category. The phase transition is second-order if the continuous model can be used to describe the transformation and no latent heat is associated with the transition.

The thermal vibration of atoms affected by the varying temperature or pressure causes phase fluctuations that occur as random rare events. A stand-alone fluctuation may be associated with a free energy reduction, but it can only survive and grow if there is an energy reduction. The cost associated with the creation of a new phase within another one, the interface energy, is a penalty which becomes smaller as the particle surface to volume ratio decreases. In a metastable system, this leads to the critical size of fluctuation beyond which growth is favored. If the nucleation is not taking place at an impurity or initiated by a foreign element to the system, it is called homogeneous. Homogeneous nucleation is described by classical nucleation theory (CNT) [33] and also by non-classical nucleation theory [34].

In experiments, solid-solid phase transitions have been studied by calorimetry [35], acoustic emission [36], X-ray scattering [37] and transmission electron microscopy [38,39]. The transitions, which occur at high pressure (up to ~600 GPa), can be revealed by advanced experimental techniques, like shock-wave [40] and the Diamond Anvil Cell (DAC) [41]. The shortcoming of these studies is that due to the small spatial and temporal scales, these techniques cannot resolve the initial stage of nucleation. Indeed, the kinetics of transition pathways and associated atomistic transformation mechanisms remain poorly understood. Herein, a main unanswered question about phase transitions in solids concerns whether kinetic pathways follow a martensitic or a diffusive nucleation process [37,38,42,43].

Many experimental studies have been done for phase transitions in colloids, because colloidal particles are micron-sized and can be directly imaged by optical microscopy. Additionally, colloids thermal motions can be tracked by image processing [44].

Compared with crystallization [45], melting [46,47] and glass transitions [48], solid-solid phase transitions in colloidal systems have been scarcely studied [49–55]. To drive a solid-solid transition, the considered colloidal crystal must be tunable, which means be representable in both ways. For example, an electric-field-induced transition between fcc and bct [i] colloidal crystals was reported to be diffusive for fcc-bct, but martensitic for the reverse bct-fcc transition [55]. Solid-solid transitions in tunable colloidal crystals have been achieved in electric- or magnetic- field-driven solid-solid transitions [51,52,54,55]. The rapid displacive martensitic transformations took place in these systems. The dynamical processes of the displacive martensitic transformations have not been studied.

---

[i] fcc- face-centred cubic; bct - body-centred tetragonal

Another type of solid-solid phase transition is much harder to study in an experiment. There is the study of the transition between square and triangular lattices, which is one of the simplest solid-solid transitions without a group–subgroup relation [56,57]. This transition occurs within large crystalline domains, and the dynamics process can be well captured. It was studied how pressure gradient enhances energy barrier crossing and promoted the collective motion of particles, thus resulting in new kinetic behavior. Phase transitions under pressure gradients represent a simple type of non-equilibrium phase transitions, which are poorly understood, yet hugely important for both basic science and technological applications [58].

Reconstructive phase transitions in solids are theoretically difficult because an order parameter cannot be defined easily without a group–subgroup relation in lattice symmetries [19,59]. Solid-solid phase transitions are also difficult to simulate due to the sluggish dynamics [42]. To accelerate transition dynamics, simulations were usually performed in small systems [60], under pressure gradients or even shock waves [61] to overcome the high free-energy barriers.

All above-mentioned classification methods are still meaningful, because they provide a phenomenological description of the phase transition. The understanding of phase transition on an atomistic level might avoid contradictions. But still, the mechanisms that govern phase transitions in solids present substantial challenges for experiment, theory and simulation.

2 THEORETICAL BACKGROUND

2.1   Theories of phase transitions

To precisely understand the phase transition mechanism at the atomic scale, a theoretical calculation may succeed where the experimental observation fails. The experimental study of such processes as solid-solid phase transition is a big problem because these processes are related to "rare events", which appear with very low frequency and cannot be directly investigated at the atomic level. On another side, the current powerful theoretical methods can analyze phase transitions. Mainly, these methods are developed based on the two theory paradigms: Landau theory and Transition State theory, which will be discussed further.

2.1.1 Landau Theory of Continuous Phase Transitions

In 1937 L. D. Landau developed a free energy-based theory, in which he phenomenologically investigated phase transitions in the solid-state for displacive transformations [62,63]. Later, the approach was extended to describe the first-order transition, including reconstructive phase transitions [59].

In the Landau approach, an order parameter η is introduced for the phase transition description. The order parameter η is an appropriate, measurable quantity that contains all the information about the structure along the transition path and extent of structure evolution during the transition. It meant that an order parameter η is apt to account for the essential differences of the phases. The free energy can be expanded as the Taylor series in terms of η and the expansion of the Taylor series is truncated at the lowest order. As a result, the terms of expanded series couple η with other physical quantities (such as temperature, strain or spin direction). Herein, using standard thermodynamic relations, the behavior of η and coupled quantities can be obtained from the free energy. Landau theory has proven to be very robust and effective. As a result, coefficients which were obtained from experimental data fitting, characterized a wide range of fundamental relationships [64].
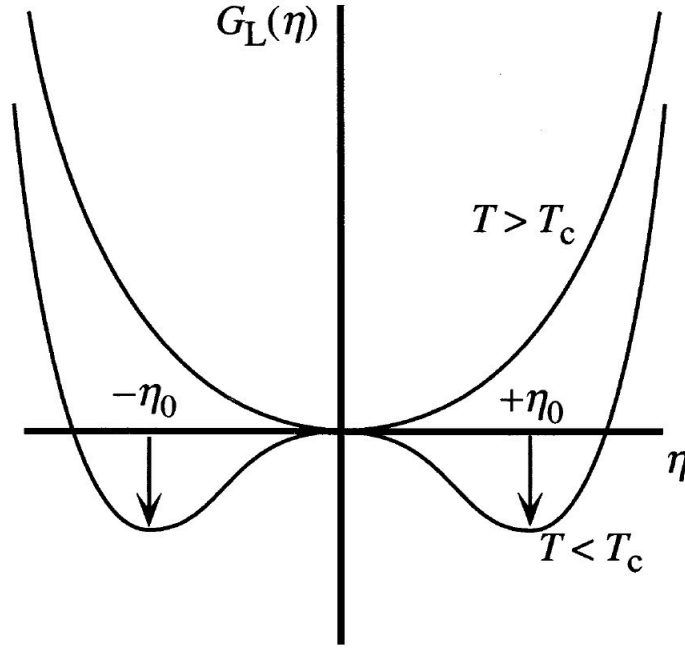
Figure 2.1. Landau free energy for temperatures above and below the transition temperature. The equilibrium value of the order parameter η is given by the minimum of the free energy. At high temperatures $(T \geq T_c)$, there is a single minimum at $\eta = 0$. At low temperatures $(T \ll T_c)$ the free energy has a maximum at $\eta = 0$ and minima at non-zero values of $\eta = \pm\eta_0$ (Reprinted from Ref [65]).

Landau theory relies on the appropriate definition of the order parameter. Once η is defined, the Landau free energy can be presented by following formula:

$$G(\eta) = G_0 + A \cdot \eta^2 + B \cdot \eta^4 + \cdots \tag{2.1}$$

where G_0 is system's free energy for $\eta = 0$ while A and B are constants. For a temperature-induced phase transition, the shape of Landau free energy changes as a function of temperature and pressure, as displayed in Figure 2.1.

For phase transitions in solids, the form of η reflects the system symmetries. In combination with representation theory [66], group-subgroup relationships directly affect the form of η. The concept applies to second-order continuous transformations. In the case of first-order phase transitions, it requires the Landau free energy consideration in a general form, which includes odd terms:

$$G(\eta) = G_0 + A \cdot \eta^2 + \beta \cdot \eta^3 + B \cdot \eta^4 + \cdots \tag{2.2}$$

As a result, secondary minima appear. Moreover, one of them may become global on lowering the critical value of the coupling parameter, e.g., temperature. Considering the phase coexistence, the order parameter discontinuously jumps from 0 to some finite, non-zero value.

While the Landau theory has a mean-field character, it is a significant drawback of this theory. As a result, the condition on the vanishing of η at the critical point will not be fulfilled, because theory

flattens local fluctuations into averages. Due to this, Landau theory does not cover nucleation and growth phenomena.

For the description of the mechanism of first-order phase transitions, there have been presented several improved approaches. Generally, they can be divided into following approaches:

- **The adiabatic approximation**. These approaches investigate the transitions using periodic least-enthalpy calculations [67–69]. The method is based on the exploration of the adiabatic potential energy hypersurface of the transformation configuration space. The search for energetically favored intermediate states is performed assuming conservation of translational symmetry. For the kinetics of the transition characterization, activation volumes are determined and analyzed with respect to pressure variations. However, the use of systems as small as unit cells and the resulting concerted mechanisms is insufficient to capture phase coexistence and nucleation and growth processes.

- **The Free energy surface (FES) approaches.** This type of methods scan the free energy landscape using advanced molecular dynamics simulation or algorithms that perform specific optimization. The most popular is the metadynamics method [70], which pioneered this type and many other methods have been inspired by it. It explores energy landscape using a history-dependent bias potential. The bias potential is constructed as a function of a small number of collective variables (CVs) used to distinguish between all the relevant states of the system. Provided that a CV can be developed for a certain process, it can be studied using metadynamics. Original one uses the system lattice parameter as a CVs. As a result, the bias potential fills energy minima and, hence, shorten the waiting time between minima-to-minima transitions and this bias potential depends on the low number of CVs, so the system evolves to the new state with low efforts. During the metadynamics simulation, on each step, the calculated forces are stored in the simulation's track history. This method avoids revisiting the same valley on the free energy landscape and preventing the fall back to the same minimum. In Figure 2.2, it is shown how the system evolves during the metadynamics simulation. The scan proceeds by flooding free energy minima until the surface is enough to cross over to another local minimum. Metadynamics has been widely used in many scientific fields [71,72] and to calculate the rates of slow processes accurately [73], even in complex systems [74].

  Another important algorithm for energy landscape exploration is called the stochastic surface walking (SSW) method [75]. This method is based on bias-potential-driven dynamics and Metropolis MC sampling. Stationary points are perturbed toward a new configuration through randomly generated modes of displacement and the subsequent construction of a biasing potential [75,76].

- **The common subgroup paradigm**. This approach is helpful in cases when the direct group-subgroup correspondence between structures cannot be obtained. The space groups of both structures are lowered until the common space group will be found. The resulting space groups are then used to generate a common for both structures cell and structures are brought to this cell. As a result, one is capable to map structures onto each other. The transition is then described using the set of degrees of freedom allowed in the common subgroup. The number of possible common space groups that can be used is large and all these possible transformations must be considered. The biggest problem of these methods is that they can only be used for the system with small number of atoms in the unit cell (at maximum – several dozens of atoms), thus nucleation processes are not feasible. The origin of this approach is presented in the study made by H. T. Stokes and D. M. Hatch [77].

- **The common lattice complex principle**. This approach relies on point configurations generated within one type of Wyckoff set forming a lattice complex [78]. The transition may be described as a deformation of a homogeneous sphere packing with a given number of contacts per sphere. Similar to the common subgroup paradigm, the deformation is achieved within a lattice complex which allows for lowering the number of contacts per sphere. Because of the continuous character of the mechanistic model obtained using this method, it suffers from the same limitations as the previous paradigm.
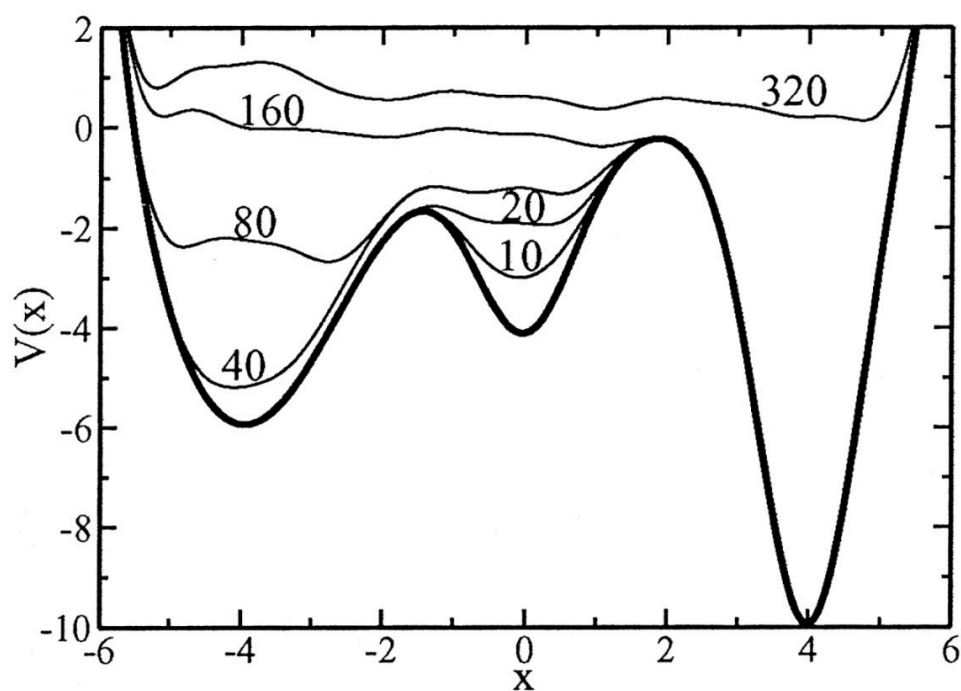
Figure 2.2. The dynamic evolution (thin lines) labeled by the number of dynamical iterations of free energy minima flooding using the metadynamics method (Reprinted from Ref [79]).

For a very long time, capturing the first-order character of the transition has been a huge problem either in the investigation or classification. However, the mean-field methods mentioned above are working well for the continuous transitions and fail to study discontinuous transformations. Since the presented methods provide meaningful information about atomic structures mapping before and after the transition, they still cannot provide any details of nucleation and growth processes. Additionally, it is a not an easy task to choose the representative reaction coordinate that describes the transition. Due to a large number of degrees of freedom in the crystals, usually, reaction coordinates are unknown from the beginning.

All methods that scan the free energy landscape helped to understand the most relevant transition features of this landscape. This kind of methods does not always find the structures that are sought by the simulation because visited minima not always represent the necessary steps of the transition. Moreover, the resulting mechanism does not really represent the atomic movement during the transition and the nucleation process is out of the scope of these methods. Alternatively, in the first-order phase transitions, the atomic motion may have very long trajectories that cannot be traced by the free energy scanning algorithms.

The method for studying first-order phase transitions covering the nucleation and growth processes is the most desired by the scientific community. Such method has been proposed by Bolhuis and Chandler is called transition path sampling (TPS) [80,81]. The presented method performs a Monte Carlo sampling of transition pathways and the resulting pathway with high probability represents the real transition mechanism. TPS proved its efficiency in the investigation of solid-solid phase transitions in A17 $\rightarrow$ A7 transition in black phosphorus [82], solid Ar [83], carbons [84] and many more.

2.2 Energy Landscapes

The structure of an atomic system can be specified by the locations of the atoms in this system. A system has specific energy for a given structure and electronic state. A potential energy surface (PES) describes how the energy of the system in a particular state varies as a function of the atomic structure of the system. Under certain circumstances, the characteristic points of the PES can provide information about the properties of condensed systems [85,86]. Reorganization processes in solids, transport in or on solids and chemical bond cleavage and formation belong to this type of processes.

First, let us consider the system of N atoms of classical mechanical system. Here the structure and dynamics are essentially determined by the potential energy $V(r)$ usually given as a function of the coordinates $r = \{r_1, r_2, \ldots r_{3N}\}$ of all N atoms. Molecular simulations usually use the potential energy that is either modeled as an empirical potential or calculated directly from a solution of the electronic Schrodinger equation. The latter, usually, is solved in the Born–Oppenheimer approximation. This approximation separates the motion of the electrons from the motion of the nuclei because the electrons are much lighter and move much faster than the nuclei. The energy of an atomic system can be obtained by solving the electronic structure problem, where the nuclei are pinned to the fixed positions. This procedure can be repeated for any number of nuclear positions, the energy of a system can be described as a function of the position of the nuclei, thereby yielding a PES.

Figure 2.3 illustrates a simple PES as a hilly landscape with peaks, valleys, and mountain passes. Even though most atomic systems have many more than two geometric variables (*xy*-plane), most of the important features of a PES, such as minima, transition structures and reaction paths, can be represented in such a landscape.
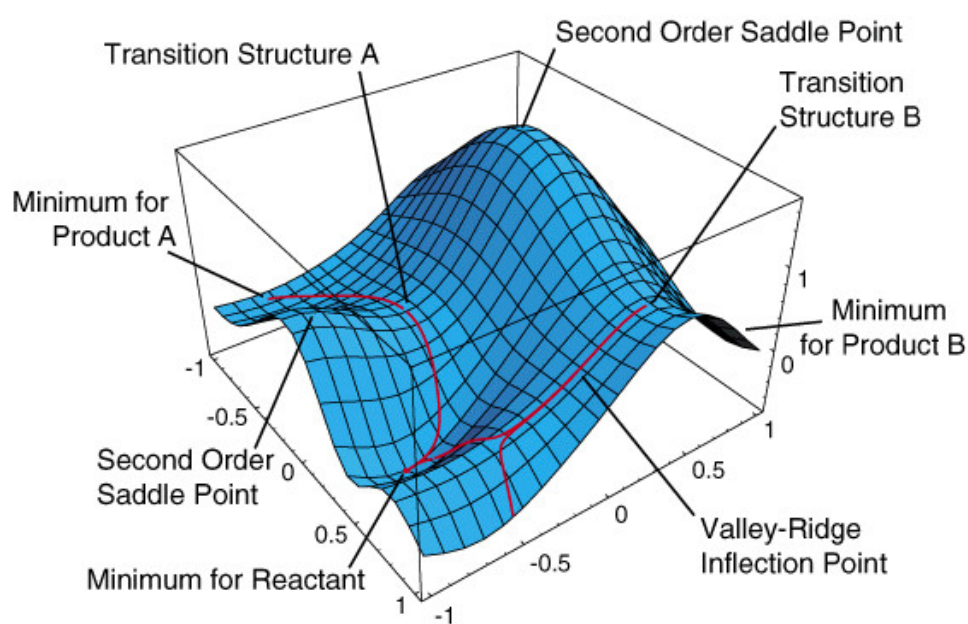
Figure 2.3. Model of potential energy surface, with depicted minima, transition structures, reaction paths, and a valley ridge inflection point. (Reprinted from Ref [87])

The valleys of a potential energy surface represent reactants, intermediates, and products of a reaction. The equilibrium structure is located in the minimum of the valley. The energy of the reaction is the energy difference between the reactant and product valleys minima. The vibrational motion of the system about the reactant and product equilibrium geometries can be used to compute zero-point energy and thermal corrections, which are required for free energy and enthalpy calculation [88]. The reaction path is the lowest energy pathway between the reactant and the product [89]. The transition state (TS) of the reaction is the highest point on the minimal energy reaction pathway. The barrier of the reaction is the energy difference between the TS energy and the reactant energy. From the mathematical perspective, TS is a maximum in the direction along the reaction path that connects reactant and product and a minimum in all other perpendicular directions. Thus, from the mathematical point of view, TS is the first-order saddle point. In Figure 2.3, TS connects two valleys by a mountain pass.

As shown before, for an activated reaction, for the reaction rate estimation, one needs the TS energy and the shape around the TS. The path generated by the steepest descent approach from the TS down to the reactants and to the products is termed the minimum energy pathway (MEP). Any other reaction path that connects reactants and products through intermediate points (if any) describes the reaction mechanism [89].

Another illustration of the potential energy is depicted in Figure 2.4. The elevation in the z-direction corresponds to the potential energy value at a particular configuration r represented by a point in the xy-plane. Although this simple example may assist our imagination, it is crucial to keep in mind that, for typical condensed matter systems, $V(r)$ is a much more complicated function with a vast number of maxima, minima, saddle and singular points. The presented landscape picture is a substantial simplification as the high-dimensional configuration space is represented by one or, at most, two dimensions.
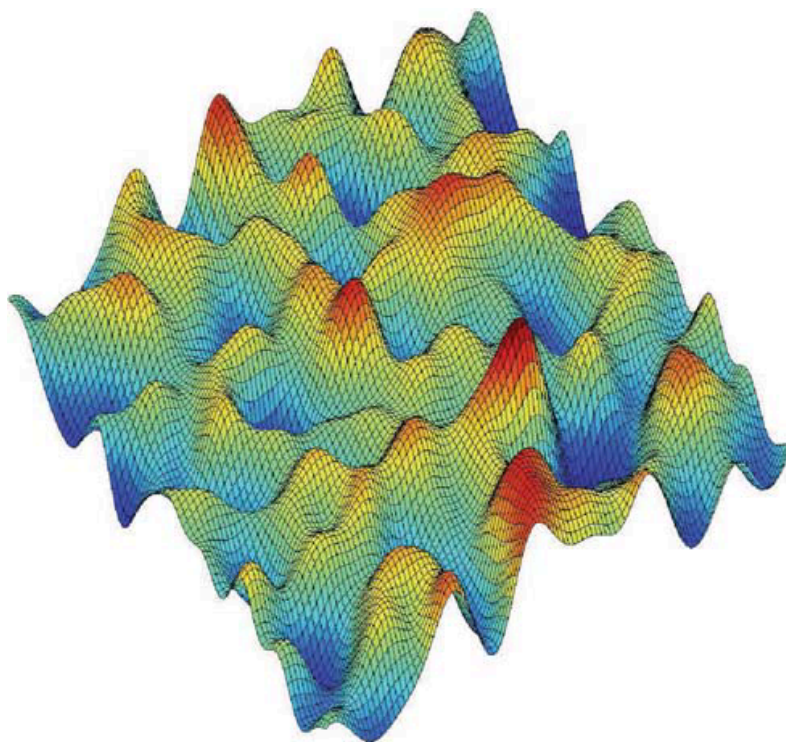
Figure 2.4. Low-dimensional depiction of a complex PES as a landscape with numerous minima, maxima, and saddle points. The vertical elevation is given by the value of the potential energy and the *xy*-plane corresponds to the system's configuration space. At low temperatures, transitions between potential energy minima occur via saddle points that coincide with the mountain passes in this topographic perspective.

A local quadratic approximation to the PES can be constructed using the first and second derivatives of the energy with respect to geometric parameters. The forces on atoms in the system are the negative of the gradient on the PES. Because the forces are zero at energy minima, TSs and higher-order saddle points, these structures are termed stationary points. The matrix of the second derivatives of the energy (Hessian) is known as the force constant matrix. The eigenvectors of the Hessian in Cartesian coordinates correspond to the normal vibrational modes (plus five or six modes for translation and rotation) [90]. For a structure to be characterized as a minimum, the forces (or gradient of PES) must be zero, where all of the eigenvalues of the Hessian must be positive; equivalently, the vibrational frequencies must be real. For a TS, the PES is a maximum in one direction (along the reaction path) and a minimum in all other perpendicular directions. Accordingly, a TS is characterized by a zero gradient of PES with only one negative eigenvalue of a Hessian; correspondingly, a TS has only one imaginary vibrational frequency. For a TS, the vibrational mode with the imaginary frequency is also known as the transition vector.

If the system has temperature T and thermal energy k_BT is relatively small compared to the activation energy barriers that separate neighboring potential energy minima, the system most of the time randomly fluctuates in the deep valleys of the PES. Only rarely will the system fluctuate far enough from one minimum to cross an activation energy barrier and shift to an adjacent minimum.

Because high-energy configurations have small statistical weight, the transition from one minimum to another is most likely to happen if it crosses the activation energy barrier at its lowest point. Wandering along the minimum, the system can cross the barrier at the lowest possible energetic expense. In the presence of thermal noise, the system does not pass precisely through the saddle point or transition state (TS) but will cross the potential energy barrier somewhere very close to it. Both the equilibrium thermodynamics as well as the dynamics of the system can be deduced from knowledge of minima and saddle points and there are exist algorithms for finding these stationary points.

The landscape picture can be extended to systems at non-zero pressure and at higher temperatures, where entropic effects may become important, by introducing the concept of a free energy landscape. This landscape perspective can be therefore applied also to the free energies and such kind of surface depicted in Figure 2.4 as an example of a FES. Minima in the free energy landscape then correspond to stable states in which the system is mainly observed. These stable states are separated by free energy barriers, which are crossed when the system performs a transition from one free energy minimum to another. Thus, the exploration of FES can be very fruitful for the pressure-induced solid-solid phase transitions.

2.3 Transition State Theory

Transition state theory (TST) was developed to describe the transition rate of reactions when already determined relevant bottlenecks that the system passes through during the transition [91–93]. *TST* is the central concept that is a basis for rare event simulation methods and explains the kinetics of rare events. The basic idea of *TST* is to divide the energy landscape between two stable states by the surface.

2.3.1 Reaction rate constant
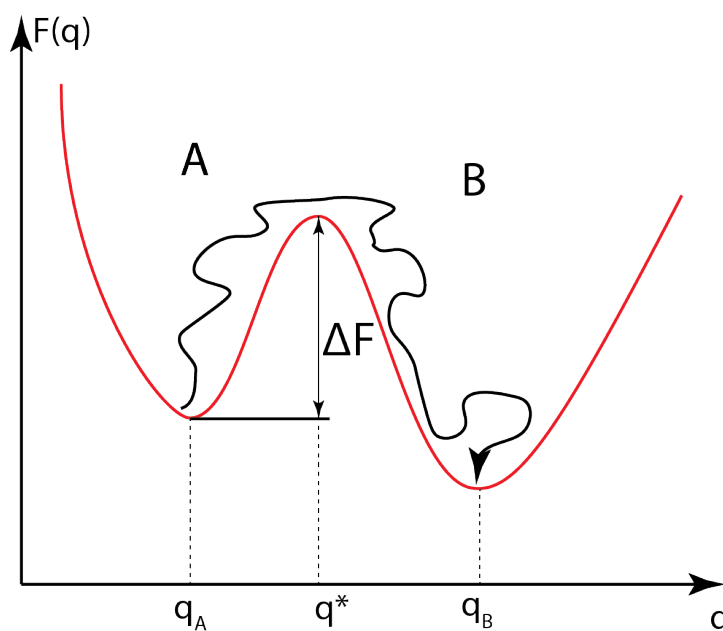
Figure 2.5. Free energy $F(q)$ as a function of the reaction coordinate q. A free energy barrier of height ΔF located at q^* separates the stable states A and B. The *thin wiggly line* represents a trajectory going from A to B.

Consider a system with a bistable free energy $F(q)$, as shown in Figure 2.5. The presented free energy profile is a good illustration of a molecule in solution undergoing isomerizations between two stable conformations. Molecules of type A can be converted into molecules of type B and vice versa. The two neighboring local minima represent these two stable states. Lets introduce the indicator function $h_B[q(t)]$ for state B which shows whether system is right or left of the barrier and can be presented as

$$h_B[q] = \begin{cases} 1 \ if \ q \geq q^* \\ 0 \ if \ q < q^* \end{cases} \tag{2.3}$$

The indicator function $h_A(q)$ for state A is defined analogously. The indicator functions h_A and h_B simply tell us whether the system resides in A or B.

Using these indicator functions we can express the conditional probability to find the system in state B at time t provided it was in A at time 0,

$$C(t) \equiv \frac{\langle h_A[q(0)] \cdot h_B[q(t)] \rangle}{\langle h_A \rangle} \qquad (2.4)$$

where angular brackets $\langle \cdots \rangle$ denote an average over equilibrium initial conditions. The averages $\langle h_A \rangle$ and $\langle h_B \rangle$ are the probability to find the system in state A and B, respectively.

The time correlation function $C(t)$ is a description of the transition statistics in the equilibrium system described in terms of the microscopic degrees of freedom. To make contact with a macroscopic description, appropriate for an experiment, there is considered the time evolution of the concentrations $c_A(t) = \frac{N_A}{V}$ and $c_B(t) = \frac{N_B}{V}$ defined as the number of molecules per volume V.

For the classical problem, where originally all molecules in the system are of type A at $t = 0$, in the approximation of the dilute solution of molecules type A and type B (no interaction between molecules), within the linear approximation to the time correlation function $C(t)$ gives us

$$C(t) \approx k_{AB} \cdot t, \qquad (2.5)$$

where k_{AB} is a reaction rate constant. Equivalently, the time derivative of $C(t)$, is a constant and equal to the reaction rate constant k_{AB} [94],

$$k(t) \equiv \dot{C}(t) \approx k_{AB}. \qquad (2.6)$$

In the equation (2.6), $C(\dot{t})$ is also called the reactive flux. Using this equation, one can estimate the reaction rate constants within *TST*.

As shown in Figure 2.5, the transition from reactants to products, as a rare event, needs sufficient energy to overcome a potential barrier, also known as activation energy. So when investigating the dynamics of the transition with *TST*, the main task is to find the energy barrier for the transition. A good way to tackle this is to describe the free energy of the system as a function of a reaction coordinate, which embraces all information about the transition.

2.3.2 TST Reaction rate constant

The condition $q(r) = q^*$ for collective coordinate $q(r)$ defines transition state (TS) surface that separates states A and B, the so-called dividing surface. Figure 2.6 illustrates a suitable TS surface, where only a small part of the TS surface is shown. Moreover, the validity of any TST-based method fully relies on the TS surface choice.

The goal of *TST* is to define an equilibrium flux through the TS surface and resulting reaction rate. In practice, searching for an analytic expression of a TS surface is usually not possible, so approximations are necessary.

The key role in *TST* plays an assumption that there is no recrossings of the dividing TS surface. In other words, this approximation means that each crossing of dividing surface corresponds to transition to another state and such transition is only allowed once at a time. Herein, if the trajectory

has passed the dividing surface heading into B, the system will relax into B. If the dynamics are reversible, each crossing point on the TS corresponding to a trajectory $A \to B$, should result into a trajectory $B \to A$ on reversing the momenta. Consequently, each point on the *TST* dividing surface has an equal probability of ending in either A or B. Given a TS surface that bounds the initial state, the calculated equilibrium flux through the surface presented as [91–93]

$$k_{TST} = \frac{1}{2} \cdot \langle |\dot{q}| \rangle_{q=q^*} \cdot \frac{exp(-\beta \cdot F(q^*))}{\int_{-\infty}^{q^*} exp(-\beta \cdot F(q)) \cdot dq} \qquad (2.7)$$

where $\langle ... \rangle_{q=q^*}$ means an ensemble average. In the rate of escape from the minimum, we are considering the outgoing flux through the TS surface, thus the factor of 1/2 is present. The next factor is simply the average positive rate of change $\dot{q}$ of the reaction coordinate and the final factor is totally related to the free energy $F(q)$. The obtained equation is also known as the Arrhenius equation and it fully characterizes activated processes. Equation (2.7) is the main result for *TST* and a simple numerical procedure can be devised from it: first, calculate the free energy $F(q)$ as a function of the reaction coordinate $q(r)$. All the dynamical information needed to describe the transition process can be obtained from the free energy F as a function of a reaction coordinate to determine q^* of the dividing surface. Then, calculate the average positive flux $\langle |\dot{q}| \rangle_{q=q^*}$, which can be either calculated analytically or determined by the simulation. And finally, combine them together. *TST* does not require the dynamical trajectories calculation, thus the reaction rate constant evaluation is computationally efficient.
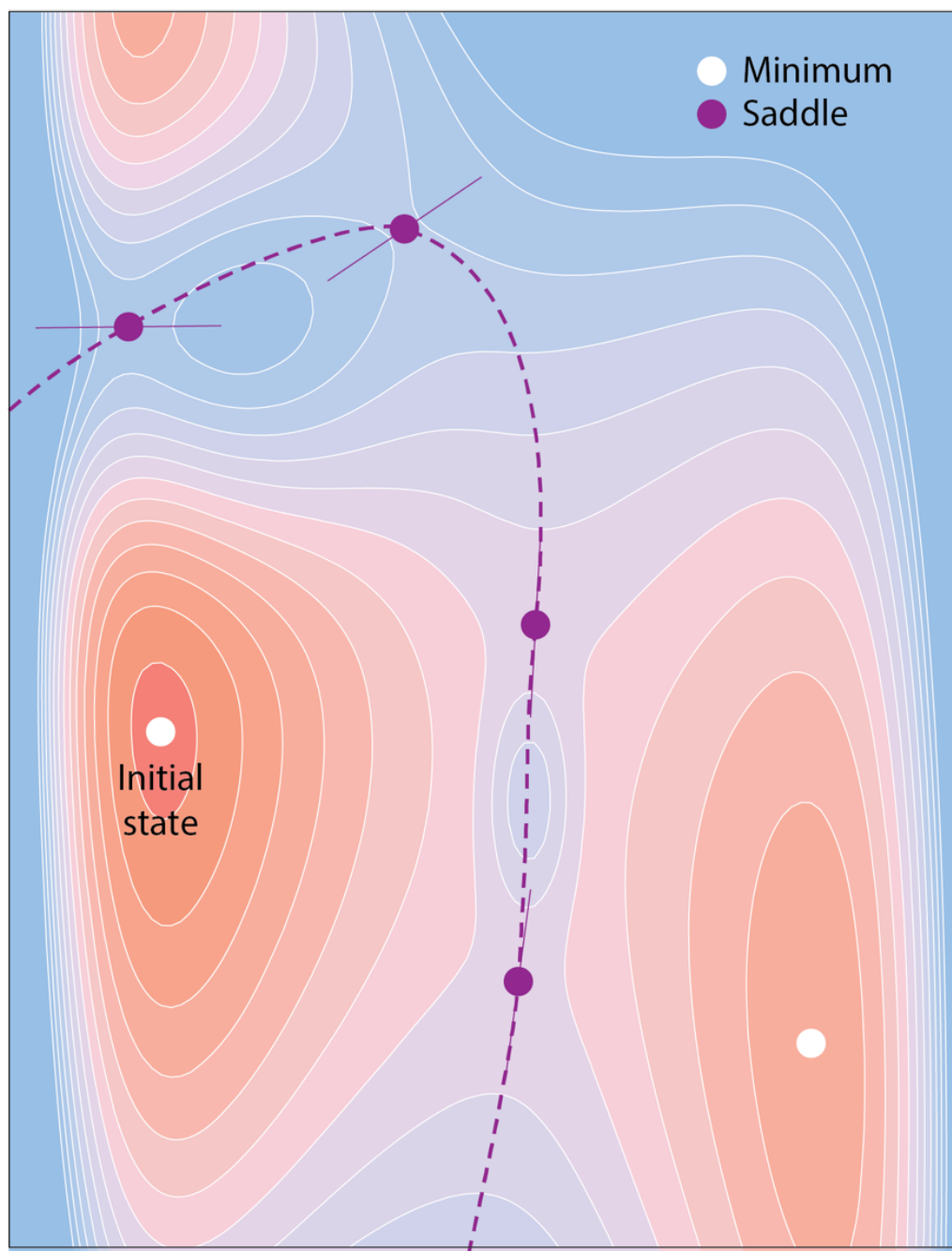
Figure 2.6. 2D model of potential energy surface, where transition state is drawn as a dashed line. There is a set of saddle points on the boundary of the initial state, which can be used to estimate escape rates within transition state theory (reprinted from Ref [95]).

In practice, the construction of proper TS surfaces is not an easy task, so that trajectories will recross the TS surface and either fail to be reactive or recross before a reaction occurs. The k_{TST} value is an upper bound on the real transition rate because *TST* counts each crossing as reactive and each reactive trajectory must have at least once crossing the TS surface. This is a powerful principle because it means that the TS surface can be variationally optimized to lower the *TST* rate to approach the real transition rate [96]. Additionally, one can compute a transmission coefficient κ by using short

trajectories from the TS and counting the ratio of crossing points to reactive trajectories. The true escape rate is then $k = \boldsymbol{\kappa} \cdot k_{TST}$ [94,97].

The pioneers of the TST approach were Chandler [94], Anderson [98] and Bennett [99]. Since then, TST was employed and systematically improved in order to get the best approximation for dynamical process statistics.

2.3.3 Harmonic approximation

The vast majority of calculations in materials science and fields of computational surface chemistry cannot provide a reaction rates evaluation according to the equation (2.7). It is because sampling is resource consuming and because good TS surface determination is a challenging task, especially by using electronic structure methods. The harmonic approximation to *TST* is most commonly used and transforms the kinetics estimation problem into another one. Here, the problem of reaction rate constants calculation in *TST* can be further simplified – on the TS surface, there are bottleneck regions that dominate the rate and these bottlenecks, also called "reaction channels", are characterized by saddle points on the FES like it is shown on Figure 2.6. These saddle points are the lowest-energy points on the FES that need to be crossed (locally) to escape the minimum. The single unstable vibrational mode at each saddle point defines the local normal to the TS surface, and the TS surface is approximated as a hyperplane with a harmonic potential given by the *N−1* remaining stable modes (in Figure 2.6, it is indicated by a purple line at each saddle). As shown in Figure 2.7, the free energy barrier is crossed near a point r_{TS}, which is a saddle point in the FES. The stable states of the system correspond to potential energy minima at r_A and r_B.
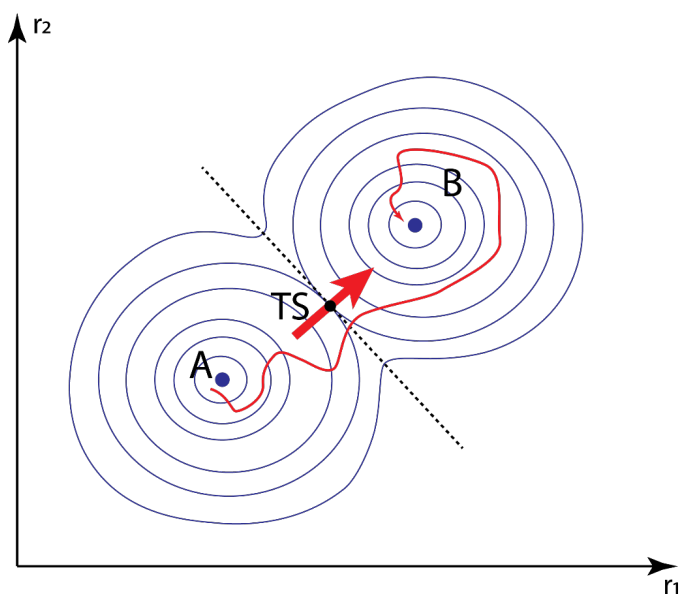
Figure 2.7. 2D model of FES. Here, *A* and *B* are stable states, which correspond to minima on the FES. The transition state TS that needs to be crossed during a transition between the stable states is a saddle point on the FES. The thick red arrow indicates the direction of the unstable mode and the dashed line is the plane dividing surface orthogonally to this direction.

This version of *TST* requires the precise location of the stationary points. At low temperatures, one can approximate the FES near the stable states and the saddle points with a Taylor expansion truncated after the quadratic term. First, it needs to carry out a normal mode analysis in the potential energy minimum A as well as in the TS by diagonalizing the mass weighted Hessian

$$H_{ij} = \frac{1}{\sqrt{m_i m_j}} \cdot \frac{\partial^2 V(r)}{\partial r_i \partial r_j} \tag{2.8}$$

where m_i is the mass associated with the degree of freedom r_i. In the potential energy minimum A, this normal mode analysis yields eigenvalues λ_i^A which are all positive and the eigenfrequencies $\omega_i^A = \sqrt{\lambda_i^A}$. In contrast, at the saddle point exactly one of the eigenvalues λ_i^{TS} is negative while all others are positive. The normal mode corresponding to the negative eigenvalue is the so-called unstable mode and it is in this direction that the system is assumed to cross the transition state in the harmonic approximation. The direction of the unstable mode is denoted by a red arrow in Figure 2.7. Accordingly, the dividing surface is the plane normal to the direction of the unstable mode. The frequencies at the transition state in directions orthogonal to that of the unstable mode are given by $\omega_i^{TS} = \sqrt{\lambda_i^{TS}}$.

It is essential to understand that the *HTST* is used to calculate the escape rate via each transition channel characterized by a saddle point. The resulting escape rate from the minimum is approximated by summing over all transition channels. In this way, *HTST* can be viewed as approximating TS surface by a set of hyperplanes passing through each saddle on the boundary of the initial state. Although it is common to hear the terms saddle point and transition state used interchangeably, this association is appropriate only in one dimension. In high-dimensional systems, the harmonic TS is the hyperplane that passes through the saddle with a normal along the unstable mode, and more generally in TST, the TS surface is an $(N - 1)$–dimensional surface that divides the initial state and product states.

The *HTST* approximation allows the analytic evaluation of equation (2.7):

$$k_{TST}^{ha} = \frac{1}{2\pi} \cdot \frac{\prod_{i=1}^{n} \omega_i^A}{\prod_{i=1}^{n-1} \omega_i^{TS}} \cdot exp(-\beta \cdot \Delta F) \tag{2.9}$$

where n is a number of non-vanishing eigenvalues in the minimum, $\Delta F = F(r_{TS}) - F(r_A)$ is the difference between the potential energy of saddle point and potential energy of minimum [100]. Similar to the Arrhenius formulation, according to the harmonic approximation, the reaction rate constant can be represented as the product of two factors:

$$k_{TST}^{ha} = v \cdot exp(-\beta \cdot \Delta F) \tag{2.10}$$

where the temperature T has been included as an argument of k_{TST}. This equation emphasizes the dependence of the reaction rate constant on the temperature. The vibrational prefactor ν is related to the width of the potential energy well at the minimum and the energy valley at the saddle point and is a characteristic atomic vibrational frequency. It can be calculated explicitly to capture entropic contributions to the transition rate. The prefactor ν is small if the passageway at the saddle point is narrow and large if it is wide. While this prefactor can play a role in some cases, it is usually the exponential dependence of ΔF which is the dominating factor.

An assumption that *HTST* is a zero-temperature approximation, is a widespread misconception for this theory. It is because for equation (2.10), there is no need for finite-temperature MD. Clearly, *HTST* will be precise and accurate for reactions that follow an Arrhenius rate dependence, i.e. reactions where the entropic contributions to the rate are temperature independent.

Equation (2.10) is the final result of the *HTST* and according to this equation, only local properties of minima and saddle points characterize the transition. That is why *HTST* is particularly attractive for the simulation. This means, there is no need for the additional sampling of the FES. Within the *HTST* approximation, during the calculation of reaction, the most challenging task is not the equation (2.10) evaluating but locating the saddle points that characterize reaction pathways. It especially becomes much harder in high-dimensional systems.

2.3.4 Application of HTST to rare events simulation

Although the *HTST* and its harmonic approximation have been widely applied for studying phase transitions and chemical reactions [101,102], there are still some theoretical limitations. First, *TST* is incomplete to describe some reactions at high temperatures. Thus, HTST always well describes reactions occurring at low temperatures and some other cases, where entropic contributions to the rate are temperature independent. Otherwise, the complex motion of atoms and collisions between them may lead to transition states far away from the lowest energy saddle point.

Second, we assume that the atomic nuclei behave according to basic mechanisms in TST [91]. With this assumption, atoms or molecules are required to overcome enough transition energy to form the transition structure. In quantum mechanics, there is a non-zero probability that particles tunnel across any finite barrier. For molecular reaction, there is a chance that molecules will react even in a case when they do not collide with enough energy to overcome the energy barrier [103]. The tunneling effect can be neglected for the transition with high activation energy, instead, it is essential in the low-activation-energy transitions since the probability of tunneling effect increases with decreasing barrier height.

Considering the previously mentioned limitation, here is a scheme for the reaction rate evaluations for the system, where energetic effects dominate (as opposed to entropic effects). First,

using algorithms that consider gradients of the FES, the TS surface can be constructed. All found saddle points are then systematically determined by the enumeration of stationary points on the FES. Local minima exemplify attraction basins, while saddle points indicate transition states. Other minima can be retrieved by the small fluctuations from saddle points [104,105].

If the transition surface location is known, one may construct a scheme where the system first moves reversibly to the transition state surface. Many fleeting trajectories are then initiated. The first step consists of determining the reversible work, thus the probability of reaching the transition state surface. Second step consists of the determination of the probability of successful crossing the threshold using the set of obtained trajectories. Combination of these steps provides the rare event rate constant [106] that can be directly compared to experimental observables.

"Solid-solid transitions have been important in technology for thousands of years and are also important in geological processes. Moreover, the pattern of symmetry breaking that exists in solids means that these transitions are not only technologically important, but that there are a lot of them (symmetry breaking patterns). The problem in understanding the transitions is that they typically happen under extreme conditions (high temperature or pressure), which makes them hard to study."[ii]

3 SIMULATING PHASE TRANSITIONS

The last several decades have proven that molecular simulation is a powerful tool for studying the activated processes kinetics. It supplies detailed atomistic information that is hard to access from experimental studies.

The direct exploration of the free energy surface (FES) is the main strategy for the mechanisms of activated processes understanding and, in particular, phase transitions in solids. There are many computational methods for this because there are different classes of energy landscapes and various questions that can be asked about kinetic properties. Most of these techniques, such as molecular dynamics (MD) [107,108], are based on employing either classical or ab initio-based atomistic force fields [107,109] and can generate dynamic trajectories by integrating the equations of motion for all atoms in the system. It provides a reasonable realistic model of the process of interest [94]. Unfortunately, the straightforward application of MD is impractical to the study of rare events such as solid-solid phase transitions because of the small system sizes and time scales. Many phenomena that we care about occur on the human timescale of seconds or longer. When interatomic interactions must be accurately described (electronic structure methods are needed), simulating even nanoseconds of dynamics is a huge effort. For example, crystal nucleation simulation can take seconds and even with billions of steps, MD simulation cannot overcome the microseconds limit. Moreover, even many billions of simulation steps are not guaranteed to yield even a single event occurrence.

As mentioned above, the picture of rare transitions between two stable states can be described in the language of statistical mechanics as two free energy minima separated by a high activation barrier [94] and the probability of observing a transition decreases exponentially with the barrier height. A good illustration of such kind of transition is shown in Figure 3.1. This figure illustrates the energy profile at room temperature with two minima and the energy barrier of 0.5 eV and with a typical pre-exponential factor such that crossing events happen 1000 times per second, which is very slow on the

---

[ii] The quotations are taken from an article of G. van Anders et al. in the Proceedings of the National Academy of Sciences, 2017.

timescale of atomic vibrations. For the direct MD simulation, where each vibration spans a second, getting such reactive event as one transition to another well will take more than 100 years, which is incredibly slow on the atomic scale. Clearly, this approach is very far beyond what is possible for current methods and unlikely will be able to simulate such events in the near future.
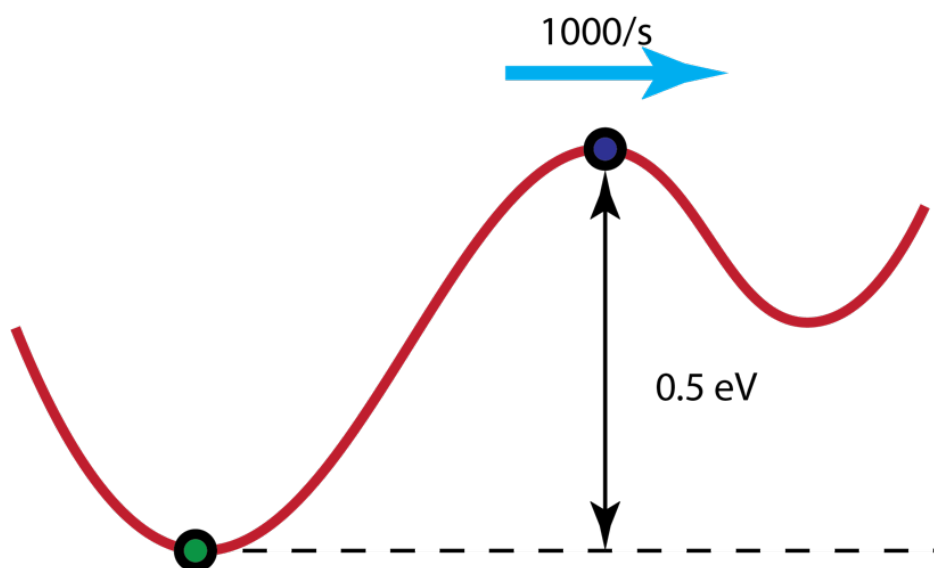
Figure 3.1. An example of a system at room temperature with two energy wells. The transition occurs when the activation barrier of 0.5 eV is overcome.

Generally, computer simulation techniques that integrate the equation of motion of the underlying dynamics [107,108], whether it is deterministic (Hamiltonian), stochastic (Langevin), or even Monte Carlo (MC) dynamics, could provide insight into the reaction coordinate describing the progress of the rare transition. Since the times separating successive transitions are very long, the straightforward application of conventional simulations makes them impractical. Thus, such simulations will likely fail to exhibit the essential dynamics of interest and are far beyond the capabilities of modern high-performance computers. Obviously, more advanced (than canonical MD or Monte Carlo) techniques that help to overcome the rare event problem must be used. Therein, the focus shifted to the rare event simulation while skipping the tedious long waiting times.

For a condensed material rare events simulation, such as phase transitions in solids, the bottlenecks are associated with the nucleation of a new phase. The nature of the bottleneck in the case of solid-solid phase transition depends upon the energy required to distort the local structure with further opening of the possible pathways for the transition of an atom from one interstitial site to another.

Herein, solid-solid phase transitions investigations consist in understanding the transition details by identifying:

- **Transition mechanism**.

  It can be determined from the reorganization of the atomic structure associated with nucleation and growth of a new phase.

- **Transition states**.

  The consequence of local deformations or the formation of low dimensional structures interfacing the coexistence of different phases.

- **Kinetics of the transition**

  In other words, it is the calculation of the rate constants. Here, the relevant degrees of freedom, or reaction coordinates, must be identified.

Below, I will describe several techniques to explore (free) energy landscapes, which relate to the first two steps of the presented scheme.

3.1 Exploring energy landscapes

All existing theoretical methods for the PES exploration of solids can be generally divided into two groups. The first group is represented by methods that are aiming the structure search, while the other group of methods are targeting the kinetic information on the phase transition pathway in solids. The efficiency and accuracy of the algorithms for the structure search can be assessed by their ability to find the most important minima on PES, e.g. global minima (GM) [105,110–119]. The results can be utilized for the thermodynamic properties of materials understanding. For the transition kinetics study, the focus is much less on theoretical modelling because many different pathways exist between the minima. Pathway sampling is theoretically much more challenging than minima sampling [85,120]. Identifying the correct reaction coordinate [121] among many degrees of freedom is the main problem in pathway sampling but usually irrelevant in structure search.

At this moment, structure search theoretical methods are involving structure change in an aggressive way. It can be changes of either atomic or lattice degrees of freedom or both simultaneously. Such aggressive change of structure parameters helps to pass the transition region of PES without trapping in local minima. For example, some GM searching methods, like minima hopping [115,116], simulated annealing [122–125], basin hopping [114,126], start from the one predefined structure on PES. Originally, these methods were developed for non-periodic systems (e.g. molecules or clusters) and then they have been extended to periodic systems, i.e. crystals, although their applications are still limited.

Another group of methods starts from multiple entries (different initial structures on PES), such as evolutionary algorithm (EA) as represented by USPEX [117,121] and the algorithms based on particle-swarm-optimization (PSO) algorithm [111,127]. They have shown big success in predicting previously

unknown structures. However, a trajectory during PES searching cannot be obtained as a result of the simulation. Thus, the pathway information is out of the scope of these methods and cannot give any information on how the phases of interest are connected.

Finding a minimum on PES is comparatively easy because the negative of the gradient always points downhill. By contrast, to be able to obtain the kinetics, the information about the transition state region (e.g. saddle point on PES) must be taken into account. Thus, a transition structure optimization must step uphill in one direction and downhill in all other orthogonal directions. Furthermore, the uphill direction is often not known in advance and must be determined during the optimization. As a result, numerous methods have been developed for transition structure searching and many of them are closely related. Generally, they can be classified as single-ended and double-ended methods [128].

3.1.1 One-ended Methods

This category of methods is focused on the escaping from the initial state *A* without any prior knowledge of the final state. The most common approach to do that is the energy pumping of the system by pushing it from the energy basin to the nearest pass to the new minimum. The realization of this concept lay in the basis of the Laio-Parrinello method [79,129], the enhanced sampling of a given reaction coordinate [130] and conformational flooding [131].

The tools for sampling the PES of crystals, such as metadynamics, involving the constraints (bias potential) [79,112,132]. Metadynamics [70] is the most popular method, which pioneered and inspired many other methods. Related to the crystal structures, metadynamics has been used in many applications presented in Ref [133–138] and more recent review extend the list of applications [139]. Metadynamics and other enhanced sampling methods based on MD techniques [140–142] have shown their high efficiency. These methods have a continuous trajectory as required in MD and scarce structural perturbation, which can be utilized for the low energy pathways identification. Moreover, if the simulation is long enough, it is possible to capture the transition event. A good example is the simulation of the phase transition process between graphite and diamond made by the metadynamics method that imposes collective variable the lattice degrees of freedom [132]. However, metadynamics-based approaches helped to investigate many other phase transitions in solids such as transitions in SiO_2 [112], CdSe [143], NaCl [137], other transitions in carbon [144], solid nitrogen [145], and many more. In case when the minima on PES are known, the barrier height of phase transition and the local density of states can also be estimated by random walk using, for example, the threshold method [146]. Overall, the general concern regarding all these methods is their low efficiency in overcoming the high barrier and simulating phase transition.

Another group of single-ended methods start with an initial structure and displace it toward the transition structure. This group of methods is presented by the mode-following methods, such as the

dimer method [147] with its extension to the solid-state usage [148], growing string method [149] or the crystal stochastic surface walking method [75]. Also, they establish paths from minima to transition state (saddle point on the PES) by following some chosen direction and usually, this direction is the vector aligned with the Hessian eigenvector with the lowest eigenvalues or a combination of such vectors. The mode-following methods evolve configurations between saddle points and adjacent minima. Additionally, this group of methods deals with an extensive exploration of the PES, which requires significant computational resources. Another strategy is based on the exploration of the PES by locating as many minima and saddle points. This approach lay on the basis of the Kinetic Monte Carlo (KMC) technique [150–152] and the discrete path sampling of Wales [113].

Finally, a totally different approach consists of procedures that use artificially controlled enhancements of rare event probability. The most common is the hyperdynamics method developed by Voter et al. [142,153]. Conceptually, it is very similar to metadynamics because both methods rely on adding a bias potential to the global potential energy surface of the system. In metadynamics, the bias potential is used to fill energy minima and, hence, shorten the waiting time between minima-to-minima transitions. In hyperdynamics, it is ensured that bias potential becomes zero in the transition-state region, in which case correct relative dynamics is preserved. This approach is based on reducing the transition barrier using bias potential that fills the energy landscape in regions other than the transition states. Another approach that increases the probability of the rare event on raising the temperature is called temperature accelerated dynamics [154]. Molecular simulation timescale scope can also be extended using parallel processing in parallel replica dynamics [155], where several simulations are parallelly performed in different thermodynamic states. While systems with a sufficiently high temperature pass over the potential bottlenecks, those at low temperatures mainly probe the local free energy minima. A stepwise system swap is used to reproduce the transition event.

3.1.2 Two-ended methods

Alternatively to optimizing a single point on the PES toward the transition structure for a reaction, there are a set of methods that aims to locate TS connecting two known phases directly. As has been mentioned, TS is represented by the first-order saddle point. These kinds of methods optimize the entire transition path from reactants to products. Paths created by one of the one-ended methods can be used. Typically these methods are based on the representation of the transition path by a set of points, that is, a chain-of-states. Different methods of this type differ by what function of the points is minimized, how the chain is generated, and what constraints are imposed to control the optimization.

Many pathway optimization methods are based on minimizing the integral of the energy along the path, normalized by the path length. A simple linear interpolation scheme is helpful to devise the initial pathway by creating a chain of configurations connecting *A* and *B*. Although this approach

does not produce a steepest descent path [156], it provides only a good approximation to it. Sometimes it is essential to use additional potentials to prevent the pathway from kinking or coiling up in minima [157]. The number of intermediate points needed to describe transition pathways usually depends on the nature of the path (e.g., number of intermediates and transition states, the curvature of the path, etc.) and can be in a range from less than 10 to more than 50. Then, several hundreds or thousands of optimization steps are required to converge the simulation, primarily because of the strong coupling of adjacent points motions.

The most common chain-of-state methods are the Nudged Elastic Band (NEB) [158,159] method and the string method [160]. At the same time, chain-of-states methods have several different extensions to simulate phase transitions in solids [161–163], which helped to simulate phase transitions in CdSe [162,163], diamond-lonsdaleite, ice and silica systems [164] and many more. The methods inheriting NEB basis are the most common and popular techniques for transition path calculation as they perform with a good combination of efficiency and simplicity. In the NEB method [158,159], the points are kept equally spaced by adding a spring potential between them. Here, the gradient for a point has contributions from the potential energy surface and from the spring potential, which can be projected into components parallel and perpendicular to the path. The algorithm uses the gradient of the spring potential to displace (nudge) the points along the reaction pathway and uses the gradient of the PES for directions perpendicular to the path. The spring potential is used to couple points on the pathway and maintain uniform spacing between these points in the chain.
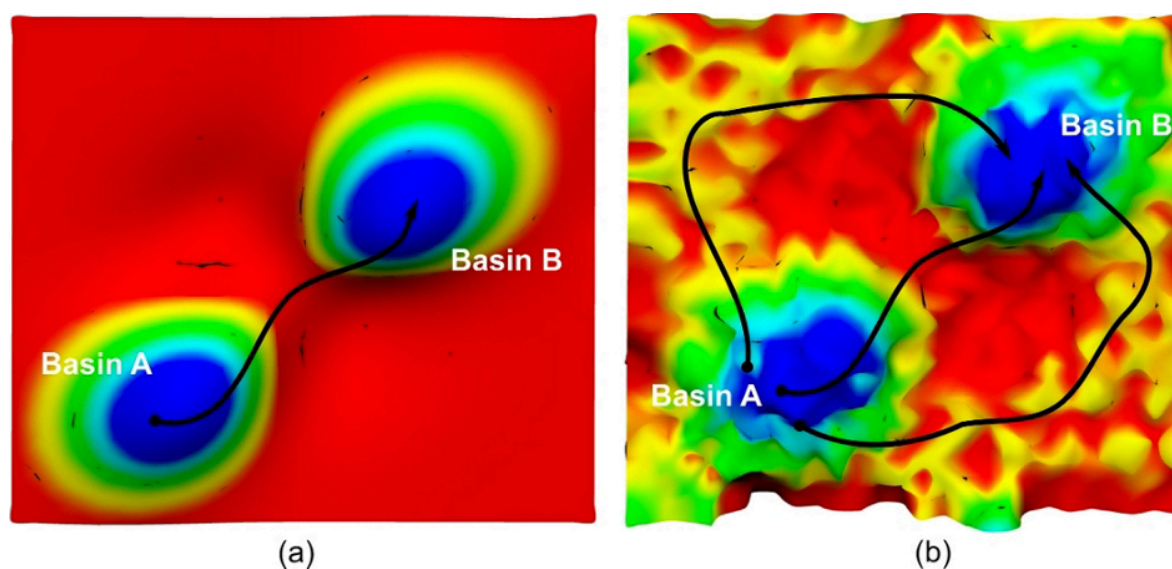
Figure 3.2. Schematic illustration of two types of PES topologies as controlled by (a) energetic effects and (b) entropic effects. Color scale distinguishes between low energy (blue) and high energy (red) regions. On the right, a more complex representation of PES and the variety of pathways are presented (Reprinted from Ref [65]).

Chain-of-state methods presented above are still more costly than one-ended methods for transition structures, and there is spacious room for the improvement of these methods. However,

they do map out the entire transition path. It can be beneficial if the pathway contains several transition states and intermediate minima. Furthermore, chain-of-states methods are more readily parallelized than other single-ended methods. Along with that, one major drawback of chain-of-states methods is the high dependence of the result on the accuracy of the initial guess of the pathway. If the manually generated initial path is not close enough to the real MEP, the algorithm will converge to MEP very slowly or, in the worst case, even will provide an unphysical result.

For the transition pathways in solids, these methods do not include the sampling of transition pathways and can miss the lowest energy pathway. For example, the more realistic scheme of PES is presented in Figure 3.2, where it is shown how many different pathways can exist and how hard the MEP is to find. Also, it is particularly challenging to guess the TS or final state (with the knowledge of the initial state) due to the existence of many equivalent choices of the cell in periodic structures ("modular invariance").

Finally, there are other ways to study the rare event problem that are based on the minimization of a suitably defined discretized action [165], or to use modified stochastic equations of motion to drive the system from A to B [166,167]. However, all these methods work pretty successfully for small systems with smooth topography of energy landscape, where the choice of reaction coordinates is not a problem. For larger systems, reaction coordinates are not known and are difficult to anticipate. Since the energy landscape becomes rougher with the number of atoms (as shown in Figure 3.2b), the TS definition is not enough – there are many of them and their enumeration is a colossal task. However, one can distinguish those dynamically relevant for the transition process – using an ensemble of transition states sampling, which can be done by transitions path sampling (TPS) [106,168,169].

3.1.3 Limitations

As has been mentioned before, the study of transitions aims to obtain the transition mechanism and precisely locate relevant transition states. The choice of a reaction coordinate plays a key role in this problem. If the reaction coordinate is wrongly chosen, then TST and the mentioned methods may show unreliable results. Sometimes, the chemical or physical intuition guides the choice of which degrees of freedom are relevant and which are not. However, it is not a trivial choice, especially for large systems. Moreover, even if the reaction coordinate looks good, some essential phenomena still out of the scope of the transition. So, the kinetic information may be obtained using one of the methods listed above.

Unfortunately, the phase transition simulation methodology performs simulations, where all unit cells of the constructed lattice evaluate equally and simultaneously. However, phase transitions proceed via nucleation and growth, as mentioned before, and the methods mentioned above are a rough but crystallographically and intuitively clear model. The complex study of nucleation and growth phenomena requires much larger systems (including hundreds and thousands of atoms) and

advanced sampling methods such as transition path sampling (TPS) [168]. However, this method requires a very accurate force field and the simulation takes a very long time.

4 METHODOLOGY

A particularly complicated problem of finding MEP between two structures by any chain-of-states algorithm is the challenge of generating a good initial pathway that will be refined to the nearest MEP. For any kind of aperiodic systems such as molecules or clusters, this task is much easier that for periodic [iii]. For crystals, this problem becomes a big challenge due to the periodicity of the structure since the number of possible variants of lattice parameters choice is infinite. Moreover, efforts in developing approaches to predict the real MEP and transition states have also been (and still are) under development.

The general workflow of finding phase transition mechanism consists of three steps:

- **Mapping building**
  The goal is to identify pairs of corresponding atoms between the initial and final geometrical configurations with an equal number of atoms in both.

- **Initial pathway(s) generation**
  Based on the previously devised mapping(s) between two structures, we generate a suitable interpolation(s) between the initial and final states and consider them as the initial pathway(s).

- **Pathway optimization**
  Previously generated initial pathway(s) must be refined by one of the chain-of-states methods.

The results of the previous step become an input for the next one. And the final result is the set of pathways, among which the one with the lowest energy barrier will be chosen.

Each of these steps has a number of difficulties for solid-solid transformations, which are not faced for aperiodic systems. In particular, lattice parameters representing translational symmetry are usually adopted to efficiently describe bulk, which works perfectly for equilibrium property calculations. During phase transitions, both lattice parameters and atomic coordinates change. These two types of variables need to be treated in an unbiased way to correctly represent the reaction coordinates of the transitions. Therefore, a generalized configuration space spanned by both cell and atomic degrees of freedom is introduced, along with a metric for proper distance measurements.

4.1 Crystal structures mapping algorithms

Here are presented several algorithms that search for the most compatible representations of pair of crystal structures and provide the structural correspondence to represent a diffusionless transformation [iv]. The main challenge for such algorithms is finding a proper mapping of atoms considering periodic boundary conditions. The first part is devoted to the purely geometrical iterative

---

[iii] It depends on the size of the molecule/cluster. The complexity of the problem of proper mapping choice has an exponential dependence on the number of atoms.

[iv] Diffusionless transformation do not require long-range diffusion during the phase change; only small atomic movements over usually less than the interatomic distances are needed.

algorithms. The second part is devoted to describing a new topological view of mapping structures onto each other.

4.1.1 Geometrical mapping algorithm

First, it must be noted that "geometric methods" mean that these methods deal only with cell parameters and atomic positions and try to map these parameters onto each other without taking energetics into account. The complexity of such methods grows exponentially with the number of atoms. Thus, it is highly ineffective for systems with a large number of atoms in the unit cell. The mapping algorithm made by Stevanovic and co-workers [170,171] will be described below. This algorithm is one that has been used in this Thesis. The goal of this algorithm is to find such mapping that represents diffusionless transformation.

The algorithm is based on the criteria of minimizing the Euclidean distance between corresponding atoms in initial and final structures and minimizing the change in the coordination of atoms along the transition path. The algorithm consists of two steps. At the first stage, the algorithm seeks the most convenient representations of the initial and final structures. It defines the least common multiple for the number of atoms N in both cells and then expands two unit cells to the previously obtained number of atoms N by constructing all possible symmetrically inequivalent supercells. According to the Hart–Forcade theory [172], the symmetry inequivalent supercells can be determined and enumerated. Next, the algorithm omits atomic positions and seeks the most compatible representations of supercells or, in other words, such pair of supercells that minimizes the strain between them. This statement can be interpreted as maximization of spatial (volumetric) overlap between generated cells. The algorithm searches for such combination of two unit cells, where the weighted sum of the absolute differences in unit cell parameters (lattice vectors a, b, c and lattice angles α, β, γ) and the total surface areas (S) of the two cells is minimal. It can be formulated as follows:

$$d(cell_1, cell_2) = \sum_{\substack{q=a,b,c, \\ \alpha,\beta,\gamma,S}} C_q \cdot |q_1 - q_2| \tag{4.1}$$

where C_q are some positive weights of quantities q. They are necessary to make the numerical values the same order of magnitude. The search for maximum overlap in the generated cell is accomplished by transforming the cells to the corresponding (unique) reduced cell according to the formulation of Niggli-Santora- Gruber [173,174]. This allows one to implicitly explore all isometric transformations of the two cells (rigid rotations and reflections) and all permutations of the unit cell vectors.

At the second stage, atoms of each structure are placed back into two generated supercells. The search for the optimal atom-to-atom mapping is performed with special operations on two sets of atomic positions [170,175]. These operations should satisfy the following conditions: (1) all symmetry

operations of parent Bravais lattices should be conserved, (2) the origin of the coordinate system should be at an atomic position, and (3) the permutations of indices of chemically identical atoms should be independent. Each chosen symmetry operation, the position of atoms, or permutation of indices of atoms is considered as a unified mapping between the structures and a pathway in the configuration space [170,175]. This two-step algorithm is illustrated in Figure 4.1.
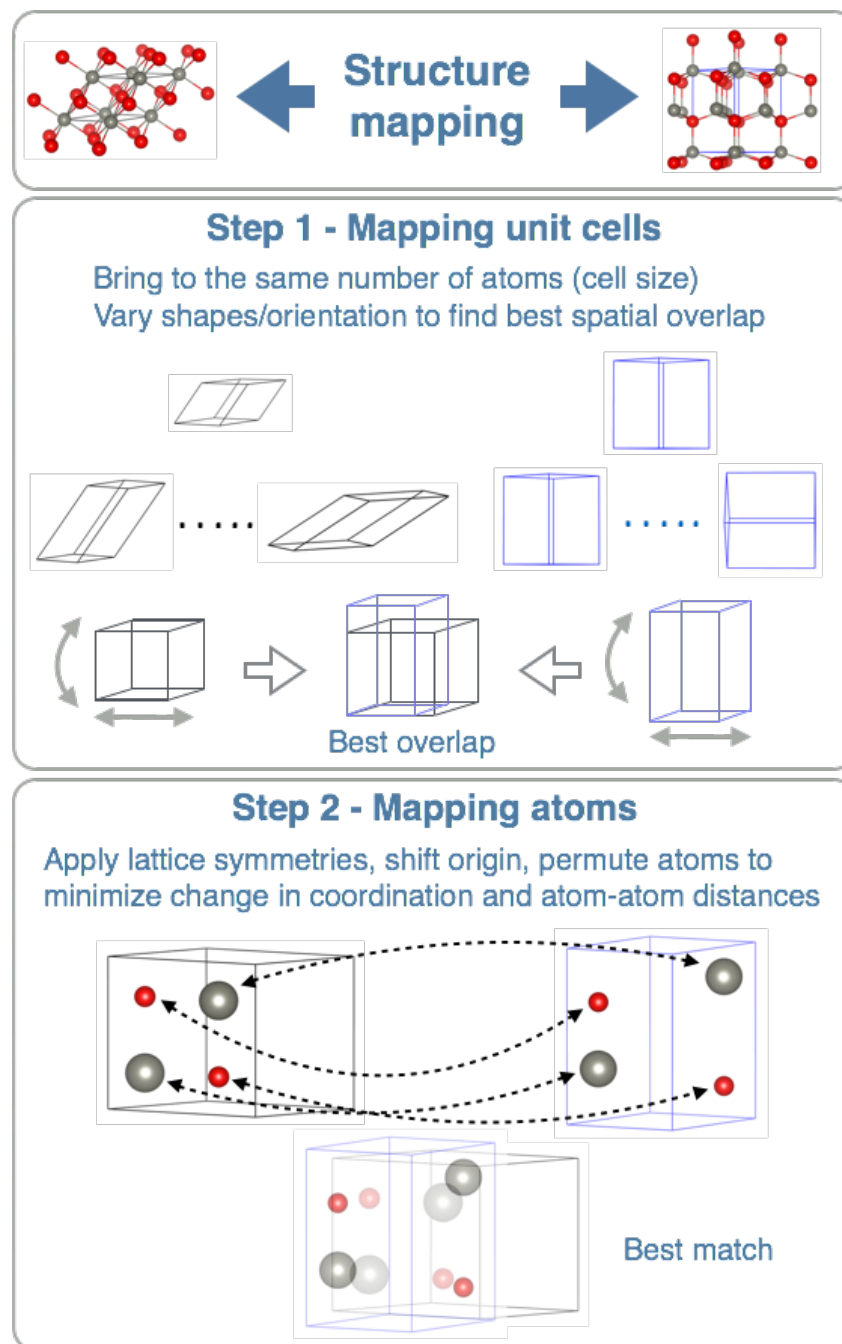
Figure 4.1. Schematics of the two-step geometrical structure mapping algorithm (Reprinted from Ref [170]).

Out of many possible atom-to-atom mappings, this algorithm selects the optimal mapping solution that yields a minimum of the sum of Euclidian distances between the corresponding atoms in the structures. In case when more than one solution is found, then the sum of distances between

the atoms is used to making comparisons for ranking them in ascending order and narrow down the choice. The described operations are performed using Hart-Forcade theory [172]. This theory allows one to enumerate the symmetry inequivalent atom sites. The Munkres algorithm [176] is used to find the optimal atomic permutation indices. Among the set of possible atom-to-atom mapping, taken only those where the trajectory mileage of atoms during the transition from the initial structure to the final structures is as less as possible [170,175]. Finally, it generates several variants of possible pathways and returns them as an output.

This approach is not unique and there is a similar approach developed previously by Goedecker and Sadeghi [177]. It measures configuration space distances between aperiodic systems, and as a result, gives the mapping between structures. Also, a search algorithm for the identification of identical (duplicate) periodic structures that helps to map the unit cells that was developed by Lonie and Zurek [178]. Another class of newly developed approaches is based on the descriptor-, feature-based fingerprinting for the similarity of different periodic structures quantifying. These methods compare a selected set of features (not atom-by-atom) and good examples of such works are made by Yang et al. [179] and by Zhu et al. [180]. In addition, several methods are based on the symmetry distortion approach for cell parameters matching made by Munro et al. [181] and by Hatch [57]. However, atomic mapping is still based on the search for optimal transition trajectory lengths. In the algorithm made by Stevanovic et al. [170,171], the unit cells mapping algorithm can be viewed as a more generalized of the ideas proposed by Lonie and Zurek [178] to the case where the goal is to discover the optimal alignment of two input structures and where these structures are presumed to be different. Concerning the atom-to-atom mapping, this was made by the extension of the algorithm of Goedecker and Sadeghi [177] to periodic systems.

4.1.2 Topological mapping algorithm

Instead of considering the crystal structures as a set of atoms inside the cell, it can be represented as a periodic graph. Initially, this idea was proposed by Wells in 1954 [182] and is now the most common approach for describing crystal structure topology. Here, the atoms and/or atomic groups in the crystal structure are represented as nodes and interatomic contacts or links between atomic groups are represented as edges. Considering the periodicity of crystals, we get an infinite periodic graph, which is called a net. In some cases, the net connectivity of crystal structure cannot be precisely determined on the level of human expertise and it can be done only using specific algorithms to generate the net [183]. Sometimes, several different topologies correspond to the same structure [184] and, conversely, different crystal structures may have the same net connectivity (same topology).
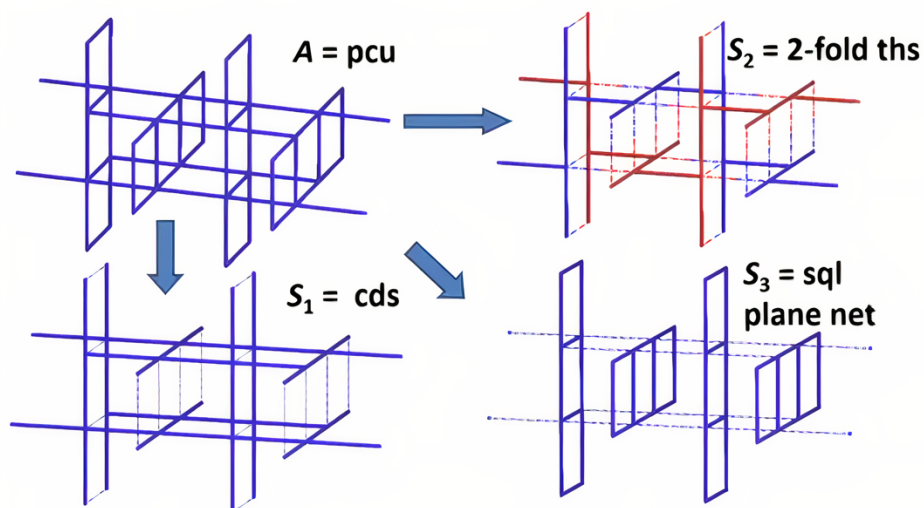
Figure 4.2. Different ways of subnet generation. The net *A* is starting topology and *S1*, *S2*, *S3* are subnets of *A*. (reprinted from Ref [164])

However, the supernet-subnet concept must be introduced for the whole picture scope. The subnet of some specific net is generated by the cutting edges and, vice versa, the supernet is generated by creating new edges. As shown in Figure 4.2, topology *A* has **pcu** (primitive cubic) topological type and, by cutting some edges, it can be transformed into different subnets. The subnet *S1* shown in Figure 4.2 is the 1-fold subnet of **pcu** and has **cds** (cadmium sulfide) topological type. The subnet *S2* shown in Figure 4.2 is the 2-fold subnet of **pcu** and has **ths** topological type. The *S2* subnet has 2 topologically equivalent networks that are interpenetrated into each other (colored by blue and red) and these networks do not connected to each other. The subnet *S3* shown in Figure 4.2 has **sql** topological type and represents low-dimensional subnet, since S1 and S2 are 3-dimensional. In the same way, **pcu** is the supernet with respect to **cds**, **ths** and **sql** nets. All mentioned topological types are designated following RCSR [185] or TOPOS [186] nomenclatures.
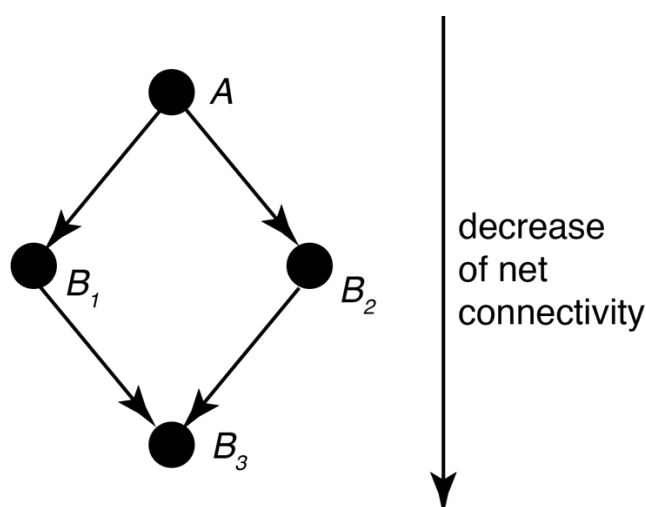
Figure 4.3. Relations between structure topologies, where A is original topology and *B1, B2, B3* are subnets of *A*.

The relations between supernets and subnets can be represented as a net relation graph (NRG), where the vertices of the graph correspond to the nets and edges correspond to a topological transformation (connect the subnet-supernet pairs) [187]. The NRG is the map with many different paths, where we can find many ways how one net can be converted into another one. As shown in Figure 4.3, A is a supernet for B_1, B_2 and B_1, B_2 are supernets for B_3. Also, one can see that topological transformation from B_1 to B_2 can go through the A or B_3 topologies.

The investigation of the net relations between topologies of crystal structures made a real breakthrough in the question of the solid-solid phase transition description. The original idea of this approach is presented in the study of Blatov et al. and called the topological network model of solid-state transformations (TNMST) [164]. This approach explains how a phase transition can be analyzed in the new configurational space — that of topological networks. In other words, the focus is shifted from the geometric aspects (lattice parameters and atomic positions) of structures to the more physical and chemical aspects of chemical bonds and the relations between topologies of the structures.
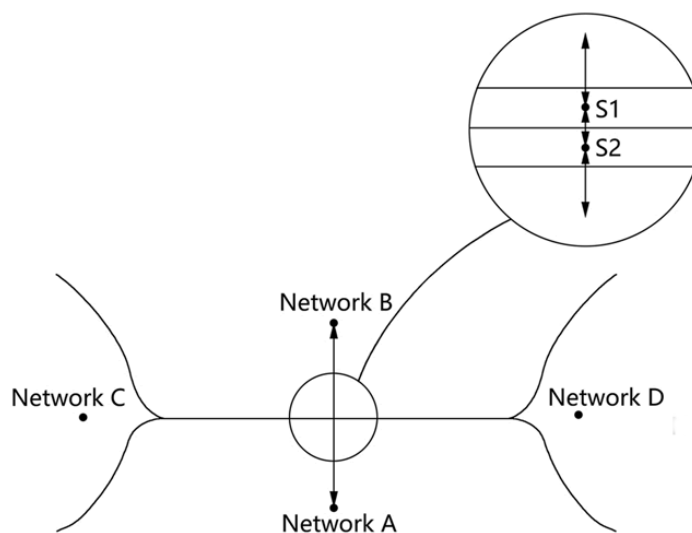
Figure 4.4. Part of configuration space with four stable network regions (A–D): a simplified representation with a linear boundary that is formed by two narrow metastable network regions (S1 is the supernet, S2 is the subnet) (reprinted from Ref [164])

Here, the crystal system is considered in terms of the network configuration space (CS) and a particular topology corresponds to each point on CS. Surely, there are network regions on CS, where the topology can be precisely determined and they are called *stable network regions*. Although, the boundaries between stable regions are representing intermediate regions, where several topologies can coexist (**Error! Reference source not found.**). For the particular structure, several topologies can be defined depending on the bond length cutoff parameter. For example, some interatomic contacts can be treated as additional bonds and opposite, some bonds can be skipped. The results of both representations are supernet and subnet, respectively. These configurations are metastable network regions and correspond to the subnets or supernets of the nets from stable network regions.

The determination of net edges is not a strict and precise procedure, thus in this model, the CS has been simplified and metastable network regions are represented as narrow lines between the stable regions (**Error! Reference source not found.**).

As a result, the authors proposed the description of the CS [164], where the crystal structure within the region on configurational space of local minimum (LM) or TS can be represented as a periodic graph (net) and the adjacency of these regions can be described as the subnet-supernet relations [187,188]. The model provides a list of formulations that govern phase transitions in solids in specific CS. So, the most important aspects of the TNMST for the structure mapping algorithm are:

1. Any region around local minima (LM) on the configurational space is presented by a unique topology and can be considered as a *topologically stable region*. And the *topologically stable regions* with different topologies do not cross each other. Transition state (TS) is located on the border of several *topologically stable regions.*

2. Any transition path crosses at least one boundary between topologically stable regions. Transition $T_A \rightarrow T_B$ with a direct supernet-subnet relation corresponds immediately to the transformation of nets into each other on the boundary. In the case without direct supernet-subnet relation, the transition will go through the transition state T_S (i.e., $T_A \rightarrow T_S \rightarrow T_B$ phase transition). T_S represents the boundary and the path crossing point. From the topological point of view, T_S is the supernet-subnet pair and each of them equally describes the transition.

3. Any common subnet/supernet of T_A and T_B bears all information common to both nets; different common subnets reflect different properties common to A and B.

4. We assume energetically more favorable are those paths, which cross the least number of boundaries on the CS.

5. The symmetry of the transition state G should be as large as possible and be a common subgroup of the space groups of $T_A(G_A)$ and $T_B(G_B)$; the index of G in G_A and G_B should be as small as possible. Consequently, the number of non-equivalent nodes/atoms (or *nodality*) in the subnet/supernet should not be too high.

6. The minimal supernets and maximal subnets can be considered as the most promising candidates for the transition.

The net has an infinite number of different subnets/supernets, but for a given nodality, this number is finite and there is a restriction for nodality. The total number of different subnets/supernets that must be considered for both structures is finite, but only several nets are common subnets/supernets for both structures. Most promising is the transition through a maximal subnet (or minimal supernet) with low nodality and high symmetry.

As was mentioned, for the interpretation of reconstructive phase transitions, it is necessary to understand the relations of supernets and subnets between structures [187]. In general, the subnet of a

net is formed by subsets of nodes and subsets of edges of the supernet and the subnet can be considered part of the supernet. During the transition, the chemical composition of structures is unchanged, the subnets that contain the same number of nodes are considered. From a chemical point of view, during the transition, some bonds are broken from the supernet to the subnet or bonds are created from the subnet or the supernet – both variants are equivalent.

It is easy to intuitively understand that the path is more energetically favorable when the number of broken and newly created bonds is as small as possible. This model can easily describe many phase transitions in solids because structures are in direct supernet-subnet relations. A good example of such transition is the transition from the rock salt topological type (**pcu-b**, CN = 6) to zinc blende type (**dia-b**; CN = 4) corresponding to the relation **pcu-b** − **dia-b** in the net relation graph. However, not every transition structure has a direct supernet-subnet relation, though the transition can always be represented in the net relation graph as a set of edges. Thus, each transition between crystal structures passes through a TS, which is described by a common subnet or supernet of both structures. The transition pathway with the lowest activation energy of the transition state is expected to represent a minimal number of bonds that should be broken and created from the topological side. And when the common subnet and supernet for both structures are defined, it can be obtained which bonds undergo changes during phase transitions.

Unfortunately, any topology can be geometrically realized in an infinite number of structures (called embeddings into Euclidean space), but luckily not all of these realizations fit the network symmetry. The network symmetry is described by an automorphism group, which is isomorphic to the space group G of the most symmetrical embedding of the network [189]. Different geometrical embeddings can have symmetry, which is a subgroup of G or coincide with G. This imposes additional conditions: the subnet and supernet embeddings in the transition state must be in a group-subgroup relation or, in other words, belong to the same Barnighausen tree [190]. The symmetry of the transition state $G(S)$ between the A and B nets cannot be higher than $G(A)$ or $G(B)$; $G(S)$ must be a common subgroup of $G(A)$ and $G(B)$. Thus, the corresponding common subnet/supernet S of A and B exists in the transition state in an embedding of the $G(S)$ symmetry; the maximal symmetry of S can be higher but must be a supergroup of $G(S)$.

The principles of TNMST, including the determination of the supernet-subnet relations, are implemented in the ToposPro code [191] and it has been used for the topological analysis of some phase transformations in the Thesis. But it provides only topological mapping data, which contains the edge-to-edge mapping between structures. Thus, a self-written code has been developed to interpret the topological mapping data and convert it into a geometrical pathway.

According to previously defined rules of the phase transition topological description, the following algorithm has been used for structures mapping and consists of the following steps:

1. The topology networks of both structures A and B are defined and denoted as T_A and T_B.

2. Both networks have been decomposed by symmetry. Next, in the resulting datasets, we search for items of common space group and the number of atoms. All other networks in both datasets we leave aside and do not consider anymore. As a result, we have two datasets D_A and D_B.

3. For all networks left in both datasets D_A and D_B we produce new datasets by cutting all possible combinations of inequivalent bonds. The number of bonds in the set varies from 1 to N symmetrical, where N is the maximal coordination number of atoms. Such an approach produces a plethora of new networks for both datasets, and among them, we must find common networks. At this step, when such networks are found, we classify them as common subnets of T_A and T_B and all other networks in both datasets we leave aside and do not consider anymore. The resulting datasets are denoted as $D_A{}'$ and $D_B{}'$. Subnets in $D_A{}'$ and $D_B{}'$ may have different number of nodes, symmetries.

4. As a rule, while common subnets are found, there must be common supernets for such transition. Thus, for all structures in both datasets $D_A{}'$ and $D_B{}'$, we generate new datasets by forming new edges from second and further coordination shells. Indeed, edges from the second coordination shell are more preferable because they correspond to the lowest displacements for all atoms during the transition. When these two datasets are formed, we denote them as $D_A{}''$ and $D_B{}''$, respectively, and next we search for items which correspond to T_B in D_A'' dataset and items which correspond to T_A in D_B''. Found items stay in datasets D_A'' and D_B'' and all others we leave aside. Next, in both datasets, we restore bonds cut on step 3 and get the candidates to the parents of the supernet.

5. At this step, in both datasets, we seek items with equal nodality and equal space group. When we find such matched structures, we group them for further topological mapping analysis. Each group corresponds to the unique pair of parameters – nodality +spacegroup.

Finally, after all manipulations with topological networks, we have a bunch of groups, each group strictly contains at least one network made from T_A (let us denote it as T_A') and at least one made from T_B (let us denote it as T_B') and for each possible pair nets like (T_A', T_B') the results next will be converted into the atom-to-atom mapping.

Since we already matched both structures in terms of topological nets (edge-to-edge correspondence) with equal supernet, nodality and spacegroup, the matched nets are represented on the structures with an equal number of atoms in the cell; thus, we can interpret this data into the geometrical (atom-to-atom) mapping.

Each group generated by the previous part of the algorithm will be considered separately from others. In the selected group for each net T_A'-type we map with other nets of T_B'-type and if we match

topologies, we get strict correspondence between interatomic connections in the initial structure and final. Such topological mapping is written in a format:

$$ID \ X_i \ r_i \ - \ X_f \ r_f \ b_1, b_2, \dots$$

where ID is the identifier of the selected mapping line, X is a chemical symbol of the initial atom, r is the fractional coordinate of the atom, b1,b2… are ids of end atoms of the bonds for this particular atom. Indices *i* and *f* mean the initial and the final structures. When the mapping between interatomic connections is defined, it is easy to get the atom-to-atom correspondence. And as a result, after this step, we get a number of possible mappings, each of them contains three things: a geometric representation of both structures, atomic mapping and topological mapping.
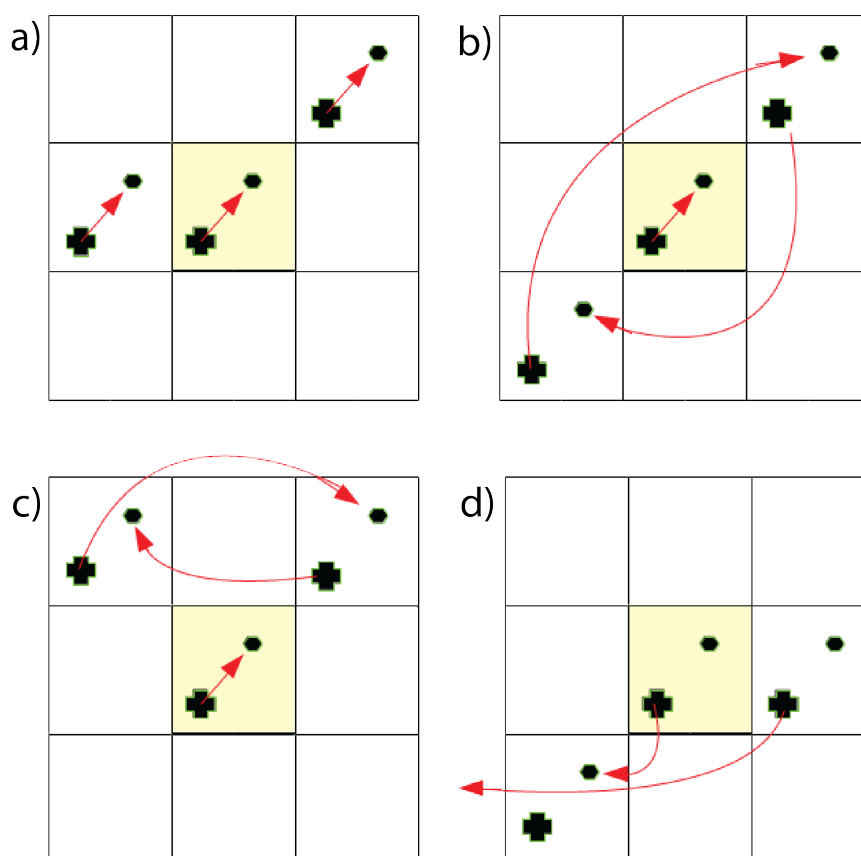
Figure 4.5. Types of transitions generated by ToposPro. '+' is the initial position, '●' is the final position in scaled coordinates.

The results obtained from the topological analysis need to be examined. The goal of this examination is to find mappings that can describe the transition in infinite crystals. In other words, such mappings will lead to the initial pathway without intersections of atoms trajectories during the transition. For all atom-to-atom mapping, the atom in position '+' always goes into the position '●' as presumed. It was found that the topological mapping algorithm generates transitions with several different schemes and some of them are shown in Figure 4.5. The illustration in the upper left corner corresponds to a transition that happens fully periodically and atom trajectories do not intersect. However, such condition will not always be satisfied and generated initial pathway will have atoms

43

trajectories intersection as illustrated in Figure 4.5b-d. Thus, such cases must be skipped for further consideration. As a result, only fully periodic atom-to-atom mappings will be considered for the initial pathways generation.

4.2   Initial path generation

Still, the result, as well as the computing time of any chain-of-states algorithm, are highly dependent on whether the proposed initial guess of the pathway is close to real MEP. Hence, generated initial pathways give us hints on how particles are moving during the phase transition, leading to an intuitive understanding of whether this transition is realistic or not. By default, the initial pathway is generated by the linear interpolation (*LI*) approach, artificially perverting the trajectories and often lowering the quality of the initial guess. This is because for some intermediate images, atoms inside the structure will come too close to each other and optimization of this pathway will take a much longer time.

The chain-of-states methods involve finding a discrete representation of the MEP. The starting point for the initial path generation of the phase transition of crystal structures consists of vectors r^{init} and r^{final}, which are representing initial and final states. Here, r will denote the vector of 3*N*+3 coordinates of the lattice vectors $\{a, b, c\}$ and atomic positions $\{r_1, r_2 \dots r_N\}$ in a given configuration, $r = \{a, b, c, r_1, r_2 \dots r_N\}$, where *N* is a number of atoms in the cell and a linear interpolation of these coordinates of the two endpoint configurations is most commonly used as an initial path in NEB calculations and can be written in the following way:

$$r^k = r^{init} + \frac{k}{Q} \cdot \left(r^{final} - r^{init}\right) \tag{4.2}$$

where index k denotes the image number in the path and runs from 1 to Q and the path will have $Q - 1$ intermediate images.

After applying the *LI* approach for each previously obtained atom-to-atom mapping, an abundance of initial pathways have been obtained and each of them must be refined by the chain-of-states optimization algorithm.

4.3   Pathway(s) optimization

Since the set of initial pathways have been generated, the pathway optimization has been made by the Variable Cell Nudged Elastic Band (VCNEB) method.

4.3.1 Variable Cell Nudged Elastic Band

A set of images $\{X_1, X_2, \dots, X_i, \dots X_N\}$ connecting the two endpoints X_1 and X_N represent the discrete version of the transition pathway in the VCNEB method, like in the original NEB method. Here, X_i-th is a vector that contains the *i*-th image coordinates in a special configuration space. The

transition path is adjusted according to the initial one by the "virtual" springs that connect neighboring images and employing the force orthogonal to the pathway. After the convergence, the resulting chain of images tends to be MEP.

Contrary to the original NEB method, in the VCNEB method, the configuration space and the force vectors form an expanded vector that has components from the cell and atomic positions. Both parameters are transformed to have the same dimensionality.

The unit cell of a crystal is presented as a variable matrix of lattice vectors $\boldsymbol{h} = \{\vec{a}, \vec{b}, \vec{c}\}$, with a volume of $\Omega = \det(\boldsymbol{h})$. In the variable cell NEB technique [192–194], the finite strain tensor ϵ as a free variable is always chosen, instead of the lattice vector h, for the sake of convenience. Thus we can replace $\boldsymbol{h_0}$ as a reference configuration by $\boldsymbol{h} = \boldsymbol{h_0}(1 + \epsilon)$, where ϵ includes nine components ϵ_{ij} ($i, j = 1,2,3$).

The atomic fractional coordinates r_ν ($\nu = 1,2,\dots,N$) represent positions of all ν-th atoms. The full configuration space is described by the vector $X = (\epsilon_{1i}, \epsilon_{2i}, \epsilon_{3i}; r_1, r_2, \dots, r_N)$ ($i, j = 1,2,3$), with $9 + 3N$ components.

Under the applied pressure P, the enthalpy $H = E + PV$ is determined by the $9 + 3N$-dimensional energy surface — the "enthalpy surface"

$$H = H(\epsilon_{1i}, \epsilon_{2i}, \epsilon_{3i}; r_1, r_2, \dots, r_N) \tag{4.3}$$

where E is the energy of this structure. The expanded "force vector" in a $9 + 3N$ configuration space can be defined by the derivative of the enthalpy with respect to X as follows

$$F = -\left(\frac{\partial H}{\partial X}\right)_P \tag{4.4}$$

The strain components of F on the lattice are the derivatives of H with respect to ϵ

$$f(\epsilon) = -(\sigma + P)V \cdot (1 + \sigma^T)^{-1} \tag{4.5}$$

where σ is the quantum-mechanical stress tensor [195] at a given configuration X. The forces on atoms, $f_1, f_2, \dots, f_N$ can be obtained from the Hellmann–Feynman theorem [196]. Finally, the generalized force F can be written as [192]

$$F = (f_\epsilon, gf_1, gf_2, \dots, gf_N) \tag{4.6}$$

where the metric tensor $g = \boldsymbol{h}^T \cdot \boldsymbol{h}$ is introduced to keep the symmetry during structure relaxation [192,193].
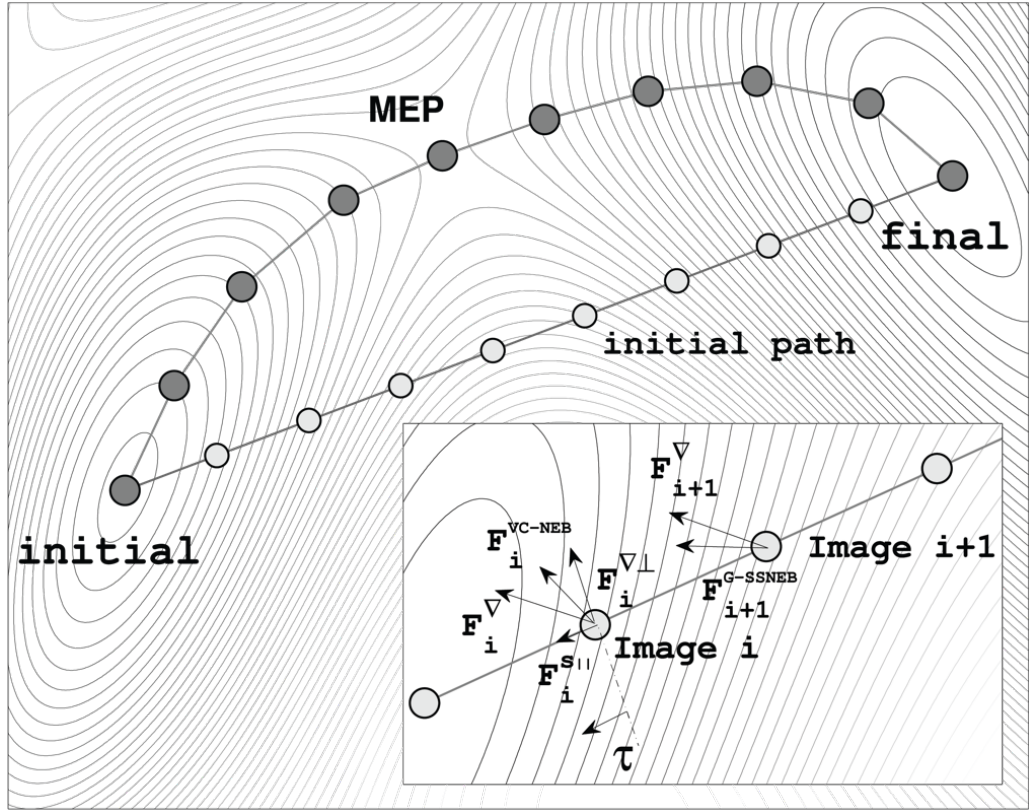
Figure 4.6. The minimum energy path (line with gray cycle) and initial path are described on the enthalpy surface. The forces in the VCNEB method on Image i are shown in the inset. $\boldsymbol{F}_i^{\nabla}$ is the potential force in the gradient direction. $\boldsymbol{F}_i^{\nabla\perp}$ and $\boldsymbol{F}_i^{S\parallel}$ are the transverse component of $\boldsymbol{F}_i^{\nabla}$ and the spring force, respectively (Reprinted from Ref [163]).

The tangent vector τ represents the unit vector to neighboring images and is directed along the path [158,197,198]. The transverse components of the potential forces acting on the lattice are denoted as $f_\epsilon^{\nabla\perp}$ and forces acting on atoms are denoted as $f_v^{\nabla\perp}$. $f_\epsilon^{S\parallel}$ and $f_v^{S\parallel}$ represent the nudging spring forces acting on lattice and atoms, respectively. They keep the image spacings in the pathway. Now one can define the VCNEB force F^{VCNEB}, the cell force $\boldsymbol{F}_\epsilon^{VCNEB}$ acting to reshape the new image of the cell, and the atom force $\boldsymbol{F}_v^{VCNEB}$ shifting the atoms

$$f_\epsilon^{VCNEB} = f_\epsilon^{\nabla\perp} + f_\epsilon^{S\parallel} \tag{4.7}$$

$$f_v^{VCNEB} = f_v^{\nabla\perp} + f_v^{S\parallel} \tag{4.8}$$

$$\boldsymbol{F}^{VCNEB} = (f_\epsilon^{VCNEB}, gf_1^{VCNEB}, gf_2^{VCNEB}, \dots, gf_N^{VCNEB}) \tag{4.9}$$

In the VCNEB method, the basic idea is to search the MEPs by studying the ''enthalpy surface'' instead of the "potential energy surface" [199] in the traditional NEB method. When applying the VC-NEB method to reconstructive phase transitions, the transition path is determined by finding the MEPs on the enthalpy surface in a larger (9+3N)-dimensional configuration space, combining the unit cell and atomic variables. The images along the path are relaxed to MEPs through $\boldsymbol{F}^{VCNEB}$, which

contain the transverse components of the potential forces $F^{\nabla\perp}$ and the spring forces $F^{S\parallel}$ (Fig. 1). Along with the VCNEB method there exists a generalized solid-state NEB (G-SSNEB) method proposed by Sheppard et al. [162]. G-SSNEB method investigates the solid–solid transformations involving the unit-cell and atomic degrees of freedom, using scaled stress with a Jacobian term along the steepest-descent direction and the atomic forces. The VCNEB and G-SSNEB methods treat the problem in different metric spaces [200] and have a significant technical difference. In the VCNEB method, all the components of the general forces are along the gradient direction on the enthalpy surface, whereas in the G-SSNEB method, they are replaced by the true lattice force (the derivative of energy). For the latter, the computation is implemented under the assumption of an isotropic elastic medium with a Poisson ratio of zero, while this unjustified assumption is not needed in our VCNEB method.

4.3.2 Implementation of VCNEB

To perform a VCNEB calculation for the description of phase transition between two structures, the initial pathway represented by a set of intermediate images must be defined. As has been shown before, usually, it is the linear interpolation between two given endpoint images. However, it can be the user-provided specific configurations.

By starting from the initial path, the images are relaxed to the MEP through the VCNEB force F^{VCNEB} derived from the force and stress tensors calculated by the popular empirical (GULP [201]) and *ab initio* (Quantum ESPRESSO [202,203] and VASP [204]) codes. The variable-elastic-constant, improved-tangent-estimate and climbing-image NEB schemes [197,198,205] are also implemented in VCNEB code for accurate saddle point determination. The VCNEB calculation will stop when the user-defined convergence conditions on force and enthalpy have been satisfied.
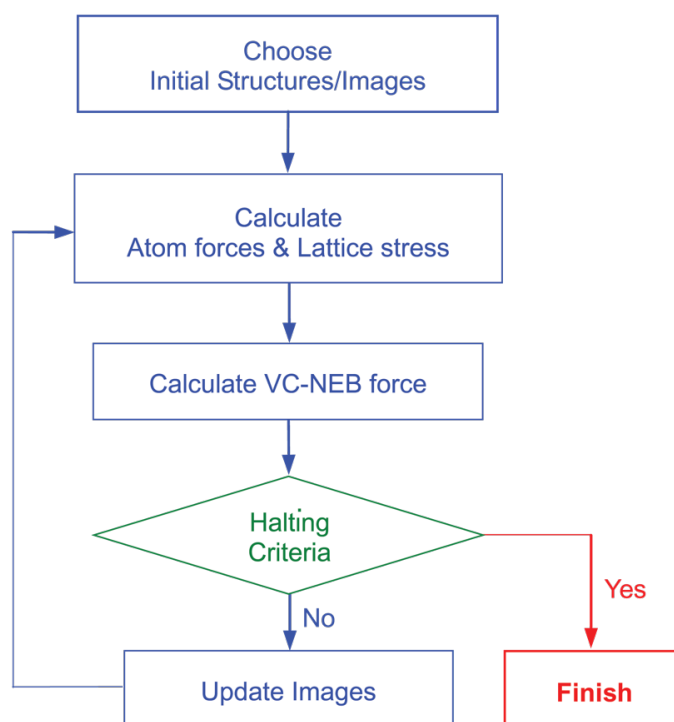
Figure 4.7. The basic procedure of the VCNEB technique (Reprinted from Ref [163]).

For the previously obtained initial pathway, the basic procedure of the VCNEB technique is as follows, as shown in Figure 4.7:

1. Calculate the stress on the lattice and the forces on the atoms in the intermediate images from first principles.

2. Calculate the VCNEB forces based on the stress on the lattice and the forces on the atoms by determining the tangent vector τ with the vector $X = (\epsilon_{1i}, \epsilon_{2i}, \epsilon_{3i}; r_1, r_2, \ldots, r_N)$ (i = 1, 2, 3) for intermediate images.

3. Calculate the displacement of atoms and the transformation strain for the cell based on the calculated VCNEB forces by using the optimization algorithm. As a result, a new set of images will be generated.

4. Repeat steps (1)–(3) until the halting criteria are satisfied.

As a result, the set of optimized pathways are obtained with a lot of meaningful data, including the transition energy profile, structure evolution, cell parameters change of the investigated transition and much more. The main focus here is the TS – its energy, height of the barrier and geometry. Finally, among all optimized pathways, the best (with the lowest energy barrier) is chosen.

In conclusion, two important remarks must be made concerning all phase transition mechanisms. First, the transition mechanism, which will further be discussed, is the best mechanism among those tested; i.e., it has the lowest activation barrier. However, other mechanisms with a lower transition barrier are not excluded since the global optimization of phase transition paths was not performed and robust methods for doing so still do not exist. Second, the phase transition mechanisms

are based on the mean-field approximation, where all unit cells behave identically and simultaneously. As has been mentioned before, phase transitions are proceeding via nucleation and growth and the presented methodology is a rough but crystallographically and intuitively clear model.

4.4 Workflow

All steps described above in this section are combined in the unique workflow for the phase transition simulation in solids. The developed workflow is illustrated in Figure 4.8.
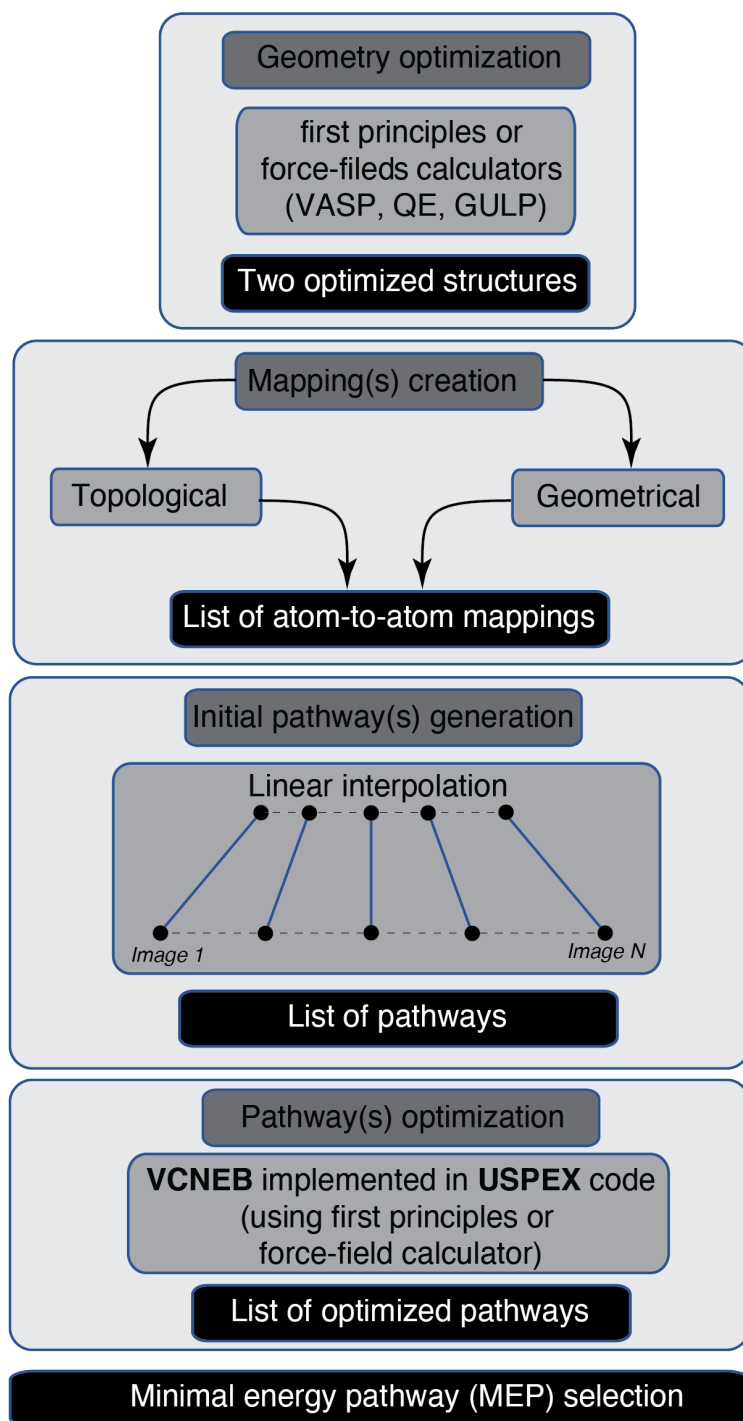
Figure 4.8. The workflow for the Minimal energy pathway search.

4.5 Computational methods

4.5.1 Geometry optimization

For every single simulation, in the beginning, structure relaxation of the studied system should be carried out. So, the atomic forces, cell stresses and total energy calculations were performed using density functional theory (DFT) [206,207] within the generalized gradient approximation (Perdew-Burke-Ernzerhof functional) [208], and the projector augmented wave method [209,210] as implemented in the VASP [204,211,212] package. The Monkhorst–Pack scheme [213] was used to sample the Brillouin zone. The details of other parameters will be noted for each particular system in **Results** section.

4.5.2 Mapping

A geometric mapping algorithm made by Stevanovic and co-workers [170,171] has been used to generate a set of mappings. Topological mapping has been performed using TOPOS crystal-chemistry package [191]. Translation of the mapping data into chain-of-states pathway and validation of obtained pathways have been performed by the hand-written code.

4.5.3 Pathway optimization

Each of the produced initial pathways has been optimized and to reveal the mechanism of structural phase transition, we performed variable-cell nudged-elastic-band (VCNEB) [163] simulations, as implemented in the USPEX code [117,121]. Besides the energy estimation, VCNEB calculations require atomic forces and cell stresses calculation, all of them were computed with projector-augmented wave pseudopotentials (PAW) on the Vienna Ab initio Simulation Package (VASP) developed by Kresse and Furthmüller [204] at the Perdew-Burke-Ernzerhof generalized gradient approximation (PBE-GGA) level of theory [208]. The climbing image − descending image technique [197] was used to precisely locate transition states (TSs). The FIRE optimizer [214] has been chosen. The halting criteria of the calculation are met when the maximum magnitude VCNEB-force among all images is less than some predefined value. For each particular system, this value will be specified in **Results** section. The time step, maximum number of steps, number of images in the pathway and value of the spring constants will also be specified for each particular system in **Results** section.

Crystal structures of predicted phases were generated using VESTA software [215].

5 RESULTS AND DISCUSSIONS

The main result of this Thesis is the development of the topology-based approach for the initial path generation and the adaptation of the geometrical mapping approach with its further application for MEP search. The summary of all steps for the MEP search is presented as a unified workflow presented in **Workflow** section in **Methodology** chapter.

I describe below how the proposed unified workflow has been used to investigate phase transitions in superhard chromium nitrides, calcites, tungsten borides and between andalusite, sillimanite and kyanite phases of Al_2SiO_5.

5.1 Mechanism of the phase transition in CrN: from NaCl-type to WC-type structure.

Generally, the hardest and most popular superhard materials belong to two groups – (1) some B-C-N compounds and their derivatives (e.g., Refs. [216,217]), and (2) nitrides, carbides and borides of some transition metals. Compounds of the first class are semiconducting and brittle and the best known superhard phases (i.e., with Vickers hardness > 40 GPa) belong to it, whereas those of the second class are metallic and more ductile. A recent study made by Kvashnin et al. [218] has been devoted to search for the material with the best hardness (computed using the Lyakhov-Oganov model [219]), where the list of new promising hard and superhard Cr-B, Cr-C and Cr-N systems has been studied. Several theoretical studies of chromium nitrides and borides reported that CrB_4 and hypothetical metastable CrN_2 have to be superhard [218,220–222].

Usually, chromium metal and its compounds are used in a wide range of applications mainly related to cutting tools [223,224] and wear-resistant coatings [225–228]. Chromium nitride, CrN, is often used on medical implants and tools as a coating material due to its good wear, oxidation and corrosion resistance [225–227]. CrN is also a valuable component in advanced multicomponent coating systems, such as CrAlN, for hard, wear-resistant applications on cutting tools [229].

Several experimental works devoted to chromium nitrides reported the existence of a cubic paramagnetic B1-phase (NaCl-type) with chemical formula CrN and $Fm\overline{3}m$ space group [230,231]. However, at temperatures below the Néel temperature (200-287 K) [231–234] B1-CrN phase transforms to an orthorhombic antiferromagnetic phase with $Pnma$ space group [231,233] and this transition was studied theoretically [235]. Today, electronic and magnetic properties of chromium nitride at low temperatures are actively studied [231,235–238].

In addition to CrN, there is another stable compound Cr_2N, which appears together with CrN during the fabrication of Cr-N films and displays comparable wear resistance, but worse oxidation resistance [239–242]. Theoretically predicted crystal structure of Cr_2N [243] was based on experimental data

obtained by Eriksson [244], who reported about hexagonal close-packed structure with $P\bar{3}1m$ space group with lattice parameters a=4.752 Å, c=4.429 Å. Comprehensive first-principles calculations of atomic structure and physical properties of different Cr_2N phases [245] were provided. However, the only work on the global optimization of Cr-N systems was done by Kvashnin et al. [218]. A convex hull diagram was constructed based on the calculated enthalpies of formation of predicted phases at zero pressure for different compositions, as shown in Figure 5.1a. Red and white points in the convex hull diagram correspond to thermodynamically stable and metastable phases, respectively. The results of Pareto optimization [v] shown in Figure 5.1b. All points, which belong to a certain Pareto front, are connected by black line. The first Pareto front contains phases with simultaneously optimal high hardness (estimated using Lyakhov-Oganov model [219]) and maximum stability (measured as vertical distance from the convex hull). The phases located in the first Pareto fronts, shown by red circles, lie on the convex hull or close to it (see Figure 5.1b).

---

[v] Pareto optimization is the method for the multiobjective optimization problem, where more than one objective, which have to be optimized simultaneously.
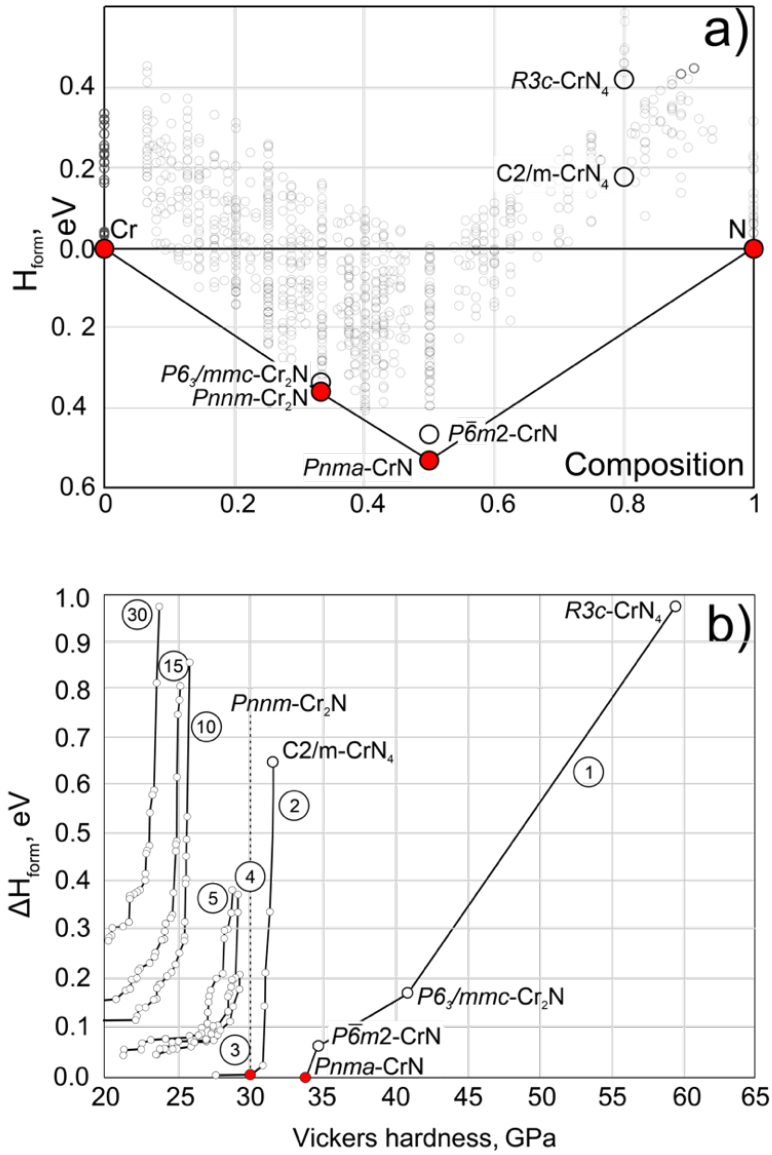
Figure 5.1. a) Convex hull diagram of Cr-N system and b) results of Pareto optimization in terms of formation enthalpies and Vickers hardness, computed using the Lyakhov-Oganov model [219] for Cr-N system. Numbers in circles denote the number of Pareto front. Full and open circles are stable and metastable phases, full triangles – one-component phases (reprinted from Ref. [218])

Results of Pareto optimization of the Cr-N system show that thermodynamically stable CrN and Cr_2N phases display hardness up to 30 GPa. The ideal strength of $Pnma$-CrN, $P\bar{6}m2$-CrN, $Pnnm$-Cr_2N and $R3c$-CrN_4 phases, to be equal to 38.2, 41.7, 37.3 and 24.2 GPa, respectively. At the same time, new $P\bar{6}m2$ phase has been predicted. From this perspective, the structural phase transition from the previously known $Pnma$-CrN phase to $P\bar{6}m2$-CrN attracted our attention. $Pnma$-CrN phase has a NaCl-type structure with an orthorhombic distortion due to antiferromagnetic ordering, while predicted $P\bar{6}m2$-CrN is isostructural to tungsten carbide (WC) as shown in Figure 5.2. The structural similarity suggests that $P\bar{6}m2$-CrN may have outstanding mechanical properties similar to those of WC.
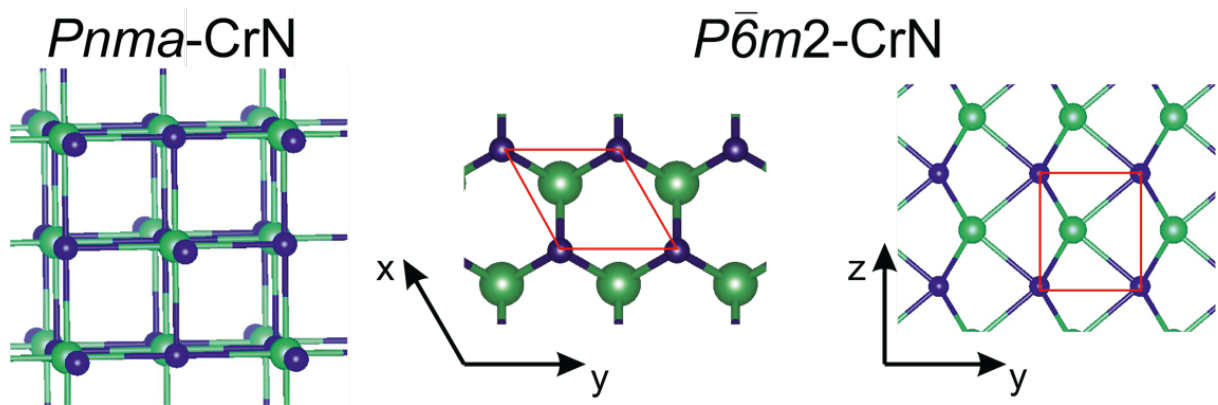
Figure 5.2. Crystal structures of CrN phases. Green spheres – Cr atoms, blue – N atoms
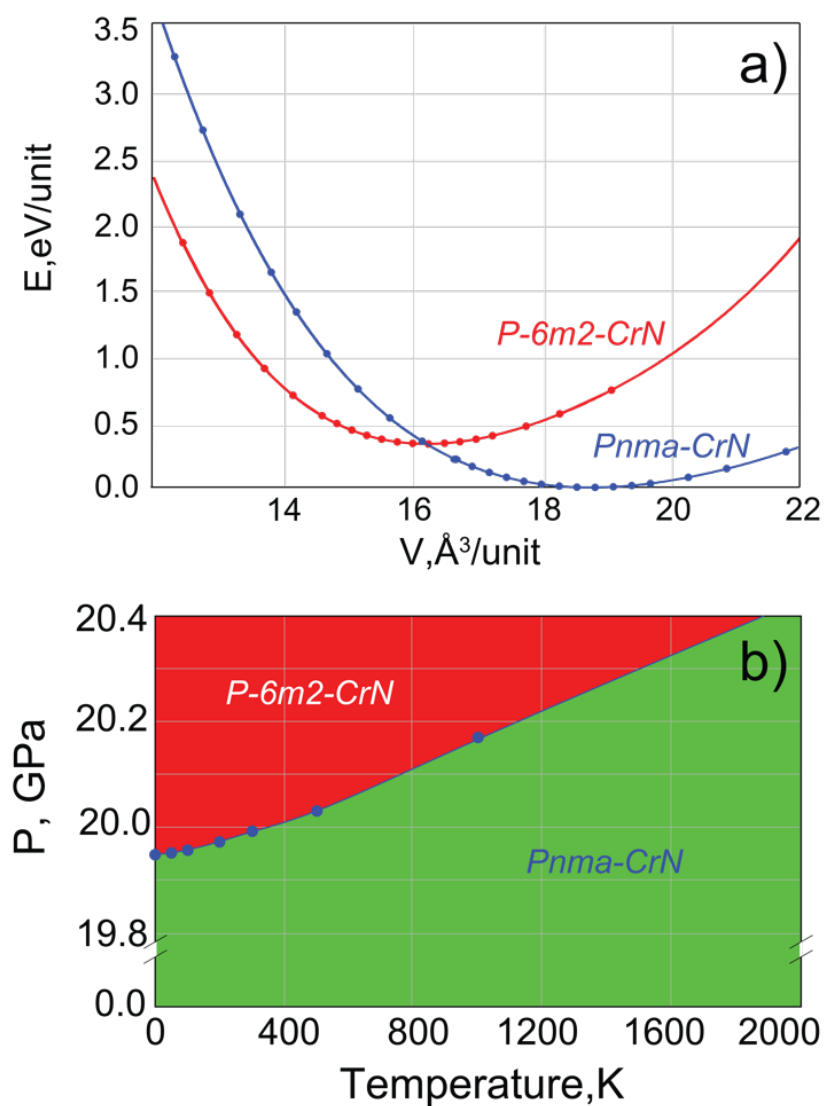
Figure 5.3. a) Energy per stoichiometry unit as a function of volume for both of considered CrN phases, b) Phase diagram of CrN (reprinted from Ref. [218])

The dependences of the total energy on the volume of *Pnma* and *P6̄m2* phases are shown in Figure 5.3a. Conditions for the experimental synthesis of CrN phases were estimated by computing

phase diagrams, shown in Figure 5.3b, where $Pnma \rightarrow P\bar{6}m2$ phase transition pressure at 0 K equals to 19.9 GPa, which is readily achievable in experiments.

The convex hull diagrams of Cr-N phases were calculated at the pressures of 0, 10, 20 and 30 GPa as shown in Figure 5.4. We see the same stable compositions as at zero pressure and at 30 GPa $P\bar{6}m2$-CrN phase becomes more stable than $Pnma$-CrN.
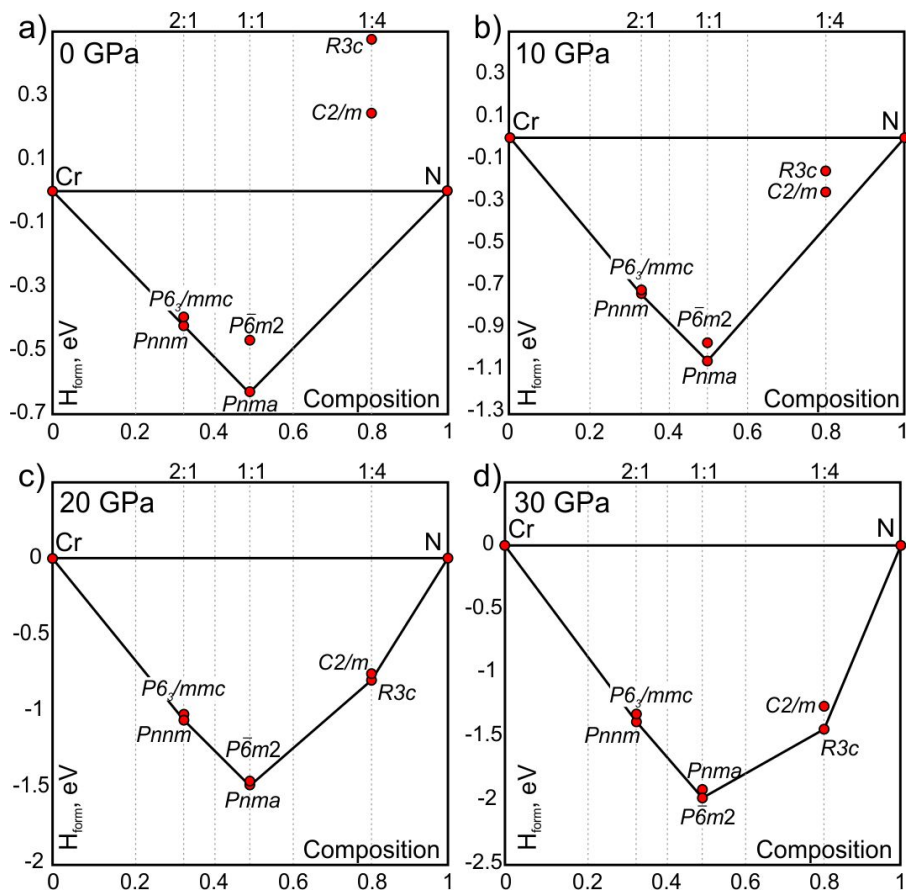
Figure 5.4. Convex hull diagrams for Cr-N system at a) 0 GPa, b) 10 GPa, c) 20 GPa, d) 30 GPa (reprinted from Ref. [218])

My contribution to this work was investigating the phase transition mechanism from $Pnma$-CrN to newly predicted $P\bar{6}m2$-CrN.

5.1.1 Calculation details

The structural phase transition from $Pnma$-CrN to newly predicted $P\bar{6}m2$-CrN was calculated at 0 GPa. As has been mentioned in **Geometry optimization** section of **Methodology** chapter, first of all, both structures have to be well optimized. It is important to note that for CrN phases has been used the Hubbard U-term correction – detailed information on the choice of U-J parameter described below. The plane–wave energy cutoff of 600 eV was used, ensuring excellent convergence of total energies, forces and stresses. The mappings were generated by the topological mapping approach (see **Topological mapping** paragraph). The initial pathways were generated using the linear interpolation approach as described in **Initial pathway** section from the obtained mappings. Each of all generated

initial pathways was subsequently refined by VCNEB method as discussed in **Pathway optimization** section. VCNEB calculations started with 10 intermediate images (structures), and this number was automatically increased whenever the path became longer. Spring constants varied from 3 to 6 eV/Å^2. The halting criterion for the calculation was set as RMS (Root Mean Square forces) on images that are less than 0.01 eV/Å.

5.1.1.1 *Details of U-J calculations*

For different properties of interest, very different values of U-J are optimal. For our purposes of finding thermodynamically stable compounds, the most important quantity is the enthalpy of formation: we calculated the enthalpy of formation of CrN at different values of the U-J parameter from 0 to 5 eV and compared them with experimental data taken from Ref. [246] (ΔH= 0.64 eV/atom). We found that U-J = 1 eV gives the enthalpy of formation of 0.53 eV/atom, which is in good agreement with reference data [246]. We also found that the GGA+U approach with U- J = 1 eV predicts the structural parameters of considered CrN system accurately: a_{calc} = 4.189 Å, a_{exp} = 4.148 Å (Ref [247]), V_{calc} = 73.35 Å^3, V_{ref} = 73.28 Å^3 (Ref [248]). Thus, we believe that value U-J=1 eV is suitable for correct description of stability and structural parameters of AFM orthorhombic CrN phase and the same U-J parameter was used for calculations of other phases in the Cr-N system.

5.1.2 Results

After optimization of the initial structures, the topological mapping has been created. Initially, the coordination of Cr and N atoms in both structures are six-coordinated. Cr and N atoms are topologically equivalent in both structures, which means that topology of both structures can be presented by uninodal (with one inequivalent atom) net. The topological type of $P\bar{6}m2$-CrN is **acs** and **pcu** for *Pnma*-CrN. These topologies are not in direct relation between each other, thus a net relation graph needs to be built (see **Topological mapping** paragraph). The trees of topologies generated from **acs** and **pcu** have several common topologies. Figure 5.5 presents the net relation graph, where common subnets for **acs** and **pcu** topologies were listed. All of mentioned common subnets, i.e. **sqp**, **vma** and **wlj,** are 5-coordinated (highest possible) and all other topologies with lower coordination have been skipped. As one can see, the list of common symmetry subgroups is not complete but represented by only a few possible subgroups. That is because each topology can only be presented by a geometrical embedding of a limited number of symmetries.
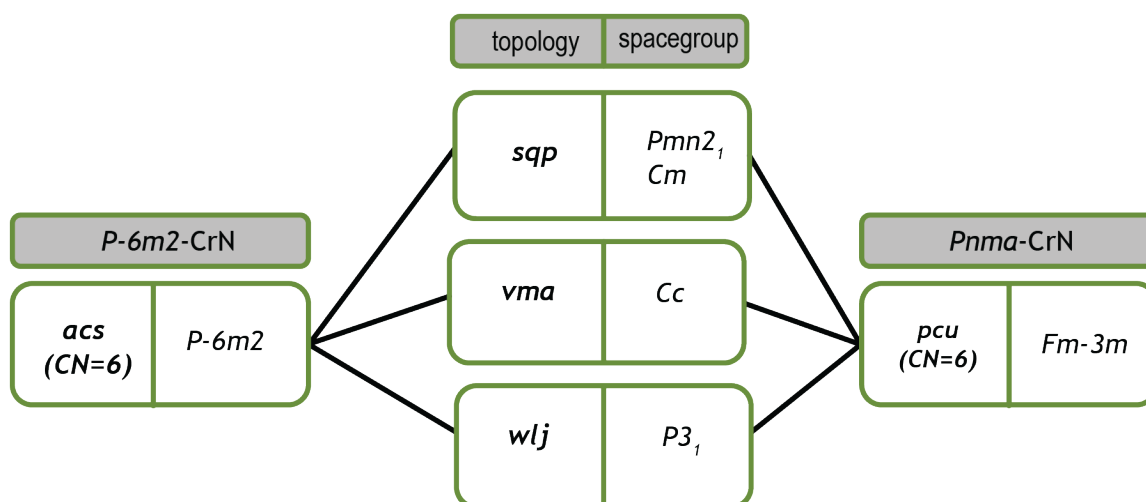
Figure 5.5. Piece of net relation graph for **acs** and **pcu** topologies with the highest coordination.

When the common subnet and common symmetry subgroups are found, the supernet of the transition needs to be found. For both **vma** and **wlj** topologies, the common supernet has not been found (**acs** or **pcu** cannot be found as subnets of generated supernets) and only for **sqp** topology the supernet **bcu-7** contains both **acs** and **pcu**. Geometric representation of **bcu-7** supernet on the geometries of $P\bar{6}m2$-CrN and $Pnma$-CrN structures helped to create an atom-to-atom mapping, which is truly periodic. As a result, only one mapping has been used for further initial pathway generation, as shown in Figure 5.6.
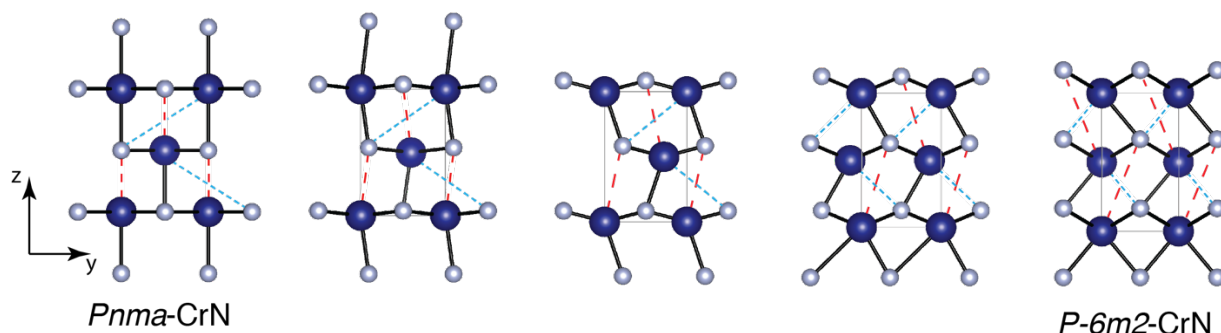
Figure 5.6. The geometrical representation of $P\bar{6}m2 \rightarrow Pnma$ (topologically: **acs** $\rightarrow$ **pcu**) transition. Black interatomic contacts represent constant chemical bonds. Red and blue dashed lines represent chemical bonds cut and created during the transition, respectively. Black+blue interatomic contacts represent **acs** topology, black+red interatomic contacts represent **pcu** topology, black+red+blue interatomic contacts represent **bcu-7** topology.

As a result, we found that $P\bar{6}m2$-CrN phase, which has WC-type crystal structure is less stable at zero pressure than $Pnma$-CrN phase by 0.21 eV per formula unit with U-J=1 eV (see Figure 5.7). Details of the calculations can be found in related publication [218]. The optimized transition path is shown on the top panel of Figure 5.7. Two transition states denoted as TS1 and TS2 were found along with an intermediate structure (IS) with Pm space group. Direct transition barrier from $Pnma$ to IS

structure is 0.47 eV per formula unit. Transition state TS2 is located 0.28 eV/unit higher than IS. The reverse transition from $P\bar{6}m2$ phase is accompanied by the barrier of 0.31 eV/unit.
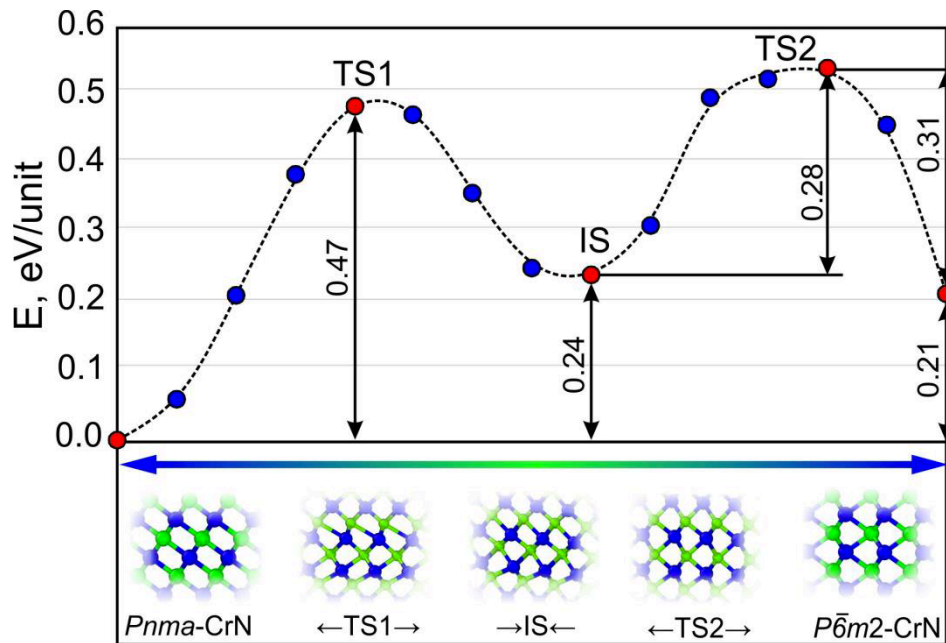
Figure 5.7. The $Pnma \rightarrow P\bar{6}m2$ transition of CrN at 0 GPa and 0 K. Structures of initial $Pnma$ phase, transition states TS1 and TS2, intermediate structure (IS) and final $P\bar{6}m2$ phase of CrN are shown on the bottom.

It should be noted that intermediate structure consists of alternation of layers of $Pnma$ and $P\bar{6}m2$ structures with the energy higher than $Pnma$ phase by 0.24 eV/unit and than $P\bar{6}m2$ by 0.03 eV/unit. High barrier indicates that high temperatures are necessary to kinetically enable this transition.

5.2 Mechanism of the sp^2-sp^3 transition in CaCO$_3$

The exceptional ability of carbon to form sp^2 and sp^3 bonding states leads to a great structural and chemical diversity of carbon-bearing phases at nonambient conditions and carbonates are not an exception. Graphite is the ground state of carbon at ambient conditions with a triangular bonding pattern (sp^2 hybridization). At high pressure (P), carbon tends to be tetrahedrally bonded (sp^3), and diamond is stable at P > 1.7GPa (0 K) [249]. These different bonding patterns result in very different mechanical, optical, electric, and thermal properties [250], making carbon a truly remarkable element. Along with that, carbon forms very strong bonds, leading to high melting temperatures and high activation energies for the solid-state phase transitions [249]. As a result, a number of carbon-based metastable phases with mixed sp^2 and sp^3 bonding patterns exist that combine unique physical properties of both graphite and diamond [251,252]. The synthesis of such novel carbon-based technological materials requires navigating in the carbon energy landscape as well as insights into the trajectories and mechanisms of its phase transitions [253].

Theoretical computations predict that sp^3 carbonates become thermodynamically stable at P > ~80–130GPa [254–258]. Lobanov et al. [259] investigated the high-P behavior of CaCO$_3$, one of the most abundant carbonates near the Earth's surface and a good proxy for carbonate chemical composition in the mantle [260,261]. It is an sp^2 carbonate at normal pressure. Previous high-P studies have revealed a number of pressure-induced transformations in CaCO$_3$. At P < ~40GPa, (meta)stable phases of CaCO$_3$ exist that include calcite, aragonite, CaCO$_3$ II, CaCO$_3$ III, CaCO$_3$ IIIB, and CaCO$_3$ VI (e.g., Refs [255,262–264]). At P > 40GPa, CaCO$_3$ transforms into postaragonite, which has been reported as a stable phase up to 137 GPa [255,265,266]. Importantly, all these structures contain sp^2-hybridized carbon forming triangular CO$_3$ groups.

Pyroxene-like $C222_1$–CaCO$_3$, which has been predicted to be stable at P > 137GPa, has a different bonding pattern, with sp^3-hybridized carbon forming polymerized CO$_4$ chains [255]. This prediction gained some experimental support in that the major Bragg peaks of the $C222_1$ CaCO$_3$ were observed in experiment at P > 140GPa [266]. The high synthesis pressure implied that sp^3 CaCO$_3$ is not present in the Earth's mantle (135 GPa is the core-mantle boundary pressure), and further experimental studies of sp^3 carbonates were shifted to other compositions. More recently, the sp^2-sp^3 transition in CaCO$_3$ was revisited by Pickard and Needs [258], who predicted a new sp^3 CaCO$_3$ phase ($P2_1/c$) at P > 76GPa, calling for a new synthesis study.

In the study made by Lobanov et al. [259], the phase transitions in CaCO$_3$ at P > 40GPa via synchrotron X-ray diffraction, Raman spectroscopy, and first-principles calculations have been explored. It has been found from X-ray diffraction that at pressure of 40–102 GPa, the $Pmmn$-CaCO$_3$ (postaragonite phase) is stable, which is in a good agreement with previous studies [255,265]. Also, has been predicted the transformation of postaragonite CaCO$_3$ phase to the previously predicted $P2_1/c$

CaCO$_3$ with sp^3-hybridized carbon at 105 GPa ($\sim$30GPa higher than the theoretically predicted crossover pressure). Also, the stability field of sp^3-bonded $P2_1/c$ CaCO$_3$ has been established and it was shown that this phase has a strong Raman band characteristic of fourfold carbon in its crystal structure. Raman spectra of $P2_1/c$ CaCO$_3$ show an intense band at 1025 cm^{-1}, which we assign to the symmetric C-O stretching vibration based on empirical and first-principles calculations. This Raman band has a frequency that is $\sim$20% lower than the symmetric C-O stretching in sp^2 CaCO$_3$ due to the increasing of C-O bond length during the sp^2-sp^3 transition and can be used as a fingerprint for tetrahedrally coordinated carbon in other carbonates.

My contribution to this work was the investigation of the phase transition mechanism from $Pmmn$-CaCO$_3$ to $P2_1/c$-CaCO$_3$. The sp^2-sp^3 phase-transition mechanism in CaCO$_3$ appears to be a complex multistage process. The lowest-enthalpy transition path includes reoccurring sp^2 and sp^3 CaCO$_3$ intermediate phases and transition states.

5.2.1 Calculation details

The structural phase transition from $P2_1/c$-CaCO$_3$ to $Pmmn$-CaCO$_3$ (postaragonite) was performed at 100 GPa. As has been mentioned in **Geometry optimization** section of **Methodology** chapter, first of all, both structures have to be well optimized. The plane–wave energy cutoff of 600 eV was used, ensuring excellent convergence of total energies, forces and stresses. Among all possible mappings for transition generated by geometrical mapping approach (see **Geometric mapping** paragraph), we chose top 10 results. Because mapping algorithm is not commutative, two sets of mappings have been generated ($P2_1/c$-CaCO$_3 \rightarrow Pmmn$-CaCO$_3$ and $Pmmn$-CaCO$_3 \rightarrow P2_1/c$-CaCO$_3$). From the obtained mappings, the initial pathways were generated using linear interpolation approach as described in **Initial pathway** section. Each of all generated initial pathways was subsequently refined by VCNEB method as presented in **Pathway optimization** section. VCNEB calculations started with 10 intermediate images (structures), and this number was automatically increased whenever the path became longer. Spring constants varied from 3 to 6 eV/Å^2. The halting criterion for the calculation was set as RMS (Root Mean Square forces) on images that are less than 0.01 eV/Å.

5.2.2 Results

At a pressure of 100 GPa, the $P2_1/c$ CaCO$_3$ phase is more stable by 0.02 eV/atom than postaragonite. The barrier height from postaragonite side is quite large, 0.14 eV/atom (or 0.70 eV/f.u.), implying that this transition is kinetically feasible only at high temperatures. One crucial distinction between the crystal structures of sp^2 and sp^3 CaCO$_3$ is that CO$_3$ groups in postaragonite are isolated, while CO$_4$ groups in $P2_1/c$ CaCO$_3$ are corner linked into pyroxenelike chains. Accordingly, the transformation mechanism from $P2_1/c$ - CaCO$_3$ to postaragonite at 100GPa is quite complex and can be divided into four stages (see Figure 5.8): each stage corresponds to an energy

minimum, and boundaries between them correspond to TSs. In the first stage of the transformation, the postaragonite structure distorts gradually, with all CO_3-triangles becoming nonplanar. This distortion becomes critical at transition state 1 (TS1), triggering the second stage of the transition with all carbon atoms forming additional bonds with oxygen atoms of the next layer, stitching isolated CO_3 groups into infinite chains of CO_4 tetrahedra. This topology corresponds to a local enthalpy minimum and has a $P2_1$ symmetry (intermediate phase 1, IP1). However, the enthalpy minimum of IP1 is very shallow (see Figure 5.8). Towards transition state TS2, one of the C-O bonds of the original CO3 triangle gradually elongates and eventually breaks. In the third stage, between transition states TS2 and TS3, yet another metastable structure with a $P2_1$ symmetry appears, featuring flat and noncoplanar CO_3 triangles and a shallow enthalpy minimum. As this structure distorts towards transition state TS3, carbonate triangles reorient, nearby oxygens displace towards them, and eventually, one obtains infinite chains of CO_4 tetrahedra in the same topology as in the $P2_1/c$ structure. The final fourth stage of the transformation is just a relaxation towards the theoretically predicted $P2_1/c$ CaCO$_3$ structure [258]. Transition states define the crossover between different topologies, i.e., the point at which chemical bonds are formed or broken. It is very tempting to think of some maximum bond lengths characteristic of a given pair of atoms (e.g., C-O), beyond which bonds break. However, this is not to be the case for $Pmmn \rightarrow P2_1/c$ transition, as the values of critical C-O bond lengths vary for different transitions. This suggests that the phase transitions are driven not just by the nearest-neighbor interactions but also by longer-range interactions while cooperative effects are essential.

One fundamental comment is necessary regarding the mechanism of this phase transition. The intermediate minima (IP1 and IP2) in this case are so shallow that they are unlikely to be quenched in the experiment: these minima are not strongly kinetically protected and will rapidly decay into postaragonite and $P2_1/c$, respectively. The role of these intermediate minima is to be "stepping-stones" on the transition pathway, lowering the overall barrier. This is in contrast to the case of BH, a newly predicted compound, where the phase transition involves a very deep and most likely experimentally obtainable, intermediate phase [267].
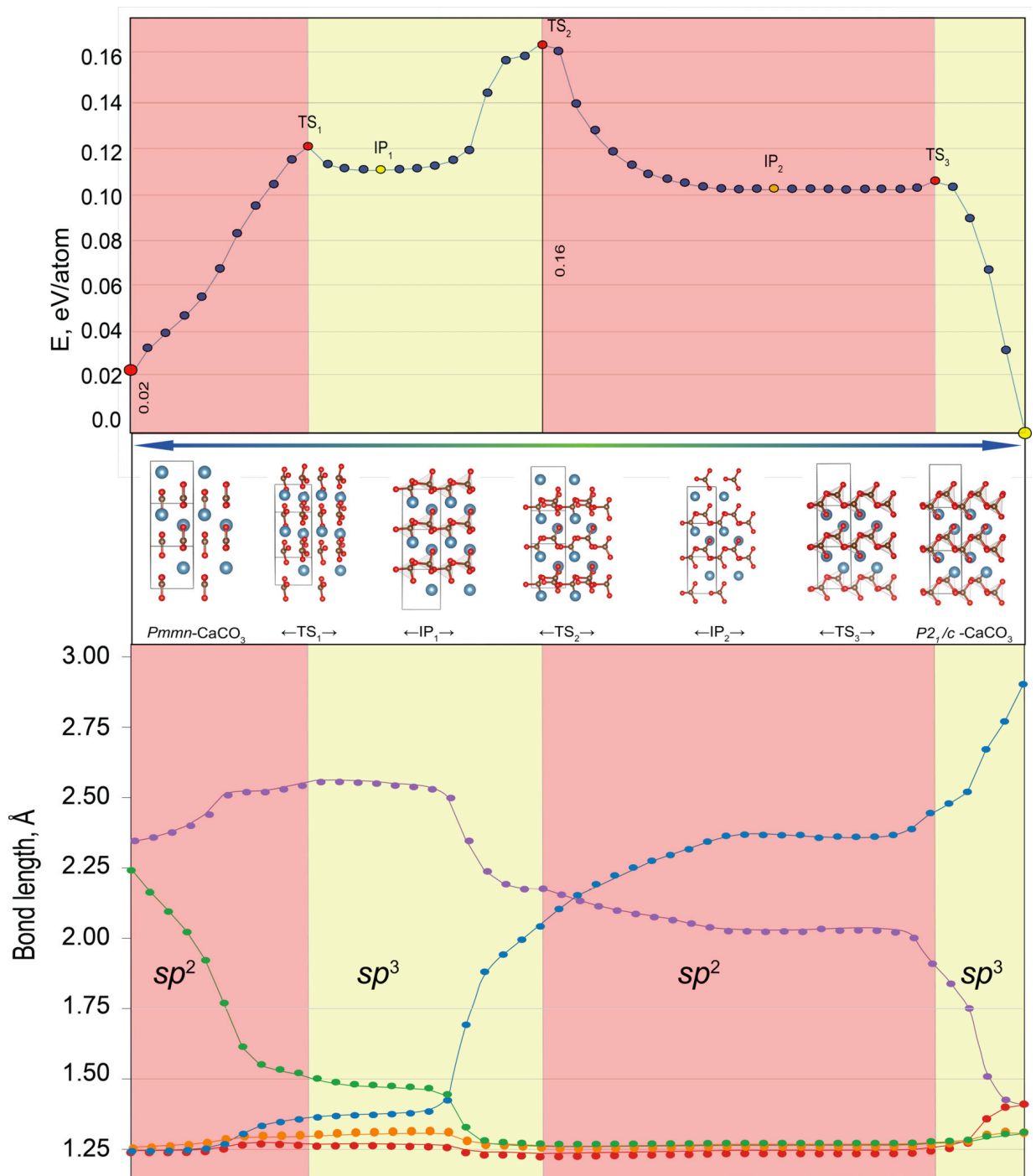
Figure 5.8. Mechanism of the *Pmmn* (postaragonite) → $P2_1/c$ transition of CaCO₃ at 100 GPa. Structures of initial postaragonite phase; transition states TS₁, TS₂, and TS₃; intermediate phases IP₁ and IP₂; and final $P2_1/c$ of CaCO₃ are shown (for clarity, we highlighted CO₄ tetrahedra). The evolution of the five shortest C-O distances is shown across the proposed transition path.

5.3 Mechanism of the phase transition in tungsten monoborides

Transition metal borides are important materials for many industrial applications and the most common are boron-rich phases, which are superhard [268–274]. However, not only the boron-rich phases could have potential interest from fundamental points of view. It is known experimentally that there are two tungsten monoborides with $I4_1/amd$ and $Cmcm$ space groups, respectively [275,276]. Initially, tungsten monoboride was reported to crystallize in a tetragonal α-MoB-type structure in the space group $I4_1/amd$ [275] and was later named α-WB. It was found from the X-ray patterns of hot-pressed W–B alloys with W:B = 1:1 composition after annealing treatments at temperatures between 1473 and 1673 K that it consists of the low-temperature α-WB and the high-temperature orthorhombic CrB-type structure, recognized as β-WB ($Cmcm$ space group). Its detailed crystallographic characteristics were measured and its isostructurality with the CrB phase was confirmed experimentally [277]. These tungsten monoborides have a difference in the enthalpy formation of about 13 meV/atom [273,278].
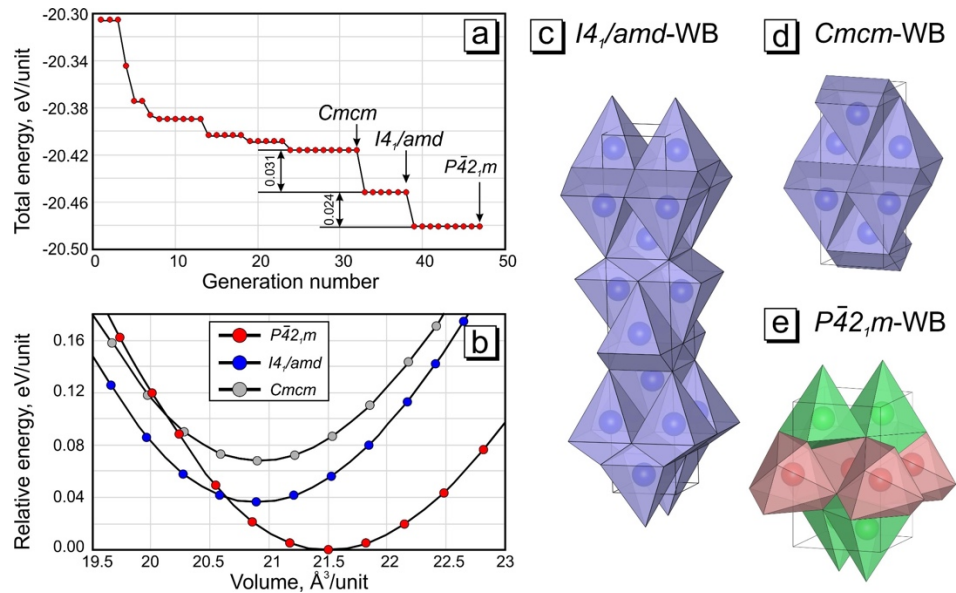
Figure 5.9. a) Total energy as a function of generation number as a result of the fixed-composition evolutionary search for WB phases; b) total energy per stoichiometry unit as a function of the volume for considered WB phases; c-e) crystal structures of $I4_1/amd$, $Cmcm$ and $P\bar{4}2_1m$ phases. Boron atoms are located in the vertexes of polyhedra. Green and red colors of W atoms demonstrate symmetrically nonequivalent atoms. Crystal structures of WB phases were generated using VESTA [215] (reprinted from Ref [279]).

A recent computational study made by Kvashnin et al. [274] indicates the potential existence of a new low-temperature phase of WB with $P\bar{4}2_1m$ space group, stable in the temperature range from 0 to 300 K at ambient pressure [274]. $P\bar{4}2_1m$-WB was found to be thermodynamically more stable than α-WB with the enthalpy difference of 12 meV/atom [274]. Thus there is an issue why such low-enthalpy phase has not been found experimentally, yet. In recent study [279], we predicted all three thermodynamically stable tungsten monoborides using the fixed-composition USPEX evolutionary

algorithm. The dependence of the total energy of various tungsten monoboride phases on the number of the generation during the evolutionary search is shown in Figure 5.9a. The calculated dependences of the total energy on the volume of three lowest-energy tungsten monoborides shown in Figure 5.9b. Calculated curves make it possible to obtain information about the pressure required for the $P\bar{4}2_1m \rightarrow I4_1/amd$ phase transition, which is equal to 12.9 GPa; this value is in good agreement with 11.8 GPa from Ref [280]. The volumes of the unit cells of β-WB and α-WB are almost the same, but the energy of the equilibrium state of β-WB is higher than that for α-WB (see Figure 5.9b). Physically, this means that the $I4_1/amd$ phase cannot undergo a phase transition to the $Cmcm$-WB phase under the action of a finite external pressure. The only way for the phase transition from the α phase to the β phase is to increase the temperature. These conditions are used in experimental synthesis of these materials [275,276].

The crystal structures of the studied tungsten monoborides are shown in Figure 5.9c-e. Boron atoms are located at the vertices of polygons and are not shown explicitly. Blue polyhedra correspond to the boron atomic environment of a tungsten atom. The α- and β-WB phases differ in mutual arrangement of layers in their crystal structures. The α-WB structure consists of WB layers with the AB stacking. Each layer is turned with respect to the neighboring layer by 90°, whereas the β-WB phase has the AA' stacking, where each layer is shifted with respect to the neighboring layer by half the lattice parameter a. A W atom in both phases is coordinated with six boron atoms and seven tungsten atoms; i.e., it has a coordination number of 13. The new $P\bar{4}2_1m$ -WB phase can also be represented as a layered structure, but each layer is obtained by the fusion of A and B layers of the α-WB structure. Each layer consists of two tungsten atoms at the Wyckoff positions 2b (0.000, 0.000, 0.500) and 4e (0.754, 0.254, 0.131). The tungsten atom at the 2b position is coordinated with six boron atoms and ten tungsten atoms, whereas the second tungsten atom is coordinated with eight boron atoms and eight tungsten atoms.
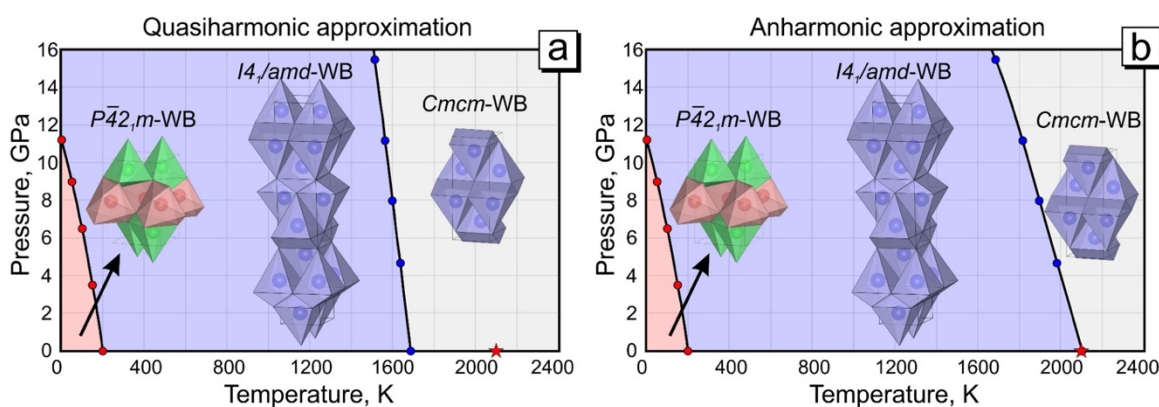
Figure 5.10. The pressure-temperature phase diagrams of tungsten monoborides calculated using both a) quasiharmonic and b) anharmonic approximations (reprinted from Ref [279]).

As has been shown before [274], $P\bar{4}2_1m$-WB is stable up to 250 K, after which the α-WB becomes more stable until the 2100 K, where the β-WB possesses higher stability. The study of possible phase transition from the only temperature contribution to the energy is not complete, herein, the pressure-temperature phase diagram has been constructed for the whole stability field in our study. The Gibbs free energy was calculated, including zero-point and vibrational energy contributions in both quasiharmonic and anharmonic approximations (for details, please refer to Ref [279]) and the phase diagrams are illustrated in Figure 5.10. As one can see from Figure 5.10 the phase boundary between $P\bar{4}2_1m$ and $I4_1/amd$ phases starts from 11.8 GPa (0 K) and decreases to zero as temperature increases to 200 K according to both quasiharmonic (QHA) and anharmonic (AHA) calculations. The anharmonic contribution does not influence significantly the phase boundary because of the low temperature.

At higher temperatures ~1600 K, the α phase undergoes a phase transition to β phase according to QHA (see Figure 5.10a). However, AHA gives much higher temperature of phase transition at zero pressure of ~2100 K, which perfectly agrees with the experimental value of the transition temperature of 2110 K [281]. It is also can be found that the α phase can be transformed into β phase at lower temperatures ~1800 K by applying pressure of 15 GPa (see Figure 5.10b). It can also be noted that β-WB cannot be synthesized at low temperatures by using only pressure. Thus, the newly predicted $P\bar{4}2_1m$-WB phase can be obtained only at very high temperature.

Along with the analysis of the phase diagram, the transition pathways during the $P\bar{4}2_1m \rightarrow I4_1/amd$ phase transition has been investigated and details of this part are provided below.

5.3.1 Calculation details

The structural phase transition from $P\bar{4}2_1m$ to $I4_1/amd$-WB (α phase) was performed at 0 GPa. As has been mentioned in **Geometry optimization** section of **Methodology** chapter, first of all, both structures ($P\bar{4}2_1m$ and $I4_1/amd$) have to be well optimized. The plane–wave energy cutoff of 600 eV was used, ensuring excellent convergence of total energies, forces and stresses. Among all possible mappings for the transition generated by geometrical mapping approach (see **Geometrical mapping** paragraph), we chose top 10 results. Because of mapping algorithm is not commutative, there have been generated two sets of mappings ($P\bar{4}2_1m$-WB $\rightarrow I4_1/amd$-WB and $I4_1/amd$-WB $\rightarrow P\bar{4}2_1m$-WB). From the obtained mappings, the initial pathways were generated using linear interpolation approach as described in **Initial path generation** section. Each of all generated initial pathways was subsequently refined by VCNEB method as presented in **Pathway optimization** section. VCNEB calculations started with 21 intermediate images (structures), and this number was automatically increased whenever the path became longer. Spring constants varied from 7 to 10

eV/Å^2. The halting criterion for the calculation was set as RMS (Root Mean Square forces) on images that are less than 0.01 eV/Å.

5.3.2 Results

At a pressure of 0 GPa, the $P\bar{4}2_1m$ -WB is more stable by 12 meV/atom than $I4_1/amd$-WB. The total number of atoms in the simulated unit cell was set to 48 (considered cells are $W_{24}B_{24}$) which is the least common multiple number of atoms in the primitive cells of both phases (12 and 16 for $P\bar{4}2_1m$ and $I4_1/amd$, respectively). This leads to a simulation of the phase transition in large dimensionality of configurational space. Because of these two reasons, the transformation mechanism appeared to be quite complex. The considered unitcells are presented in Figure 5.11b-d.
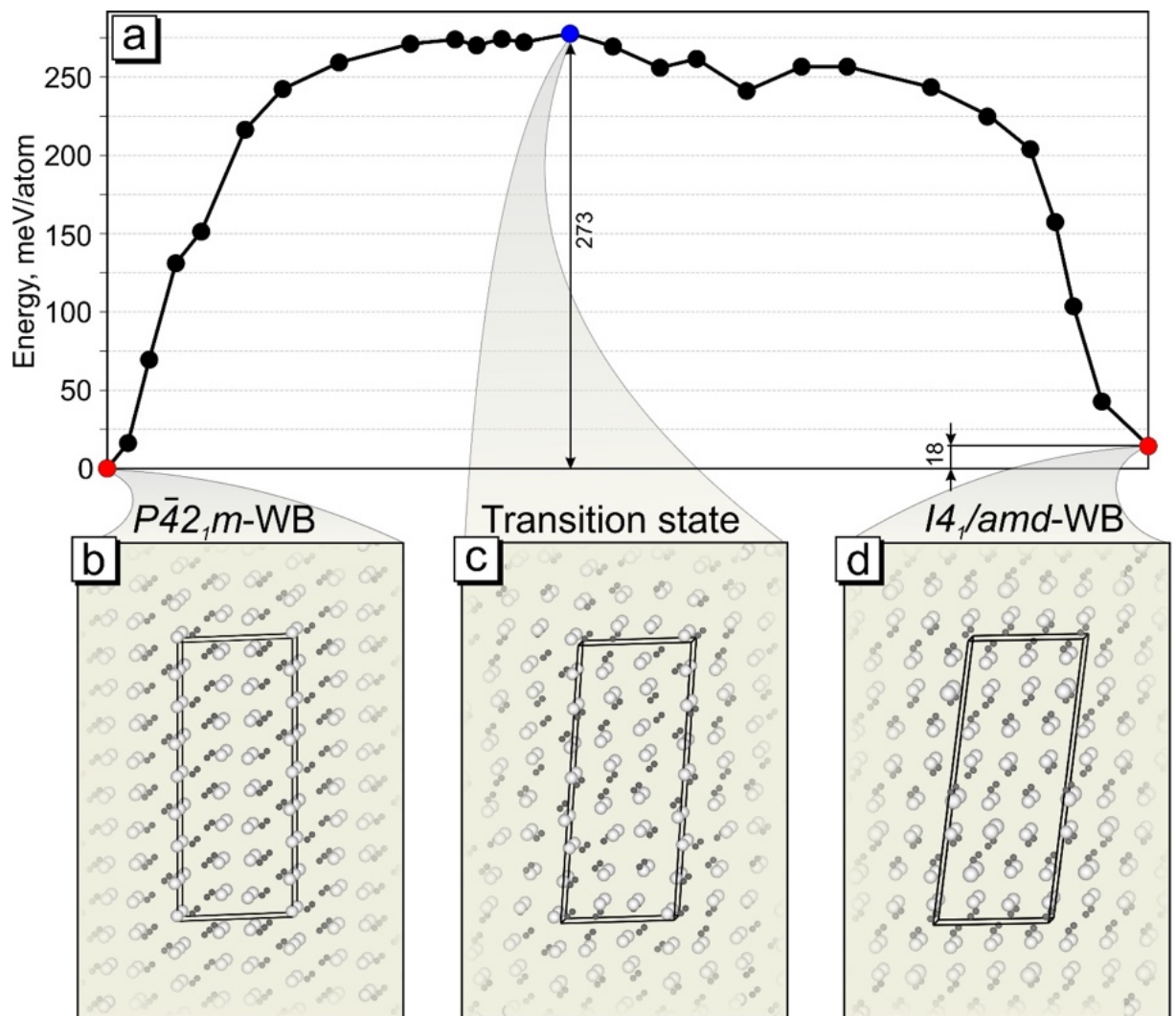
Figure 5.11. a) The $P\bar{4}2_1m \rightarrow I4_1/amd$ phase transition pathway for studied tungsten monoborides at 0 K and 0 GPa. Crystal structures of the b) initial $P\bar{4}2_1m$-WB, c) transition state and d) final $I4_1/amd$-WB. Tungsten atoms are white; boron atoms are dark grey (reprinted from Ref [279]).

Canonical approaches, which usually consider only the movement of atoms in the crystal structure, are not the best way to describe such complex transitions. To describe it from the physical point of view, the change in crystal structure connectivity was considered [164]. This approach shows which interatomic contacts are broken and which new contacts are created during the transition. Here, in the $P\bar{4}2_1m \rightarrow I4_1/amd$ phase transformation, boron atoms are moving more chaotically than tungsten atoms (tungsten is much heavier than boron), and thus only the evolution of tungsten sublattice was studied. Each tungsten atom in the W-sublattice of $I4_1/amd$-WB is 10-coordinated, while $P\bar{4}2_1m$-WB phase has 8 and 10-coordinated tungsten atoms. During the transition, the coordination number of tungsten varies in the range between 8 and 12.

For each tungsten atom, we chose specific surroundings representing W-W bonds that will be formed and bonds that will be broken during the transition. According to this criterion, all tungsten atoms can be divided into four groups corresponding to different types of bond evolutions shown in Table 5.1. The first number shows the coordination number (CN) of the selected tungsten atom at the starting point and the second shows the number of additional interatomic contacts that will be created during the transition. For example, the first line shows that in the $P\bar{4}2_1m$-WB selected tungsten atom has 8 bonds (coordination number is 8) in the shell in the starting point, 4 additional interatomic contacts will be created and then 2 interatomic contacts will be broken during the transition to $I4_1/amd$-WB. Thus, this tungsten atom will have 10 W-W bonds in its coordination sphere. Such description helps us to represent the moving of tungsten atoms in terms of changing their coordination number, i.e. creating and breaking interatomic contacts (see Figure 5.12).

Table 5.1. Four types of tungsten atoms in the W-sublattice of both phases according to bond evolution

$P\bar{4}2_1m$-WB	$I4_1/amd$-WB
8+4	10+2
8+3	10+1
10+2	10+2
10+1	10+1
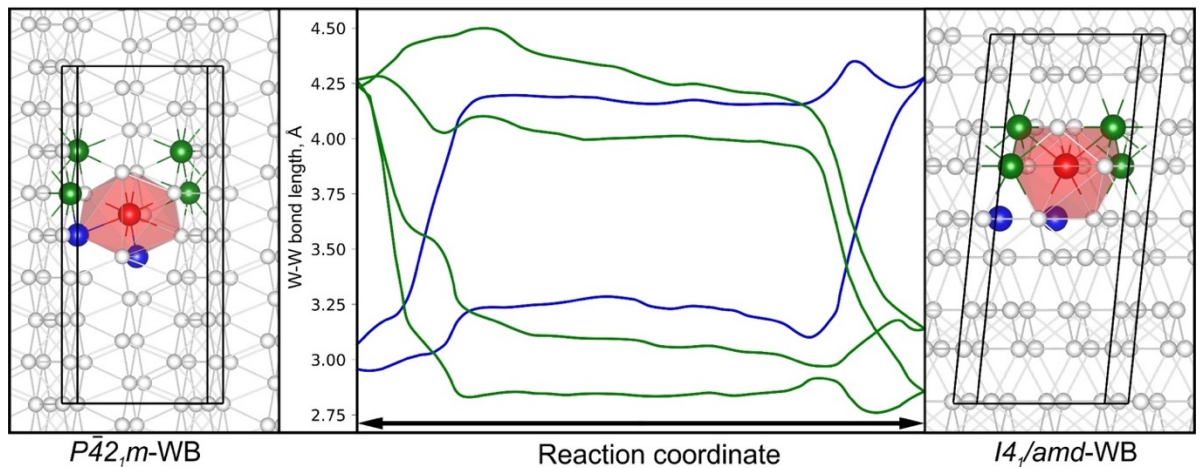
Figure 5.12. Changing in the coordination of specific tungsten atom (red color). Tungsten atoms that have no interatomic contact in the $P\bar{4}2_1m$-WB is highlighted by green color, blue color is for atoms that have interatomic contact in $P\bar{4}2_1m$-WB, but it will be cut during the transition to $I4_1/amd$-WB.

Transition states define the crossover between different topologies, i.e., the point at which chemical bonds are formed or broken. In Figure 5.11a, one can see the energy profile of the lowest-energy phase transition mechanism with a large number of local minima, which shows the logic of nucleation-and-growth process in real solid-solid phase transformation. These intermediate minima are so shallow that they are unlikely to be quenched in the experiment: these minima are not strongly kinetically protected and will rapidly decay into $P\bar{4}2_1m$-WB or $I4_1/amd$-WB, respectively. The transition state with the highest energy has symmetry *P1* and its energy is 255 meV/atom higher than that of $P\bar{4}2_1m$-WB and 273 meV/atom higher than for $I4_1/amd$-WB (α-WB).

5.4 Mechanism of the phase transition in Al_2SiO_5 phases

Andalusite, kyanite and sillimanite are three minerals that are polymorphic modifications of Al_2SiO_5 [282,283]. Important for Earth's sciences, they also have wide practical usage as ceramic and refractory materials [284] and they are used to produce lightweight aluminum-silicon alloys to fabricate metallic fiber, which is used in supersonic aircraft and spaceships, etc. [285–288]. A closely related material, mullite, a component of porcelain, has recently become a promising candidate for structural and functional ceramics due to its low thermal expansion, low thermal capacity, and excellent creep resistance along with high-temperature strength and stability under severe chemical environments [289,290].

All three structures have some common features: all Si atoms are tetrahedrally coordinated and half of all Al atoms are in the octahedral coordination and form chains of edge-sharing AlO_6 octahedra [291,292]. The other half of Al atoms are in the tetrahedral coordination in sillimanite, 5-fold coordination in andalusite, and in the octahedral coordination in kyanite. Kyanite crystallizes in the triclinic system with space group $P\bar{1}$ [293], while sillimanite and andalusite crystallize in the orthorhombic structures with space groups *Pnnm* and *Pbnm*, respectively [293,294]. All three polymorphs of Al_2SiO_5 are found commonly in metamorphic rocks and are geologically important markers since they provide information about pressure and temperature at their time of formation and the type of metamorphism [295–297].

Andalusite is formed as a low-pressure and low-temperature phase, while kyanite is formed at high pressure and low temperature, and sillimanite is formed at medium or low pressure and high temperature [295,298]. The entropy and Gibbs free energy of the three minerals are very similar [295,299].

In nature, often two or three polymorphs of Al_2SiO_5 are found coexisting in the same rock. There are numerous examples with each of two-polymorph assemblages, i.e. andalusite + kyanite, kyanite + sillimanite and andalusite + sillimanite [300–302] and in many cases all three Al_2SiO_5 polymorphs coexist in a rock [296,303–318]. Such coexistence indicates conditions of formation at a rock, corresponding to two- or three-phase equilibrium. Coexistence at normal conditions is due to high barriers of transitions, leading to metastable persistence of phases.

Here, we have studied in detail the mechanisms of structural transitions between all three phases of Al_2SiO_5 – kyanite-andalusite, andalusite-sillimanite and kyanite-sillimanite at the pressures of 0 and 10 GPa. The obtained results have provided insights into the nature of structural changes of Al_2SiO_5 polymorphs, their coexistence with each other and their transformation pathways.

5.4.1 Calculation details

The lattice parameters and atomic positions of Al_2SiO_5 polymorphs used in our calculations were taken from experimental studies of Ralph et al. [319] for andalusite and from Yang et al. [293,294] for kyanite and sillimanite. Then, these structures were relaxed. Structure relaxations and total energy

calculations were performed as presented in **Geometry optimization** paragraph. The plane–wave energy cutoff of 600 eV was used, ensuring excellent convergence of total energies, forces and stresses. Crystal structures were relaxed until the maximum net force on atoms became less than 0.01 eV/Å. The Monkhorst–Pack scheme [213] was used to sample the Brillouin zone, using 4×3×3 for all three Al_2SiO_5 phases. For each of andalusite-kyanite, kyanite-sillimanite and andalusite-sillimanite transitions, we used the geometrical mapping approach (see **Geometrical mapping** paragraph) and among all possible mappings, we chose the top 10 results. Because of the noncommutativity of the mapping algorithm, it was used to generate two sets of pathways - forth and back (structure A → structure B and structure B → structure A).

From the obtained mappings, the initial pathways were generated using linear interpolation approach as described in **Initial path generation** section. To find the optimal solution, we generated a large number of initial paths for each of andalusite-kyanite, kyanite-sillimanite and andalusite-sillimanite transitions. Each of all generated initial pathways was subsequently refined by VCNEB method as presented in **Pathway optimization** section. The VCNEB calculation began with an initial path transition consisting of 20 intermediate structures ("images"). All these cells have 32 atoms in the unit cell, and in all trajectories we considered all intermediate structures also had 32 atoms/cell. The spring constants for the VCNEB method were varied from 3 to 6 eV/Å^2. The halting criterion for the calculation was set as RMS (Root Mean Square forces) on images that are less than 0.003 eV/Å. Crystal structures of predicted phases and were generated using VESTA software [215].

5.4.2 Results

Crystal structures of the Al_2SiO_5 phases are shown in Figure 5.13a-c. Gray, orange and green polyhedra shown in Figure 5.13e-f correspond to 6-,5- and 4-coordinate Al atoms. Blue polyhedra in Figure 5.13g corresponds to silicon atoms, which are 4-fold coordinated.
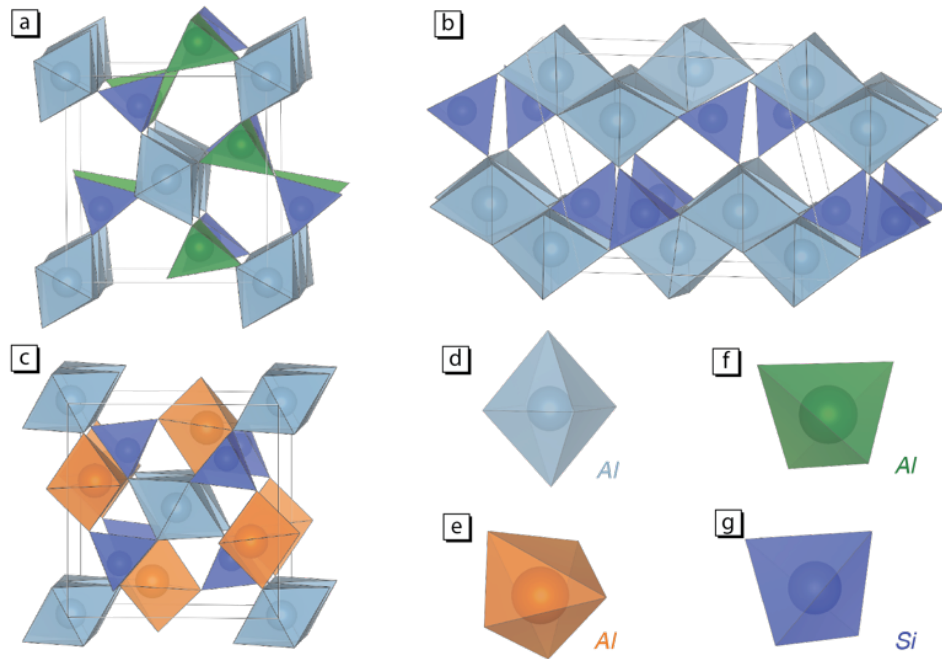
Figure 5.13. Crystal structures of a) sillimanite, b) kyanite and c) andalusite phases of Al_2SiO_5. Oxygen atoms are located in the vertices of polyhedra; polyhedra of Al atoms in different structures and correspond to the d) 6-, e) 5- and f) 4-coordinate atoms; g) tetrahedral coordination of Si atom.

First, we relaxed structures of all three Al_2SiO_5 phases at the pressures of 0 and 10 GPa. The lowest-enthalpy phase is andalusite at 0 GPa and kyanite at 10 GPa, which is in agreement with experiments and previous calculations [320]. As one can see in Figure 5.14, all three phases are energetically close to each other. At 0 GPa, sillimanite is 10 meV/atom higher in energy than andalusite, and kyanite is 12 meV/atom above sillimanite. At 10 GPa, sillimanite is 60 meV/atom higher in enthalpy than kyanite and andalusite is 8 meV/atom above sillimanite.
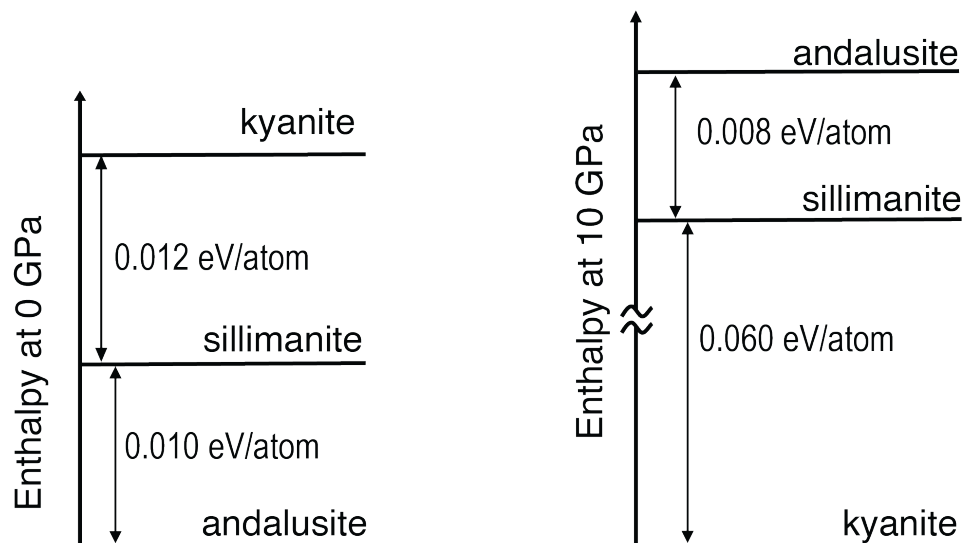
Figure 5.14. Enthalpy differences between Al_2SiO_5 phases at 0 GPa and 10 GPa.

First, let us consider the transition from sillimanite to andalusite at pressures of 0 and 10 GPa. Both structures have relatively similar orthorhombic cell parameters listed in Table 5.2. Given the similarity of unit cells and even of crystal structures, one might think that it is trivial to construct the optimal phase transition pathway and that it should be within the orthorhombic cell. We did this both at 0 GPa and 10 GPa, at each pressure constructing the initial pathways by using smooth variation of orthorhombic cell parameters and choosing such mapping of atomic coordinates that minimizes the total distance traveled by all the atoms. Then, we optimized these paths by the VCNEB method. The resulting pathways are presented in Figures 5.15 and 5.16. As one can see, the energy barrier equals 0.389 eV/atom at 0 GPa and 0.353 eV/atom at 10 GPa. It is instructive that these are not the lowest-barrier paths. Considering non-trivial cell mappings, we found lower-barrier paths.

Table 5.2. Lattice parameters for orthorhombic structures of andalusite and sillimanite at the pressure of 0 and 10 GPa: theoretical results and experimental data [293,319]

	VASP, 0GPa	Experiment, 0 GPa	VASP, 10 GPa
andalusite	$a = 5.610$ Å	$a = 5.557$ Å	$a = 5.534$ Å
	$b = 7.868$ Å	$b = 7.798$ Å	$b = 7.647$ Å
	$c = 7.973$ Å	$c = 7.903$ Å	$c = 7.821$ Å
sillimanite	$a = 5.816$ Å	$a = 5.777$ Å	$a = 5.754$ Å
	$b = 7.568$ Å	$b = 7.488$ Å	$b = 7.415$ Å
	$c = 7.772$ Å	$c = 7.681$ Å	$c = 7.559$ Å
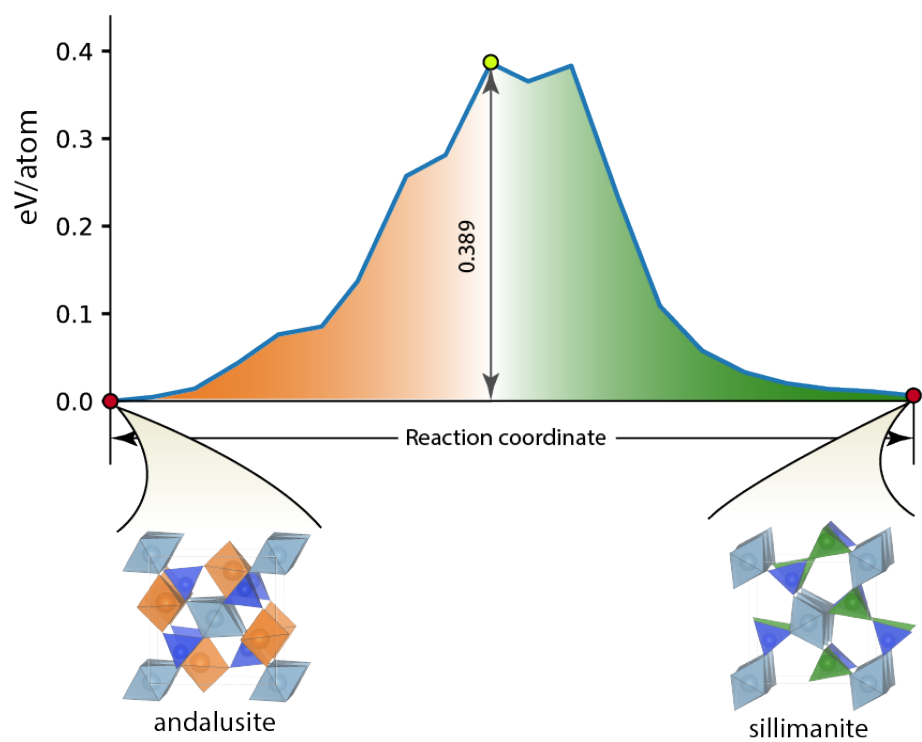
Figure 5.15. Enthalpy profile of andalusite-sillimanite transition at 0 GPa generated with fixed-cell mapping.
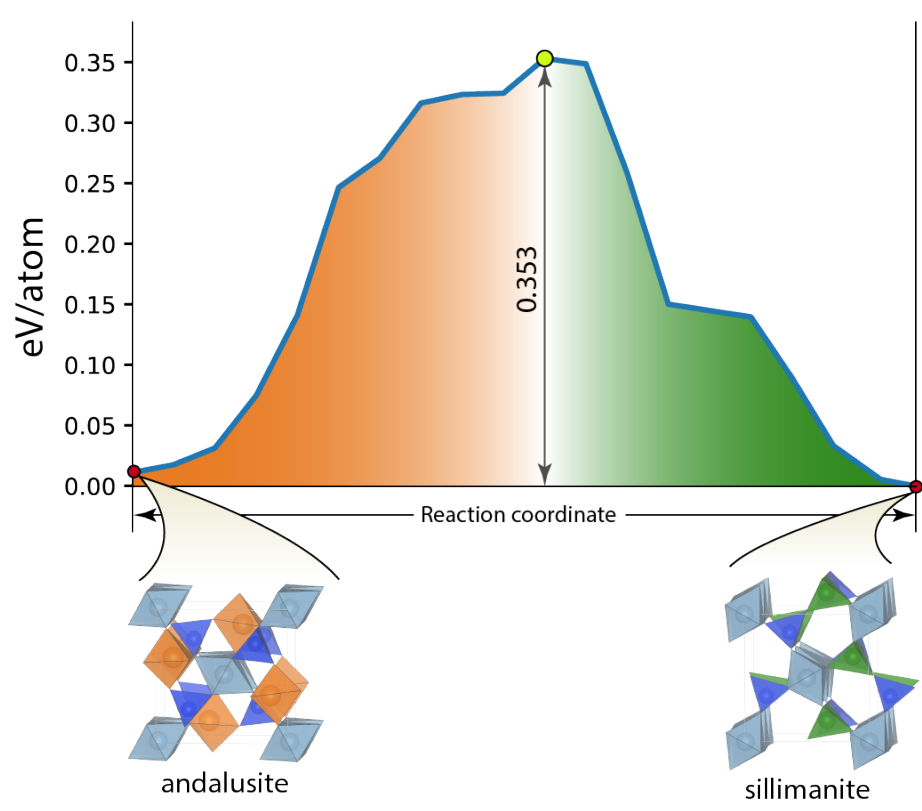
Figure 5.16. Enthalpy profile of andalusite-sillimanite transition at 10 GPa generated with fixed-cell mapping.

Thus, to describe phase transitions we generated six sets of initial pathways for the optimized structures at each pressure (kyanite → sillimanite, sillimanite → kyanite, kyanite → andalusite, andalusite → kyanite, andalusite → sillimanite and sillimanite → andalusite). The structure mapping for the initial pathway generation considers the mapping of cell parameters and atomic positions. Each set consists of 10 initial pathways. The lowest-barrier transition profiles for each transformation at 0 and 10 GPa are shown in Figures 5.17 and 5.18, respectively. For all transitions the symmetry of intermediate states is *P1*. These are all reconstructive phase transitions; energy barriers for each transition at both pressures are very high and the schemes of transitions with barrier values are presented in Figure 5.19. Such high barriers imply that these transitions are kinetically feasible only at high temperatures (the lowest energy barrier of 0.255 eV/atoms).
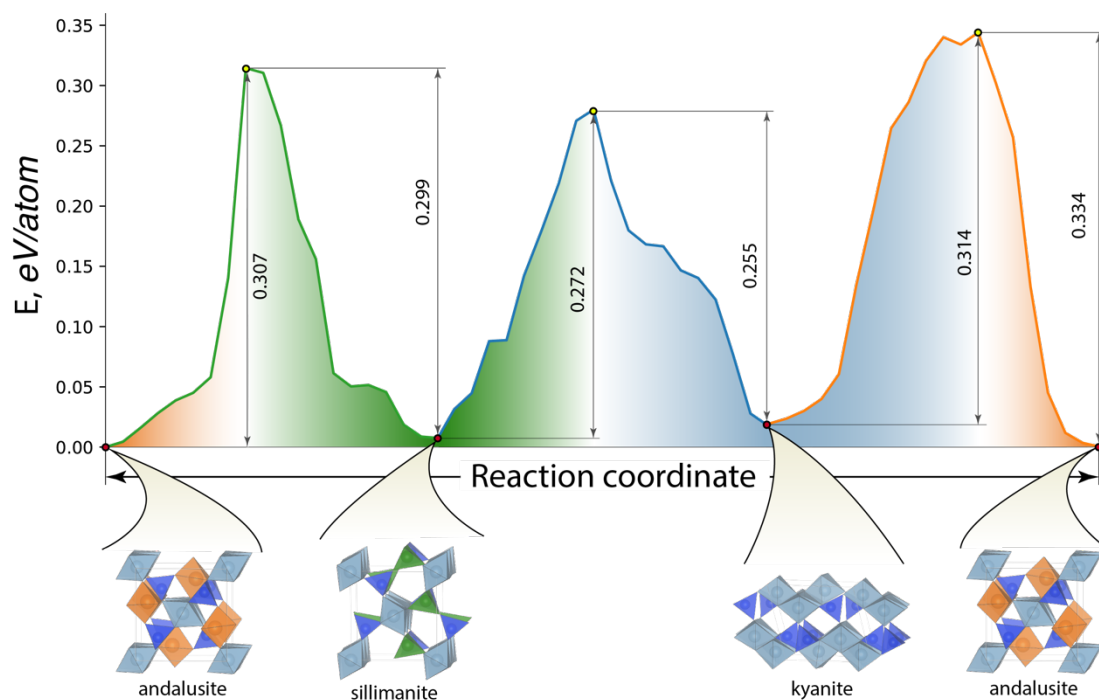
Figure 5.17. Enthalpy profile of kyanite-sillimanite, sillimanite-andalusite and andalusite – kyanite transitions at 0 GPa.
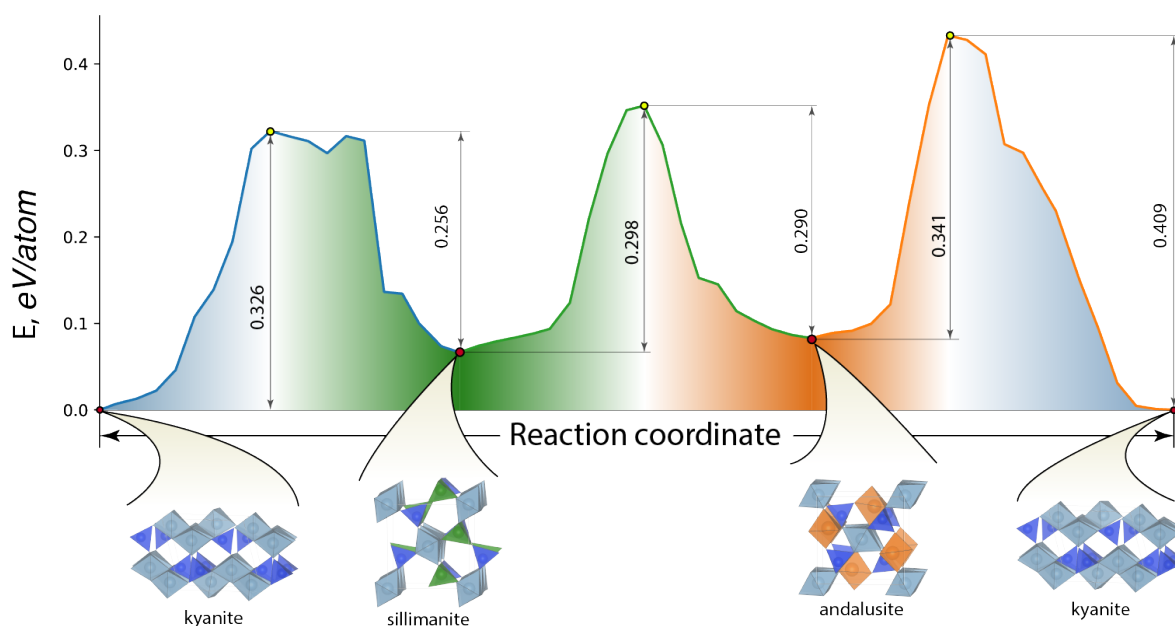
Figure 5.18. Enthalpy profile of kyanite-sillimanite, sillimanite-andalusite and andalusite – kyanite transitions at 10 GPa.
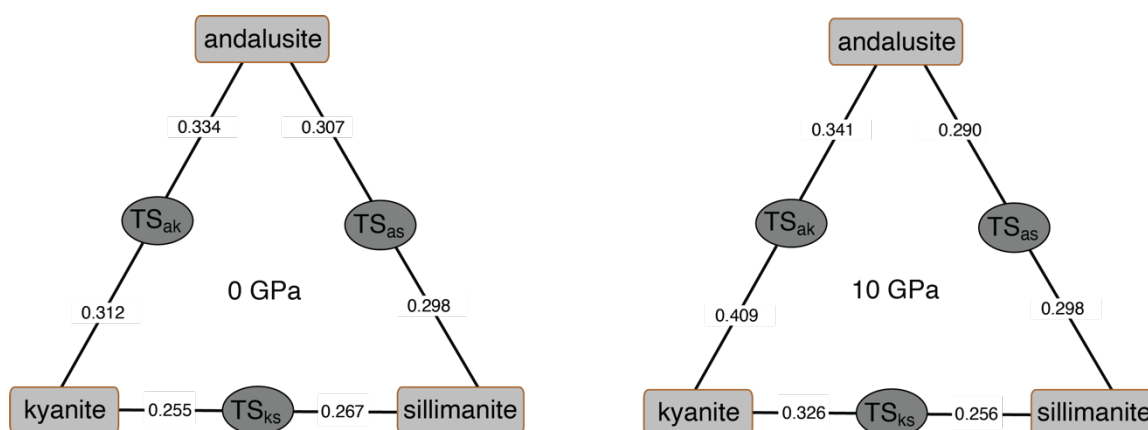
Figure 5.19. Calculated energy barriers for transitions at 0 and 10 GPa

The canonical approach, which usually involves only the movement of atoms in the crystal structure, is well-known and intuitive, but it is not the best description of such complex transitions.

Further insight can be obtained by looking at changes of a bond network in crystal structures. For the determination of interatomic contacts, we use a Voronoi–Dirichlet partition of crystal space. Since all intermediate structures along the transition path are distorted, the coordination of the polyhedra approach can be supplemented by the "effective" coordination number (ECoN) approach [321,322], which describe the surrounding of the atom with a weighting scheme, where the atoms are not counted as full atoms but as fractional atoms with numbers between 0 and 1. These two approaches allow us to understand how many interatomic contacts are broken and which new ones are formed during the transition.

We find that SiO$_4$ tetrahedra are present during all transitions and there are no changes in the coordination number of silicon. Indeed, Si-O bonds are the strongest here and, naturally, they are perturbed the least. The change of coordination of Al atoms is much more complex and informative – it provides more insights into the transition nature. Figures 5.20 and 5.21 show the change of average connectivity of Al atoms during all transitions at 0 GPa and 10 GPa, respectively. In Figures 5.22 and 5.23 we present the change of average ECoN of Al atoms during all transitions at 0 GPa and 10 GPa, respectively. Note that the averaging involves all Al atoms (including those which are 6-coordinate in three polymorphs – during transitions their coordination number also change). Transition states have the lowest average coordination number (CN) of Al atoms along the pathway, which is easy to understand – a large number of all Al-O bonds have been broken, while the new ones have not yet been formed.
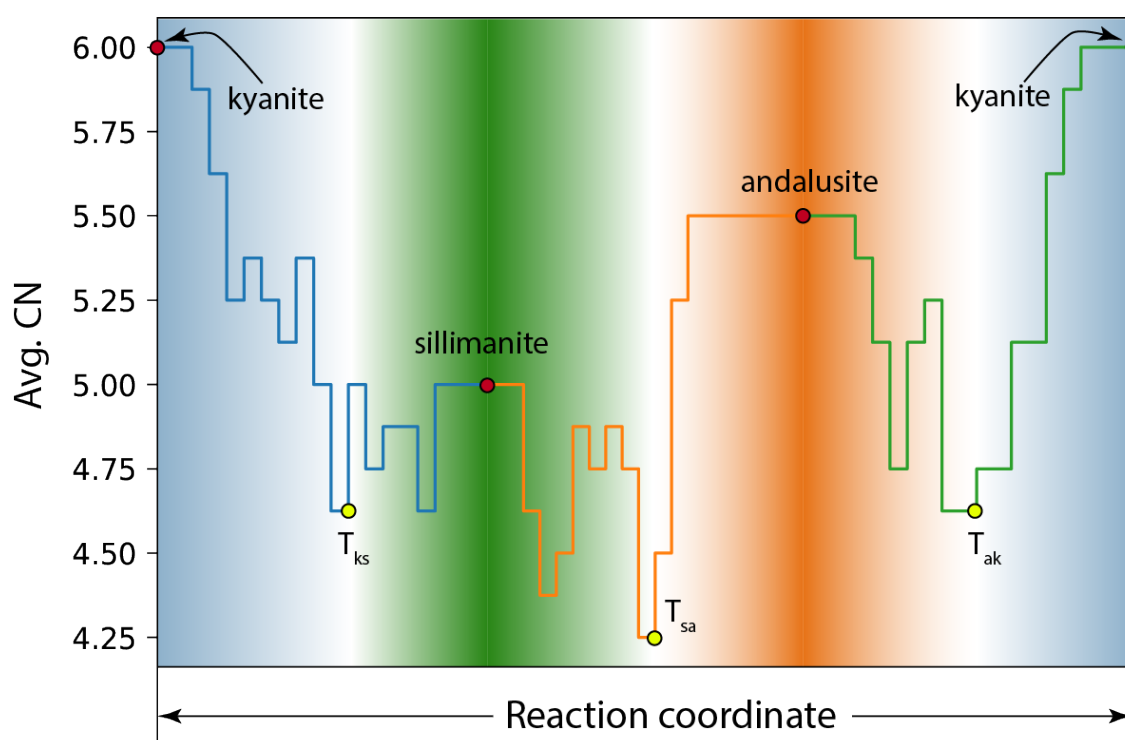
Figure 5.20. The average coordination number of Al atoms for all three transitions at 0 GPa
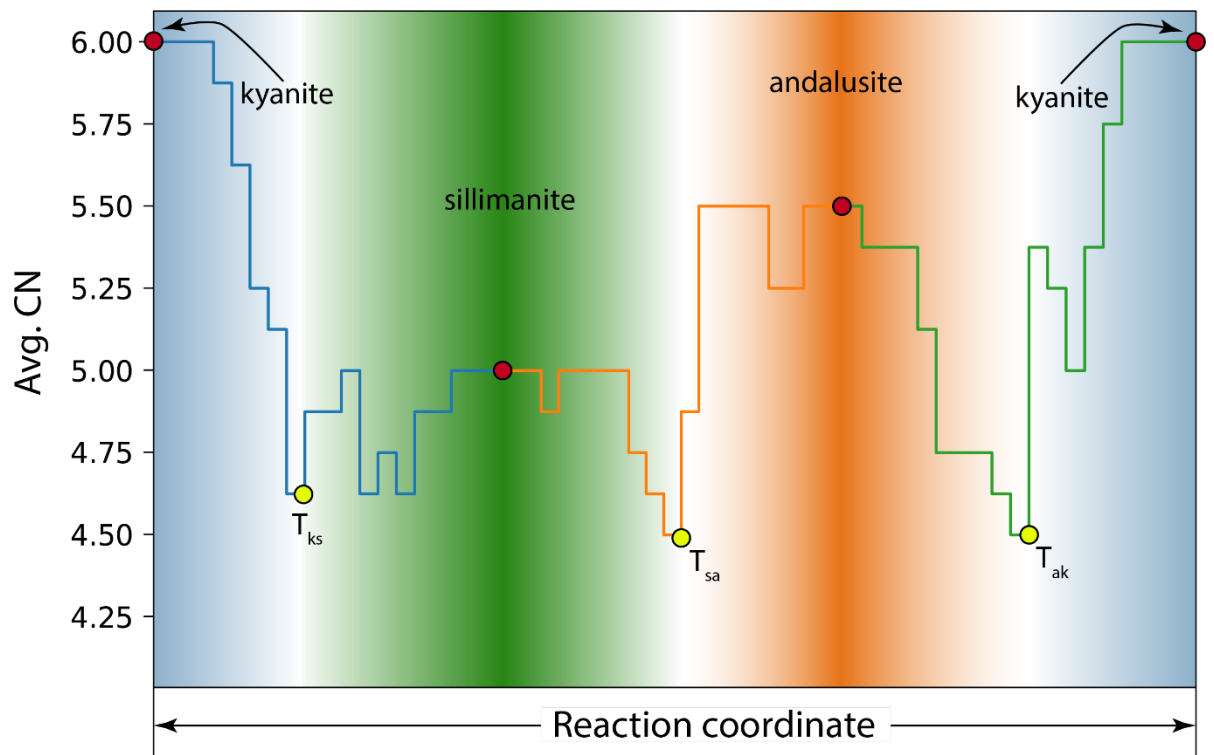
Figure 5.21. The average coordination number of Al atoms for all three transitions at 10 GPa
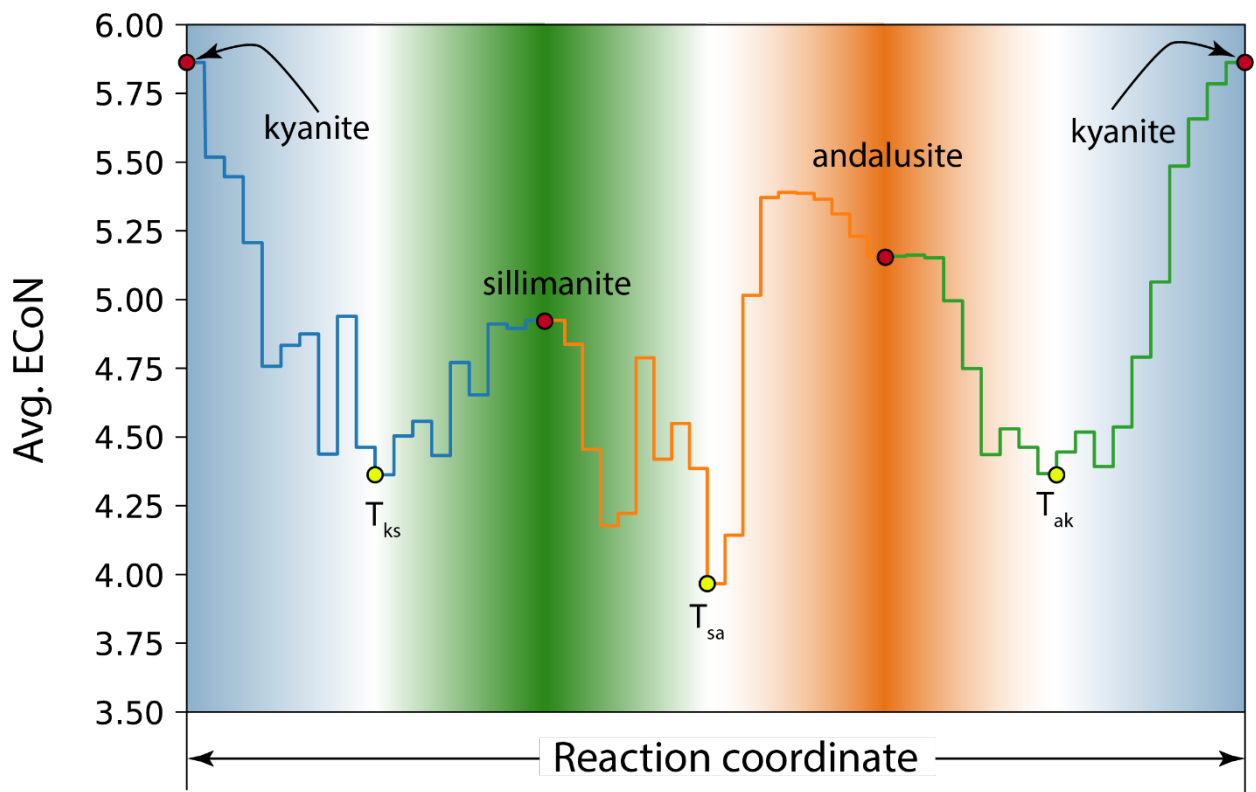
Figure 5.22. Average effective coordination number (ECoN) of Al atoms for all three transitions at 0 GPa
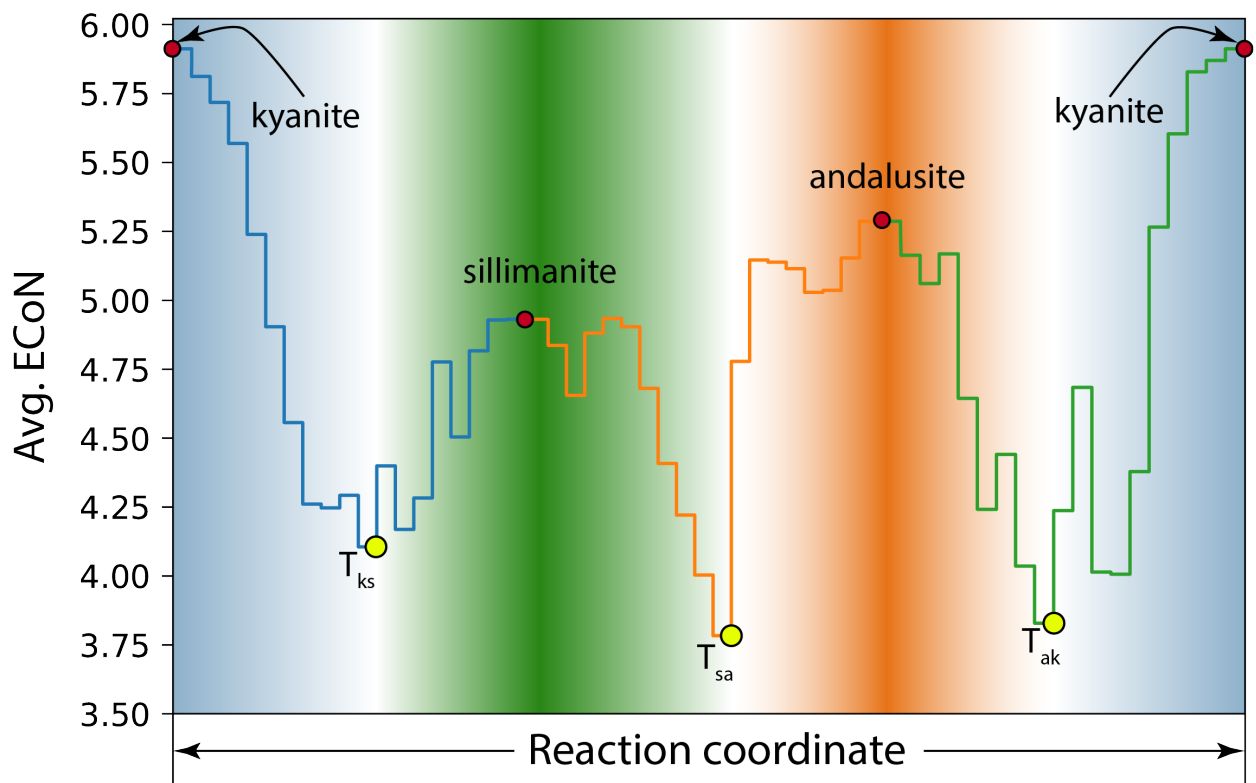
Figure 5.23. Average effective coordination number (ECoN) of Al atoms for all three transitions at 10 GPa

The combination of topological, geometrical and energetic descriptions is a tool, which allows us to compare transitions at 0 and 10 GPa and state that these transitions differ significantly. For andalusite-sillimanite transition at 0 GPa, the changes of coordination are more complex than at 10 GPa. In general, at high pressure, the drops of average coordination numbers are smaller.

6 CONCLUSIONS AND FUTURE PERSPECTIVES

This Thesis proposes a number of improvements to the canonical workflow to investigate solid-solid phase transitions by two-ended methods. These improvements help investigate free energy landscapes of solids and locate MEP for more complex phase transitions. The workflow contains the following major steps:

1. Optimization of the chosen end structures.

2. Build the atom-to-atom mapping between initial and final structures.

3. Generate an initial pathway(s) based on the generated mapping(s).

4. Refine generated initial pathways by a two-ended method and the selection of MEP.

Step 2 can be done in two variants based on two different ideas. The first one is based on the purely geometrical compliance of two structures, i.e., cell parameters and coordinates of atoms. The second one is based on the relation of periodic graphs of interatomic contacts (topological nets) and the atom-to-atom mapping comes from the compatibility of nets. The topological approach is more advanced than the geometric one since it provides mapping(s), which leads to transition with the optimal number of broken and created interatomic contacts. In other words, the topological approach considers the physical and chemical aspects of both structures and their change during the transition.

The geometrical approach allows for the calculations of the transition with any atoms in a cell, but the complexity of such approach grows exponentially with the number of atoms and it can be called straightforward. The algorithm brings both structures to the same number of atoms in the cell, which is the least common multiple of the number of atoms in primitive cells. Also, the geometrical consideration is not a time-efficient procedure since it creates a list of cells with maximized spatial (volumetric) overlap and for each pair of cells, it checks all possible variants of atomic matching for the generated cells. Thus, the phase transition investigation for structures where the least common multiple of the number of atoms in primitive cells is a huge number takes much time and can be done only with the help of high-performance computers (HPC). As a result, it provides a list of atom-to-atom mappings that yield a minimum of the sum of the Euclidian distances between the corresponding atoms in the two structures.

The topological approach allows for the consideration of solid-solid phase transitions in another way and has broadened the range of investigation. The central point of the algorithm is to build such a net relation graph that transforms one net into another by breaking and creating the least interatomic contacts and, at the same, by lowering the symmetries of both nets as small as possible. The net relation graph can be easily converted into the atom-to-atom mapping of both structures. However, such an approach has several important restrictions. For instance, the topological analysis can fail when the considered transition happens between structures with different low symmetries. Another case is the exponential explosion that can happen when atoms in both structures have high

coordination and a highly symmetrical environment. As a result, a vast number of combinations of interatomic contacts may be cut and create a new one. Nevertheless, such an approach shows its high efficiency and versatility of usage.

In general, the geometrical and topological approaches complement each other. The geometrical approach is straightforward and effective in the study transition pathways located in a narrow area of FES. In contrast, the topological approach provides more versatile pathways that cover a broader area of FES and can be helpful for global pathway optimization.

In this work, the geometrical approach made by Stevanovic et al. has been used for structure mapping in a brute-force way. In contrast, mapping crystal structures onto each other can be made by the newly developed topological approach, which is another application of the topological network model of solid-state transformations (TNMST). Both presented approaches have been integrated into the VCNEB method, which is a part of the USPEX code.

The presented workflow gave fruitful results in the investigation of solid-solid phase transitions. It has been used for the simulation of the transition from $Pnma$-CrN to newly predicted $P\bar{6}m2$-CrN, which is another hard phase of chromium nitride. Using the presented workflow, it has been shown that the mechanism of the sp^2-sp^3 crossover in $CaCO_3$ involves several intermediate phases with sp^2 and sp^3 bonding motifs and it helped to investigate the phase transition from $I4_1/amd$ to newly predicted $P\bar{4}2_1m$ phase in tungsten monoborides. Also, to investigate phase transitions between the Al_2SiO_5 polymorphs (andalusite, sillimanite and kyanite). Analysis of the evolution of the chemical bond network during transitions has shed light on the origin of high barriers responsible for the metastable coexistence of these phases in nature. The experimentalists can use the obtained results to understand how (external parameters) the newly predicted phases, like $P\bar{6}m2$-CrN or $P\bar{4}2_1m$-WB could be synthesized.

The presented approach helps to analyze the finite number of generated variants of transition pathways and select the MEP among them. Also, it is a good starting point for exploring the transition pathways in the solids, but the global search algorithm must be created. Since the complexity of such a search grows exponentially with the system size, it is the next big challenge for scientists.

References

1. Medhi, J. *Stochastic models in queueing theory*. (Elsevier, 2002).
2. Ptashne, M. & Gann, A. Genes and Signals. (2002).
3. Andersson, H. & Britton, T. *Stochastic epidemic models and their statistical analysis*. vol. 151 (Springer Science & Business Media, 2012).
4. Bartlett, M. S. Monte Carlo studies in ecology and epidemiology. in *Proceedings of the fourth Berkeley symposium on mathematical statistics and probability* vol. 4 39–55 (University of California Press London, UK, 1961).
5. Van Kampen, N. G. Stochastic processes in physics and chemistry, 3rd edn Amsterdam. *Netherlands Elsevier.[Google Sch.* (2007).
6. Marro, J. & Dickman, R. *Nonequilibrium phase transitions in lattice models*. (Cambridge University Press, 2005).
7. Mandelbrot, B. B. & Mandelbrot, B. B. *The fractal geometry of nature*. vol. 1 (WH freeman New York, 1982).
8. Niu, H., Piaggi, P. M., Invernizzi, M. & Parrinello, M. Molecular dynamics simulations of liquid silica crystallization. *Proc. Natl. Acad. Sci.* **115**, 5348–5352 (2018).
9. Jungblut, S. & Dellago, C. Pathways to self-organization: Crystallization via nucleation and growth. *Eur. Phys. J. E* **39**, 77 (2016).
10. Leoni, S. & Boulfelfel, S. E. Pathways of structural transformations in reconstructive phase transitions: insights from transition path sampling molecular dynamics. *Mod. Methods Cryst. Struct. Predict.* 181–221 (2010).
11. Chandler, D. Barrier crossings: classical theory of rare but important events. *Class. Quantum Dyn. Condens. Phase Simulations* 3–23 (1998) doi:10.1142/9789812839664_0001.
12. Chandra Shekar, N. V. & Rajan, K. G. Kinetics of pressure induced structural phase transitions—A review. *Bull. Mater. Sci.* **24**, 1–21 (2001).
13. Ehrenfest, P. Phase changes in the ordinary and extended sense classified according to the corresponding singularities of the thermodynamic potential. in *Proc Acad Sci Amsterdam* vol. 36 153–157 (1933).
14. Borrmann, P., Mülken, O. & Harting, J. Classification of Phase Transitions in Small Systems. *Phys. Rev. Lett.* **84**, 3511–3514 (2000).
15. Pippard, A. B. *Elements of classical thermodynamics: for advanced students of physics*. (Cambridge University Press, 1964).
16. Jaeger, G. The Ehrenfest Classification of Phase Transitions: Introduction and Evolution. *Arch. Hist. Exact Sci.* **53**, 51–81 (1998).
17. Roy, R. A SYNCRETIST CLASSIFICATION OF PHASE TRANSITIONS. in *Phase Transitions* 13–27 (Elsevier, 1973). doi:10.1016/B978-0-08-017955-1.50006-3.
18. Buerger, M. J. *Phase transformations in solids, ch. 6*. (New York: Wiley, 1951).
19. Bhattacharya, K., Conti, S., Zanzotto, G. & Zimmer, J. Crystal symmetry and the reversibility of martensitic transformations. *Nature* **428**, 55–59 (2004).
20. Kainuma, R. *et al.* Magnetic-field-induced shape recovery by reverse phase transformation. *Nature* **439**, 957–960 (2006).
21. Tanaka, Y. *et al.* Ferrous Polycrystalline Shape-Memory Alloy Showing Huge Superelasticity. *Science* **327**, 1488–1490 (2010).
22. Song, Y., Chen, X., Dabade, V., Shield, T. W. & James, R. D. Enhanced reversibility and unusual microstructure of a phase-transforming material. *Nature* **502**, 85–88 (2013).
23. Moya, X. *et al.* Giant and reversible extrinsic magnetocaloric effects in La0.7Ca0.3MnO3 films due to strain. *Nat. Mater.* **12**, 52–58 (2013).
24. Liu, J., Gottschall, T., Skokov, K. P., Moore, J. D. & Gutfleisch, O. Giant magnetocaloric effect driven by structural transitions. *Nat. Mater.* **11**, 620–626 (2012).
25. Porter, D. A., Easterling, K. E. & Sherif, M. Y. Phase transformations in metals and alloys, third edition. *Phase Transform. Met. Alloy. Third Ed.* 1–521 (2009).

26. Delaey, L. Diffusionless Transformations. in *Phase Transformations in Materials* 583–654 (Wiley-VCH Verlag GmbH & Co. KGaA, 2005). doi:10.1002/352760264X.ch9.

27. Christy, A. G. Multistage diffusionless pathways for reconstructive phase transitions: application to binary compounds and calcium carbonate. *Acta Crystallogr. Sect. B Struct. Sci.* **49**, 987–996 (1993).

28. Dmitriev, V. P., Tolédano, P., Torgashev, V. I. & Salje, E. K. H. Theory of reconstructive phase transitions between SiO2 polymorphs. *Phys. Rev. B* **58**, 11911–11921 (1998).

29. Matsuo, T. Encyclopedia of Supramolecular Chemistry, edited by JL Atwood & JW Steed. (2004).

30. Hilfer, R. Classification theory for anequilibrium phase transitions. *Phys. Rev. E* **48**, 2466–2475 (1993).

31. Van Roie, B. *et al.* Weakly first-order character of the nematic-isotropic phase transition in liquid crystals. *Phys. Rev. E* **72**, 041702 (2005).

32. Perrot, P. *A to Z of Thermodynamics*. (Oxford University Press on Demand, 1998).

33. Anisimov, M. P. Nucleation: theory and experiment. *Russ. Chem. Rev.* **72**, 591–628 (2003).

34. Moran, B., Chu, Y. A. & Olson, G. B. Homogeneous nucleation of a solid-solid dilatational phase transformation. *Int. J. Solids Struct.* **33**, 1903–1919 (1996).

35. White, M. A. Characterization of solid—solid phase transitions: Differential scanning calorimetry vs. adiabatic calorimetry. *Thermochim. Acta* **74**, 55–62 (1984).

36. Vives, E., Soto-Parra, D., Mañosa, L., Romero, R. & Planes, A. Imaging the dynamics of martensitic transitions using acoustic emission. *Phys. Rev. B* **84**, 060101 (2011).

37. Chen, J., Weidner, D. J., Parise, J. B., Vaughan, M. T. & Raterron, P. Observation of Cation Reordering during the Olivine-Spinel Transition in Fayalite by In Situ Synchrotron X-Ray Diffraction at High Pressure and Temperature. *Phys. Rev. Lett.* **86**, 4072–4075 (2001).

38. Burnley, P. C. & Green, H. W. Stress dependence of the mechanism of the olivine–spinel transformation. *Nature* **338**, 753–756 (1989).

39. Jacobs, K. Activation Volumes for Solid-Solid Transformations in Nanocrystals. *Science* **293**, 1803–1806 (2001).

40. Knudson, M. D., Desjarlais, M. P. & Dolan, D. H. Shock-Wave Exploration of the High-Pressure Phases of Carbon. *Science* **322**, 1822–1825 (2008).

41. Jayaraman, A. Diamond anvil cell and high-pressure physical investigations. *Rev. Mod. Phys.* **55**, 65–108 (1983).

42. Khaliullin, R. Z., Eshet, H., Kühne, T. D., Behler, J. & Parrinello, M. Nucleation mechanism for the direct graphite-to-diamond phase transition. *Nat. Mater.* **10**, 693–697 (2011).

43. Rao, M. & Sengupta, S. Nucleation of Solids in Solids: Ferrites and Martensites. *Phys. Rev. Lett.* **91**, 045502 (2003).

44. Li, B., Zhou, D. & Han, Y. Assembly and phase transitions of colloidal crystals. *Nat. Rev. Mater.* **1**, 15011 (2016).

45. Palberg, T. Crystallization kinetics of colloidal model suspensions: recent achievements and new perspectives. *J. Phys. Condens. Matter* **26**, 333101 (2014).

46. Alsayed, A. M. Premelting at Defects Within Bulk Colloidal Crystals. *Science* **309**, 1207–1210 (2005).

47. Wang, Z., Wang, F., Peng, Y., Zheng, Z. & Han, Y. Imaging the Homogeneous Nucleation During the Melting of Superheated Colloidal Crystals. *Science* **338**, 87–90 (2012).

48. Hunter, G. L. & Weeks, E. R. The physics of the colloidal glass transition. *Reports Prog. Phys.* **75**, 066501 (2012).

49. Weiss, J. A., Oxtoby, D. W., Grier, D. G. & Murray, C. A. Martensitic transition in a confined colloidal suspension. *J. Chem. Phys.* **103**, 1180–1190 (1995).

50. Casey, M. T. *et al.* Driving diffusionless transformations in colloidal crystals using DNA handshaking. *Nat. Commun.* **3**, 1209 (2012).

51. Yethiraj, A., Wouterse, A., Groh, B. & van Blaaderen, A. Nature of an Electric-Field-Induced Colloidal Martensitic Transition. *Phys. Rev. Lett.* **92**, 058301 (2004).

52. Nöjd, S., Mohanty, P. S., Bagheri, P., Yethiraj, A. & Schurtenberger, P. Electric field driven self-assembly of ionic microgels. *Soft Matter* **9**, 9199 (2013).

53. Peng, Y. *et al.* Two-step nucleation mechanism in solid-solid phase transitions. *Nat. Mater.* **14**, 101–108 (2015).

54. Yang, Y. *et al.* Phase transformations in binary colloidal monolayers. *Soft Matter* **11**, 2404–2415 (2015).

55. Mohanty, P. S., Bagheri, P., Nöjd, S., Yethiraj, A. & Schurtenberger, P. Multiple Path-Dependent Routes for Phase-Transition Kinetics in Thermoresponsive and Field-Responsive Ultrasoft Colloids. *Phys. Rev. X* **5**, 011030 (2015).

56. Peng, Y. *et al.* Diffusive and martensitic nucleation kinetics in solid-solid transitions of colloidal crystals. *Nat. Commun.* **8**, 1–12 (2017).

57. Hatch, D. M., Lookman, T., Saxena, A. & Stokes, H. T. Systematics of group-nonsubgroup transitions: Square to triangle transition. *Phys. Rev. B* **64**, 060104 (2001).

58. Henkel, M., Hinrichsen, H. & Lübeck, S. *Non-equilibrium phase transitions: volume 1: absorbing phase transitions.* (Springer Science & Business Media, 2008).

59. Tolédano, P. & Dmitriev, V. *Reconstructive Phase Transitions. Reconstructive phase transitions in crystals and quasicrystals* (World Scientific Publishing Co. Pte. Ltd., 1996). doi:10.1142/9789812830715.

60. Scandolo, S., Bernasconi, M., Chiarotti, G. L., Focher, P. & Tosatti, E. Pressure-Induced Transformation Path of Graphite to Diamond. *Phys. Rev. Lett.* **74**, 4015–4018 (1995).

61. Kadau, K. Microscopic View of Structural Phase Transitions Induced by Shock Waves. *Science* **296**, 1681–1684 (2002).

62. Toledano, P. & Toledano, J. *Landau Theory Of Phase Transitions, The: Application To Structural, Incommensurate, Magnetic And Liquid Crystal Systems.* vol. 3 (World Scientific Publishing Company, 1987).

63. Landau, L. D. & Lifshitz, E. M. Chapter i-the fundamental principles of statistical physics. *Course Theor. Phys.* 1–33 (1980).

64. Dove, M. T. Theory of displacive phase transitions in minerals. *Am. Mineral.* **82**, 213–244 (1997).

65. Boulfelfel, S. E. Atomic Scale Investigation of Pressure Induced Phase Transitions in the Solid State. (Technischen Universitat Dresden, 2009).

66. Alperin, J. L. *Local representation theory: Modular representations as an introduction to the local representation theory of finite groups.* (Cambridge University Press, 1993).

67. Catti, M. Orthorhombic Intermediate State in the Zinc Blende to Rocksalt Transformation Path of SiC at High Pressure. *Phys. Rev. Lett.* **87**, 035504 (2001).

68. Catti, M. Kinetic mechanisms of the pressure-driven phase transitions of AgI. *Phys. Rev. B - Condens. Matter Mater. Phys.* **72**, 1–7 (2005).

69. Catti, M. & Milano, U. Phase transitions with no group-subgroup relations between the phases. 21–27 (2009).

70. Martoňák, R., Laio, A. & Parrinello, M. Predicting Crystal Structures: The Parrinello-Rahman Method Revisited. *Phys. Rev. Lett.* **90**, 075503 (2003).

71. Barducci, A., Bonomi, M. & Parrinello, M. Alessandro Barducci, Massimiliano Bonomi and Michele Parrinello ∗. **1**, 826–843 (2011).

72. Zheng, S. & Pfaendtner, J. Enhanced sampling of chemical and biochemical reactions with metadynamics. *Mol. Simul.* **41**, 55–72 (2015).

73. Tiwary, P. & Parrinello, M. From Metadynamics to Dynamics. **230602**, 1–5 (2013).

74. Tiwary, P., Limongelli, V., Salvalaglio, M. & Parrinello, M. Kinetics of protein–ligand unbinding: Predicting pathways, rates, and rate-limiting steps. *Proc. Natl. Acad. Sci.* **112**, E386–E391 (2015).

75. Shang, C., Zhang, X. J. & Liu, Z. P. Stochastic surface walking method for crystal structure and phase transition pathway prediction. *Phys. Chem. Chem. Phys.* **16**, 17845–17856 (2014).

76. Huang, S. Da, Shang, C., Zhang, X. J. & Liu, Z. P. Material discovery by combining stochastic

surface walking global optimization with a neural network. *Chem. Sci.* **8**, 6327–6337 (2017).

77.   Stokes, H. T. & Hatch, D. M. Group-subgroup structural phase transitions: A comparison with existing tables. *Phys. Rev. B* **30**, 4962–4967 (1984).

78.   Sowa, H. & Koch, E. A proposal for a transition mechanism from the diamond to the lonsdaleite type. *Acta Crystallogr. Sect. A Found. Crystallogr.* **57**, 406–413 (2001).

79.   Laio, A. & Parrinello, M. Escaping free-energy minima. *Proc. Natl. Acad. Sci.* **99**, 12562–12566 (2002).

80.   Bolhuis, P. G., Chandler, D., Dellago, C. & Geissler, P. L. Transition Path Sampling: Throwing Ropes Over Rough Mountain Passes, in the Dark. 291–318 (2002) doi:10.1146/annurev.physchem.53.082301.113146.

81.   Dellago, C., Bolhuis, P. G. & Geissler, P. L. *Computer Simulations in Condensed Matter Systems: From Materials to Chemical Biology Volume 1. Lecture Notes in Physics* vol. 703 (2006).

82.   Boulfelfel, S. E., Seifert, G., Grin, Y. & Leoni, S. Squeezing lone pairs: The A17 to A7 pressure-induced phase transition in black phosphorus. *Phys. Rev. B* **85**, 014110 (2012).

83.   Li, B., Qian, G., Oganov, A. R., Boulfelfel, S. E. & Faller, R. Mechanism of the fcc-to-hcp phase transformation in solid Ar. *J. Chem. Phys.* **146**, 214502 (2017).

84.   Boulfelfel, S. E., Oganov, A. R. & Leoni, S. Understanding the nature of 'superhard graphite'. *Sci. Rep.* **2**, 1–15 (2012).

85.   Wales, D. J. Exploring Energy Landscapes. *Annu. Rev. Phys. Chem.* **69**, (2018).

86.   Wales, D. J. & Bogdan, T. V. Potential energy and free energy landscapes. *J. Phys. Chem. B* **110**, 20765–20776 (2006).

87.   Schlegel, H. B. Geometry optimization. *WIREs Comput. Mol. Sci.* **1**, 790–809 (2011).

88.   McQuarrie, D. A. *Statistical thermodynamics*. (Harper and Row, 1973).

89.   Heidrich, D. *The reaction path in chemistry: current approaches and perspectives*. vol. 16 (Springer Science & Business Media, 2013).

90.   Wilson, E. B., Decius, J. C. & Cross, P. C. *Molecular vibrations: the theory of infrared and Raman vibrational spectra*. (Courier Corporation, 1980).

91.   Eyring, H. The activated complex in chemical reactions. *J. Chem. Phys.* **3**, 63–71 (1935).

92.   Wigner, E. The transition state method. *Trans. Faraday Soc.* **34**, 29 (1938).

93.   Horiuti, J. On the Statistical Mechanical Treatment of the Absolute Rate of Chemical Reaction. *Bull. Chem. Soc. Jpn.* **13**, 210–216 (1938).

94.   Chandler, D. Statistical mechanics of isomerization dynamics in liquids and the transition state approximation. *J. Chem. Phys.* **68**, 2959 (1978).

95.   Henkelman, G. Atomistic Simulations of Activated Processes in Materials. *Annu. Rev. Mater. Res.* **47**, 199–216 (2017).

96.   Keck, J. C. Variational Theory of Reaction Rates. in vol. XIII 85–121 (2007).

97.   Voter, A. F. & Doll, J. D. Dynamical corrections to transition state theory for multistate systems: Surface self-diffusion in the rare-event regime. *J. Chem. Phys.* **82**, 80–92 (1985).

98.   Anderson, J. B. Statistical theories of chemical reactions. Distributions in the transition region. *J. Chem. Phys.* **58**, 4684–4692 (1973).

99.   Bennett, C. H. Molecular Dynamics and Transition State Theory: The Simulation of Infrequent Events. in 63–97 (1977). doi:10.1021/bk-1977-0046.ch004.

100.   Vineyard, G. H. Frequency factors and isotope effects in solid state rate processes. *J. Phys. Chem. Solids* **3**, 121–127 (1957).

101.   Cornish-Bowden, A. *Fundamentals of enzyme kinetics*. (John Wiley & Sons, 2013).

102.   Cramer, C. J. & Truhlar, D. G. Implicit Solvation Models: Equilibria, Structure, Spectra, and Dynamics. *Chem. Rev.* **99**, 2161–2200 (1999).

103.   Masel, R. I. *Principles of adsorption and reaction on solid surfaces*. vol. 3 (John Wiley & Sons, 1996).

104.   Cerjan, C. J. & Miller, W. H. On finding transition states. *J. Chem. Phys.* **75**, 2800–2806 (1981).

105. Doye, J. P. K. & Wales, D. J. Surveying a potential energy surface by eigenvector-following Applications to global optimisation and the structural transformations of clusters. *Zeitschrift Phys. D Atoms, Mol. Clust.* **40**, 194–197 (1997).

106. Dellago, C. & Bolhuis, P. G. *Transition path sampling.* vol. 123 (2002).

107. Frenkel, D. & Smit, B. Understanding Molecular Simulation (Computational Science Series, Vol 1). (2001).

108. Allen, M. P. & Tildesley, D. J. *Computer simulation of liquids.* (Oxford university press, 2017).

109. Car, R. & Parrinello, M. Unified Approach for Molecular Dynamics and Density-Functional Theory. *Phys. Rev. Lett.* **55**, 2471–2474 (1985).

110. Woodley, S. M. & Catlow, R. Crystal structure prediction from first principles. *Nat. Mater.* **7**, 937–946 (2008).

111. Wang, Y., Lv, J., Zhu, L. & Ma, Y. CALYPSO: A method for crystal structure prediction. *Comput. Phys. Commun.* **183**, 2063–2070 (2012).

112. Martoňák, R., Donadio, D., Oganov, A. R. & Parrinello, M. Crystal structure transformations in SiO2 from classical and ab initio metadynamics. *Nat. Mater.* **5**, 623–626 (2006).

113. Wales, D. J. Discrete path sampling. *Mol. Phys.* **100**, 3285–3305 (2002).

114. Middleton, T. F. & Wales, D. J. Energy landscapes of some model glass formers. *Phys. Rev. B* **64**, 024205 (2001).

115. Goedecker, S. Minima hopping: An efficient search method for the global minimum of the potential energy surface of complex molecular systems. *J. Chem. Phys.* **120**, 9911–9917 (2004).

116. Amsler, M. & Goedecker, S. Crystal structure prediction using the minima hopping method. *J. Chem. Phys.* **133**, (2010).

117. Oganov, A. R. & Glass, C. W. Crystal structure prediction using ab initio evolutionary techniques: Principles and applications. *J. Chem. Phys.* **124**, 1–15 (2006).

118. Glass, C. W., Oganov, A. R. & Hansen, N. USPEX-Evolutionary crystal structure prediction. *Comput. Phys. Commun.* **175**, 713–720 (2006).

119. Wang, Y., Lv, J., Zhu, L. & Ma, Y. Crystal structure prediction via particle-swarm optimization. *Phys. Rev. B* **82**, 094116 (2010).

120. Carr, J. M., Trygubenko, S. A. & Wales, D. J. Finding pathways between distant local minima. *J. Chem. Phys.* **122**, (2005).

121. Oganov, A. R., Lyakhov, A. O. & Valle, M. How evolutionary crystal structure prediction works-and why. *Acc. Chem. Res.* **44**, 227–237 (2011).

122. Pannetier, J., Bassas-Alsina, J., Rodriguez-Carvajal, J. & Caignaert, V. Prediction of crystal structures from crystal chemistry rules by simulated annealing. *Nature* **346**, 343–345 (1990).

123. Schön, J. C. & Jansen, M. First Step Towards Planning of Syntheses in Solid-State Chemistry: Determination of Promising Structure Candidates by Global Optimization. *Angew. Chemie Int. Ed. English* **35**, 1286–1304 (1996).

124. Schön, J. C. & Jansen, M. Determination, prediction, and understanding of structures, using the energy landscapes of chemical systems - Part I. *Zeitschrift für Krist. - Cryst. Mater.* **216**, (2001).

125. Schön, J. C. & Jansen, M. Determination, prediction, and understanding of structures, using the energy landscapes of chemical systems – Part II. *Zeitschrift für Krist. - Cryst. Mater.* **216**, (2001).

126. Wales, D. J. & Doye, J. P. K. Global Optimization by Basin-Hopping and the Lowest Energy Structures of Lennard-Jones Clusters Containing up to 110 Atoms. *J. Phys. Chem. A* **101**, 5111–5116 (1997).

127. Wang, H. *et al.* CALYPSO structure prediction method and its wide application. *Comput. Mater. Sci.* **112**, 406–415 (2016).

128. Wales, D. *Energy landscapes: Applications to clusters, biomolecules and glasses.* (Cambridge University Press, 2003).

129. Iannuzzi, M., Laio, A. & Parrinello, M. Efficient Exploration of Reactive Potential Energy Surfaces Using Car-Parrinello Molecular Dynamics. *Phys. Rev. Lett.* **90**, 238302 (2003).

130. Melchionna, S. Enhanced sampling of rare events. *Phys. Rev. E* **62**, 8762–8767 (2000).

131. Grubmüller, H. Predicting slow structural transitions in macromolecular systems: Conformational flooding. *Phys. Rev. E* **52**, 2893–2906 (1995).

132. Martoňák, R. *et al.* Simulation of structural phase transitions by metadynamics. *Zeitschrift fur Krist.* **220**, 489–498 (2005).

133. Zipoli, F., Bernasconi, M. & Martoňák, R. Constant pressure reactive molecular dynamics simulations of phase transitions under pressure: The graphite to diamond conversion revisited. *Eur. Phys. J. B* **39**, 41–47 (2004).

134. Gimondi, I. & Salvalaglio, M. CO_2 packing polymorphism under pressure: Mechanism and thermodynamics of the I-III polymorphic transition. *J. Chem. Phys.* **147**, 114502 (2017).

135. Rogal, J., Schneider, E. & Tuckerman, M. E. Neural-Network-Based Path Collective Variables for Enhanced Sampling of Phase Transformations. *Phys. Rev. Lett.* **123**, 245701 (2019).

136. Mendels, D., McCarty, J., Piaggi, P. M. & Parrinello, M. Searching for Entropically Stabilized Phases: The Case of Silver Iodide. *J. Phys. Chem. C* **122**, 1786–1790 (2018).

137. Badin, M. & Martoňák, R. Nucleating different coordination in crystal under pressure: Study of B1-B2 transition in NaCl by metadynamics. **d**, 1–7 (2021).

138. Martoňák, R. *et al.* Simulation of structural phase transitions by metadynamics. *Zeitschrift für Krist. - Cryst. Mater.* **220**, 489–498 (2005).

139. Bussi, G. & Laio, A. Using metadynamics to explore complex free-energy landscapes. *Nat. Rev. Phys.* **2**, 200–212 (2020).

140. Rosso, L., Mináry, P., Zhu, Z. & Tuckerman, M. E. On the use of the adiabatic molecular dynamics technique in the calculation of free energy profiles. *J. Chem. Phys.* **116**, 4389–4402 (2002).

141. Maragliano, L. & Vanden-Eijnden, E. A temperature accelerated method for sampling free energy and determining reaction pathways in rare events simulations. *Chem. Phys. Lett.* **426**, 168–175 (2006).

142. Voter, A. F. A method for accelerating the molecular dynamics simulation of infrequent events. *J. Chem. Phys.* **106**, 4665–4677 (1997).

143. Bealing, C., Martoňák, R. & Molteni, C. Pressure-induced structural phase transitions in CdSe: A metadynamics study. *J. Chem. Phys.* **130**, 124712 (2009).

144. Sun, J., Klug, D. D. & Martoňák, R. Structural transformations in carbon under extreme pressure: Beyond diamond. *J. Chem. Phys.* **130**, 194512 (2009).

145. Plašienka, D. & Martoňák, R. Transformation pathways in high-pressure solid nitrogen: From molecular N 2 to polymeric cg-N. *J. Chem. Phys.* **142**, 094505 (2015).

146. Schön, J. C., Putz, H. & Jansen, M. Studying the energy hypersurface of continuous systems - the threshold algorithm. *J. Phys. Condens. Matter* **8**, 143–156 (1996).

147. Henkelman, G. & Jónsson, H. A dimer method for finding saddle points on high dimensional potential surfaces using only first derivatives. *J. Chem. Phys.* **111**, 7010–7022 (1999).

148. Xiao, P. *et al.* Solid-state dimer method for calculating solid-solid phase transitions Solid-state dimer method for calculating solid-solid phase transitions. **174104**, 1–6 (2014).

149. Zimmerman, P. M. Single-ended transition state finding with the growing string method. *J. Comput. Chem.* **36**, 601–611 (2015).

150. Gillespie, D. T. Monte Carlo simulation of random walks with residence time dependent transition probability rates. *J. Comput. Phys.* **28**, 395–407 (1978).

151. Voter, A. F. Classically exact overlayer dynamics: Diffusion of rhodium clusters on Rh(100). *Phys. Rev. B* **34**, 6819–6829 (1986).

152. Fichthorn, K. A. & Weinberg, W. H. Theoretical foundations of dynamical Monte Carlo simulations. *J. Chem. Phys.* **95**, 1090–1096 (1991).

153. Voter, A. F. Hyperdynamics: Accelerated Molecular Dynamics of Infrequent Events. *Phys. Rev. Lett.* **78**, 3908–3911 (1997).

154. So/rensen, M. R. & Voter, A. F. Temperature-accelerated dynamics for simulation of infrequent events. *J. Chem. Phys.* **112**, 9599–9606 (2000).

155. Voter, A. F. Parallel replica method for dynamics of infrequent events. *Phys. Rev. B* **57**, R13985–R13988 (1998).

156. Quapp, W. & Bofill, J. M. A comment to the nudged elastic band method. *J. Comput. Chem.* **31**, 2526–2531 (2010).

157. Choi, C. & Elber, R. Reaction path study of helix formation in tetrapeptides: Effect of side chains. *J. Chem. Phys.* **94**, 751–760 (1991).

158. JÓNSSON, H., MILLS, G. & JACOBSEN, K. W. Nudged elastic band method for finding minimum energy paths of transitions. in *Classical and Quantum Dynamics in Condensed Phase Simulations* 385–404 (WORLD SCIENTIFIC, 1998). doi:10.1142/9789812839664_0016.

159. Heyden, A., Bell, A. T. & Keil, F. J. Efficient methods for finding transition states in chemical reactions: Comparison of improved dimer method and partitioned rational function optimization method. *J. Chem. Phys.* **123**, (2005).

160. E, W., Ren, W. & Vanden-Eijnden, E. String method for the study of rare events. *Phys. Rev. B* **66**, 052301 (2002).

161. Caspersen, K. J. & Carter, E. A. Finding transition states for crystalline solid-solid phase transformations. *Proc. Natl. Acad. Sci.* **102**, 6738–6743 (2005).

162. Sheppard, D., Xiao, P., Chemelewski, W., Johnson, D. D. & Henkelman, G. A generalized solid-state nudged elastic band method. *J. Chem. Phys.* **136**, 074103 (2012).

163. Qian, G. *et al.* Variable cell nudged elastic band method for studying solid–solid structural phase transitions. *Comput. Phys. Commun.* **184**, 2111–2118 (2013).

164. Blatov, V. A., Golov, A. A., Yang, C., Zeng, Q. & Kabanov, A. A. Network topological model of reconstructive solid-state transformations. *Sci. Rep.* **9**, 6007 (2019).

165. Passerone, D. & Parrinello, M. Action-Derived Molecular Dynamics in the Study of Rare Events. *Phys. Rev. Lett.* **87**, 108302 (2001).

166. Olender, R. & Elber, R. Calculation of classical trajectories with a very large time step: Formalism and numerical examples. *J. Chem. Phys.* **105**, 9299–9315 (1996).

167. Eastman, P., Grønbech-Jensen, N. & Doniach, S. Simulation of protein folding by reaction path annealing. *J. Chem. Phys.* **114**, 3823–3841 (2001).

168. Bolhuis, P. G., Chandler, D., Dellago, C. & Geissler, P. L. Transition Path Sampling: Throwing Ropes Over Rough Mountain Passes, in the Dark. *Annu. Rev. Phys. Chem.* **53**, 291–318 (2002).

169. Dellago, C. & Bolhuis, P. G. Transition Path Sampling and Other Advanced Simulation Techniques for Rare Events. in *Advanced Computer Simulation Approaches for Soft Matter Sciences III* vol. 54 167–233 (Springer Berlin Heidelberg, 2009).

170. Stevanović, V. *et al.* Predicting kinetics of polymorphic transformations from structure mapping and coordination analysis. *Phys. Rev. Mater.* **2**, 033802 (2018).

171. Therrien, F., Graf, P. & Stevanović, V. Matching crystal structures atom-to-atom. *J. Chem. Phys.* **152**, (2020).

172. Hart, G. L. W. & Forcade, R. W. Algorithm for generating derivative structures. *Phys. Rev. B - Condens. Matter Mater. Phys.* **77**, 1–12 (2008).

173. Křivý, I. & Gruber, B. A unified algorithm for determining the reduced (Niggli) cell. *Acta Crystallogr. Sect. A* **32**, 297–298 (1976).

174. Santoro, A. & Mighell, A. D. Determination of reduced cells. *Acta Crystallogr. Sect. A* **26**, 124–127 (1970).

175. Therrien, F. & Stevanović, V. Minimization of atomic displacements as a guiding principle of the martensitic phase transformation. *Phys. Rev. Lett.* **125**, 1–6 (2020).

176. Munkres, J. Algorithms for the Assignment and Transportation Problems. *J. Soc. Ind. Appl. Math.* **5**, 32–38 (1957).

177. Sadeghi, A. *et al.* Metrics for measuring distances in configuration spaces. *J. Chem. Phys.* **139**, (2013).

178. Lonie, D. C. & Zurek, E. Identifying duplicate crystal structures: XtalComp, an open-source solution. *Comput. Phys. Commun.* **183**, 690–697 (2012).

179. Yang, L., Dacek, S. & Ceder, G. Proposed definition of crystal substructure and substructural similarity. *Phys. Rev. B - Condens. Matter Mater. Phys.* **90**, 1–9 (2014).

180. Zhu, L. *et al.* A fingerprint based metric for measuring similarities of crystalline structures. *J. Chem. Phys.* **144**, (2016).

181. Munro, J. M. *et al.* Discovering minimum energy pathways via distortion symmetry groups. *Phys. Rev. B* **98**, 085107 (2018).

182. Wells, A. F. The geometrical basis of crystal chemistry. Part 1. *Acta Crystallogr.* **7**, 535–544 (1954).

183. Blatov, V. A. A method for topological analysis of rod packings. *Struct. Chem.* **27**, 1605–1611 (2016).

184. Blatov, V. A. A method for hierarchical comparative analysis of crystal structures. *Acta Crystallogr. Sect. A Found. Crystallogr.* **62**, 356–364 (2006).

185. O'Keeffe, M., Peskov, M. A., Ramsden, S. J. & Yaghi, O. M. The Reticular Chemistry Structure Resource (RCSR) Database of, and Symbols for, Crystal Nets. *Acc. Chem. Res.* **41**, 1782–1789 (2008).

186. Blatov, V. A., Alexandrov, E. V. & Shevchenko, A. P. Topology: ToposPro. in *Reference Module in Chemistry, Molecular Sciences and Chemical Engineering* 1–23 (Elsevier, 2019). doi:10.1016/B978-0-12-409547-2.14576-7.

187. Blatov, V. A. Topological relations between three-dimensional periodic nets. I. Uninodal nets. *Acta Crystallogr. Sect. A Found. Crystallogr.* **63**, 329–43 (2007).

188. Blatov, V. A. & Proserpio, D. M. Topological relations between three-periodic nets. II. Binodal nets. *Acta Crystallogr. Sect. A Found. Crystallogr.* **65**, 202–212 (2009).

189. Klee, W. E. Crystallographic nets and their quotient graphs. *Cryst. Res. Technol.* **39**, 959–968 (2004).

190. Muller, U. *Symmetry Relationships between Crystal Structures. International Union of Crystallography Book Series* (2013). doi:10.1093/acprof:oso/9780199669950.001.0001.

191. Blatov, V. A., Shevchenko, A. P. & Proserpio, D. M. Applied Topological Analysis of Crystal Structures with the Program Package ToposPro. *Cryst. Growth Des.* **14**, 3576–3586 (2014).

192. Pfrommer, B. G., Côté, M., Louie, S. G. & Cohen, M. L. Relaxation of Crystals with the Quasi-Newton Method. *J. Comput. Phys.* **131**, 233–240 (1997).

193. Wentzcovitch, R. M. Invariant molecular-dynamics approach to structural phase transitions. *Phys. Rev. B* **44**, 2358–2361 (1991).

194. Parrinello, M. & Rahman, A. Crystal Structure and Pair Potentials: A Molecular-Dynamics Study. *Phys. Rev. Lett.* **45**, 1196–1199 (1980).

195. Nielsen, O. H. & Martin, R. M. Quantum-mechanical theory of stress and force. *Phys. Rev. B* **32**, 3780–3791 (1985).

196. Martin, R. M. *Electronic Structure. Basic Theory and Practical Methods.* (Cambridge university press, 2004).

197. Henkelman, G., Uberuaga, B. P. & Jónsson, H. A climbing image nudged elastic band method for finding saddle points and minimum energy paths. *J. Chem. Phys.* **113**, 9901–9904 (2000).

198. Henkelman, G. & Jónsson, H. Improved tangent estimate in the nudged elastic band method for finding minimum energy paths and saddle points. *J. Chem. Phys.* **113**, 9978–9985 (2000).

199. Middleton, T. F. & Wales, D. J. Energy landscapes of model glasses. II. Results for constant pressure. *J. Chem. Phys.* **118**, 4583–4593 (2003).

200. Quapp, W. & Heidrich, D. Analysis of the concept of minimum energy path on the potential energy surface of chemically reacting systems. *Theor. Chim. Acta* **66**, 245–260 (1984).

201. Gale, J. D. GULP: A computer program for the symmetry-adapted simulation of solids. *J. Chem. Soc. Faraday Trans.* **93**, 629–637 (1997).

202. Giannozzi, P. *et al.* QUANTUM ESPRESSO: a modular and open-source software project for quantum simulations of materials. *J. Phys. Condens. Matter* **21**, 395502 (2009).

203. Giannozzi, P. *et al.* Advanced capabilities for materials modelling with Quantum ESPRESSO. *J. Phys. Condens. Matter* **29**, 465901 (2017).

204. Kresse, G. & Furthmüller, J. Efficient iterative schemes for ab initio total-energy calculations using a plane-wave basis set. *Phys. Rev. B* **54**, 11169–11186 (1996).

205. Sheppard, D., Terrell, R. & Henkelman, G. Optimization methods for finding minimum energy paths. *J. Chem. Phys.* **128**, 134106 (2008).

206. Hohenberg, P. & Kohn, W. Inhomogeneous Electron Gas. *Phys. Rev.* **136**, B864–B871 (1964).

207. Kohn, W. & Sham, L. J. Self-Consistent Equations Including Exchange and Correlation Effects. *Phys. Rev.* **140**, A1133–A1138 (1965).

208. Perdew, J. P., Burke, K. & Ernzerhof, M. Generalized Gradient Approximation Made Simple. *Phys. Rev. Lett.* **77**, 3865–3868 (1996).

209. Blöchl, P. E. Projector augmented-wave method. *Phys. Rev. B* **50**, 17953–17979 (1994).

210. Kresse, G. & Joubert, D. From ultrasoft pseudopotentials to the projector augmented-wave method. *Phys. Rev. B* **59**, 1758–1775 (1999).

211. Kresse, G. & Hafner, J. Ab initio molecular dynamics for liquid metals. *Phys. Rev. B* **47**, 558–561 (1993).

212. Kresse, G. & Hafner, J. Ab initio molecular-dynamics simulation of the liquid-metalamorphous- semiconductor transition in germanium. *Phys. Rev. B* **49**, 14251–14269 (1994).

213. Monkhorst, H. J. & Pack, J. D. Special points for Brillouin-zone integrations. *Phys. Rev. B* **13**, 5188–5192 (1976).

214. Bitzek, E., Koskinen, P., Gähler, F., Moseler, M. & Gumbsch, P. Structural relaxation made simple. *Phys. Rev. Lett.* **97**, 1–4 (2006).

215. Momma, K. & Izumi, F. VESTA 3 for three-dimensional visualization of crystal, volumetric and morphology data. *J. Appl. Crystallogr.* **44**, 1272–1276 (2011).

216. Liu, A. Y. & Cohen, M. L. Prediction of New Low Compressibility Solids. *Science* **245**, 841–842 (1989).

217. Niu, C., Lu, Y. Z. & Lieber, C. M. Experimental Realization of the Covalent Solid Carbon Nitride. *Science* **261**, 334–337 (1993).

218. Kvashnin, A. G., Oganov, A. R., Samtsevich, A. I. & Allahyari, Z. Computational Search for Novel Hard Chromium-Based Materials. *J. Phys. Chem. Lett.* **8**, 755–764 (2017).

219. Lyakhov, A. O. & Oganov, A. R. Evolutionary search for superhard materials: Methodology and applications to forms of carbon and TiO_2. *Phys. Rev. B - Condens. Matter Mater. Phys.* **84**, 2–5 (2011).

220. Niu, H. *et al.* Structure, bonding, and possible superhardness of CrB_4. *Phys. Rev. B* **85**, 144116 (2012).

221. Zhong, M.-M., Huang, C. & Tian, C.-L. The structural stabilities, mechanical properties and hardness of chromium tetraboride: Compared with low-B borides. *Int. J. Mod. Phys. B* **30**, 1650201 (2016).

222. Zhao, Z. *et al.* Potentially superhard hcp CrN_2 compound studied at high pressure. *Phys. Rev. B* **93**, 214104 (2016).

223. Cheng, F., Wang, Y. & Yang, T. Microstructure and wear properties of Fe–VC–Cr_7C_3 composite coating on surface of cast steel. *Mater. Charact.* **59**, 488–492 (2008).

224. Kok, Y. N. & Hovsepian, P. E. Resistance of nanoscale multilayer C/Cr coatings against environmental attack. *Surf. Coatings Technol.* **201**, 3596–3605 (2006).

225. Berg, G., Friedrich, C., Broszeit, E. & Berger, C. Development of chromium nitride coatings substituting titanium nitride. *Surf. Coatings Technol.* **86–87**, 184–191 (1996).

226. Navinšek, B., Panjan, P. & Milošev, I. Industrial applications of CrN (PVD) coatings, deposited at high and low temperatures. *Surf. Coatings Technol.* **97**, 182–191 (1997).

227. Mayrhofer, P. ., Willmann, H. & Mitterer, C. Oxidation kinetics of sputtered Cr–N hard coatings. *Surf. Coatings Technol.* **146–147**, 222–228 (2001).

228. Čekada, M., Panjan, P., Maček, M. & Šmíd, P. Comparison of structural and chemical

properties of Cr-based hard coatings. *Surf. Coatings Technol.* **151–152**, 31–35 (2002).

229. Reiter, A. E., Derflinger, V. H., Hanselmann, B., Bachmann, T. & Sartory, B. Investigation of the properties of Al1−xCrxN coatings prepared by cathodic arc evaporation. *Surf. Coatings Technol.* **200**, 2114–2122 (2005).

230. Hasegawa, M. & Yagi, T. Systematic study of formation and crystal structure of 3d-transition metal nitrides synthesized in a supercritical nitrogen fluid under 10 GPa and 1800K using diamond anvil cell and YAG laser heating. *J. Alloys Compd.* **403**, 131–142 (2005).

231. Rivadulla, F. *et al.* Reduction of the bulk modulus at high pressure in CrN. *Nat. Mater.* **8**, 947–951 (2009).

232. Corliss, L. M., Elliott, N. & Hastings, J. M. Antiferromagnetic Structure of CrN. *Phys. Rev.* **117**, 929–935 (1960).

233. Wang, S. *et al.* Experimental invalidation of phase-transition-induced elastic softening in CrN. *Phys. Rev. B* **86**, 064111 (2012).

234. Zhang, X. Y., Chawla, J. S., Deng, R. P. & Gall, D. Epitaxial suppression of the metal-insulator transition in CrN. *Phys. Rev. B* **84**, 073101 (2011).

235. Filippetti, A. & Hill, N. A. Magnetic Stress as a Driving Force of Structural Distortions: The Case of CrN. *Phys. Rev. Lett.* **85**, 5166–5169 (2000).

236. Alling, B., Marten, T. & Abrikosov, I. A. Questionable collapse of the bulk modulus in CrN. *Nat. Mater.* **9**, 283–284 (2010).

237. Alling, B., Marten, T. & Abrikosov, I. A. Effect of magnetic disorder and strong electron correlations on the thermodynamics of CrN. *Phys. Rev. B* **82**, 184430 (2010).

238. Herwadkar, A. & Lambrecht, W. R. L. Electronic structure of CrN: A borderline Mott insulator. *Phys. Rev. B* **79**, 035125 (2009).

239. Hones, P., Sanjines, R. & Levy, F. Characterization of sputter-deposited chromium nitride thin films for hard coatings. *Surf. Coatings Technol.* **94–95**, 398–402 (1997).

240. Tricoteaux, A., Jouan, P. Y., Guerin, J. D., Martinez, J. & Djouadi, A. Fretting wear properties of CrN and Cr2N coatings. *Surf. Coatings Technol.* **174–175**, 440–443 (2003).

241. Lin, J., Sproul, W. D., Moore, J. J., Lee, S. & Myers, S. High rate deposition of thick CrN and Cr2N coatings using modulated pulse power (MPP) magnetron sputtering. *Surf. Coatings Technol.* **205**, 3226–3234 (2011).

242. Qi, Z. B. *et al.* A comparative study of the oxidation behavior of Cr2N and CrN coatings. *Thin Solid Films* **544**, 515–520 (2013).

243. Kim, S.-J., Marquart, T. & Franzen, H. F. Structure refinement for Cr2N. *J. less-common Met.* **158**, L9–L10 (1990).

244. Eriksson, S. X-Ray Investigation of the System Iron-Chromium-Nitrogen. *Jernkontorets Ann.* **118**, 530 (1934).

245. Yan, M. F. & Chen, H. T. Structural, elastic and electronic properties of Cr2N: A first-principles study. *Comput. Mater. Sci.* **88**, 81–85 (2014).

246. Chase Jr, M. W. JANAF thermochemical table. *J. Phys. Chem. Ref. Data* **14**, Supplement--No (1985).

247. Aguas, M. D., Nartowski, A. M., Parkin, I. P., MacKenzie, M. & Craven, A. J. Chromium nitrides (CrN, Cr2N) from solid state metathesis reactions: effects of dilution and nitriding reagent. *J. Mater. Chem.* **8**, 1875–1880 (1998).

248. Scanavino, I. & Prencipe, M. Ab initio determination of the bulk modulus of the chromium nitride CrN. *RSC Adv.* **3**, 17813 (2013).

249. Bundy, F. P. *et al.* The pressure-temperature phase and transformation diagram for carbon; updated through 1994. *Carbon N. Y.* **34**, 141–153 (1996).

250. Field, J. E. & Field, J. E. *Properties of natural and synthetic diamond.* (Academic Press, 1992).

251. Lin, Y. *et al.* Amorphous Diamond: A High-Pressure Superhard Carbon Allotrope. *Phys. Rev. Lett.* **107**, 175504 (2011).

252. Blank, V. D. *et al.* High-pressure polymerized phases of C60. *Carbon N. Y.* **36**, 319–343 (1998).

253. Powles, R. C., Marks, N. A., Lau, D. W. M., McCulloch, D. G. & McKenzie, D. R. An energy

landscape for carbon network solids. *Carbon N. Y.* **63**, 416–422 (2013).

254. Skorodumova, N. V. Stability of the $MgCO_3$ structures under lower mantle conditions. *Am. Mineral.* **90**, 1008–1011 (2005).

255. Oganov, A. R., Glass, C. W. & Ono, S. High-pressure phases of $CaCO_3$: Crystal structure prediction and experiment. *Earth Planet. Sci. Lett.* **241**, 95–103 (2006).

256. Arapan, S., Souza de Almeida, J. & Ahuja, R. Formation of sp^3 Hybridized Bonds and Stability of $CaCO_3$ at Very High Pressure. *Phys. Rev. Lett.* **98**, 268501 (2007).

257. Oganov, A. R., Ono, S., Ma, Y., Glass, C. W. & Garcia, A. Novel high-pressure structures of $MgCO_3$, $CaCO_3$ and CO_2 and their role in Earth's lower mantle. *Earth Planet. Sci. Lett.* **273**, 38–47 (2008).

258. Pickard, C. J. & Needs, R. J. Structures and stability of calcium and magnesium carbonates at mantle pressures. *Phys. Rev. B - Condens. Matter Mater. Phys.* **91**, 1–8 (2015).

259. Lobanov, S. S. *et al.* Raman spectroscopy and x-ray diffraction of sp3 CaCO3 at lower mantle pressures. *Phys. Rev. B* **96**, 104101 (2017).

260. Martinez, I., Zhang, J. & Reeder, R. J. In situ X-ray diffraction of aragonite and dolomite at high pressure and high temperature; evidence for dolomite breakdown to aragonite and magnesite. *Am. Mineral.* **81**, 611–624 (1996).

261. Sato, K. & Katsura, T. Experimental investigation on dolomite dissociation into aragonite+magnesite up to 8.5 GPa. *Earth Planet. Sci. Lett.* **184**, 529–534 (2001).

262. Catalli, K. A high-pressure phase transition of calcite-III. *Am. Mineral.* **90**, 1679–1682 (2005).

263. Merlini, M., Hanfland, M. & Crichton, W. A. $CaCO_3$-III and $CaCO_3$-VI, high-pressure polymorphs of calcite: Possible host structures for carbon in the Earth's mantle. *Earth Planet. Sci. Lett.* **333**–**334**, 265–271 (2012).

264. Pippinger, T. *et al.* Puzzling calcite-III dimorphism: crystallography, high-pressure behavior, and pathway of single-crystal transitions. *Phys. Chem. Miner.* **42**, 29–43 (2015).

265. Ono, S. Post-aragonite phase transformation in CaCO3 at 40 GPa. *Am. Mineral.* **90**, 667–671 (2005).

266. Ono, S., Kikegawa, T. & Ohishi, Y. High-pressure transition of $CaCO_3$. *Am. Mineral.* **92**, 1246–1249 (2007).

267. Hu, C.-H. *et al.* Pressure-Induced Stabilization and Insulator-Superconductor Transition of BH. *Phys. Rev. Lett.* **110**, 165504 (2013).

268. Itoh, H., Matsudaira, T., Naka, S., Hamamoto, H. & Obayashi, M. Formation process of tungsten borides by solid state reaction between tungsten and amorphous boron. *J. Mater. Sci.* **22**, 2811–2815 (1987).

269. Gu, Q., Krauss, G. & Steurer, W. Transition Metal Borides: Superhard versus Ultra-incompressible. *Adv. Mater.* **20**, 3620–3626 (2008).

270. Zhao, E., Meng, J., Ma, Y. & Wu, Z. Phase stability and mechanical properties of tungsten borides from first principles calculations. *Phys. Chem. Chem. Phys.* **12**, 13158 (2010).

271. Mohammadi, R. *et al.* Tungsten tetraboride, an inexpensive superhard material. *Proc. Natl. Acad. Sci.* **108**, 10958–10962 (2011).

272. Aydin, S., Ciftci, Y. O. & Tatar, A. Superhard transition metal tetranitrides: XN_4 (X = Re, Os, W). *J. Mater. Res.* **27**, 1705–1715 (2012).

273. Cheng, X.-Y., Chen, X.-Q., Li, D.-Z. & Li, Y.-Y. Computational materials discovery: the case of the W–B system. *Acta Crystallogr. Sect. C Struct. Chem.* **70**, 85–103 (2014).

274. Kvashnin, A. G. *et al.* New Tungsten Borides, Their Stability and Outstanding Mechanical Properties. *J. Phys. Chem. Lett.* **9**, 3470–3477 (2018).

275. Kiessling, R., Wetterholm, A., Sillén, L. G., Linnasalmi, A. & Laukkanen, P. The Crystal Structures of Molybdenum and Tungsten Borides. *Acta Chem. Scand.* **1**, 893–916 (1947).

276. Okada, S., Kudou, K. & Lundström, T. Preparations and Some Properties of W_2B, δ-WB and WB_2 Crystals from High-Temperature Metal Solutions. *Jpn. J. Appl. Phys.* **34**, 226–231 (1995).

277. Gromilov, S. A., Kinelovskii, S. A., Alekseev, A. V. & Kirienko, I. B. Investigation of W_2B

and β-WB high-temperature phases in coatings produced by a shaped charge explosion. *J. Struct. Chem.* **51**, 1126–1131 (2010).

278. Duschanek, H. & Rogl, P. Critical assessment and thermodynamic calculation of the binary system boron-tungsten (B-W). *J. Phase Equilibria* **16**, 150–161 (1995).

279. Kvashnin, A. G. & Samtsevich, A. I. Phase Transitions in Tungsten Monoborides. *JETP Lett.* **111**, 343–349 (2020).

280. Zhao, C. *et al.* Unexpected stable phases of tungsten borides. *Phys. Chem. Chem. Phys.* **20**, 24665–24670 (2018).

281. Duschanek, H. & Rogl, P. Critical assessment and thermodynamic calculation of the binary system boron-tungsten (B-W). *J. Phase Equilibria* **16**, 150–161 (1995).

282. Schmidt, M. W., Poli, S., Comodi, P. & Zanazzi, P. F. High-pressure behavior of kyanite: Decomposition of kyanite into stishovite and corundum. *Am. Mineral.* **82**, 460–466 (1997).

283. Harben, P. W. *The industrial minerals handbook: a guide to markets, specifications and prices. Arby Industrial Minerals Division Metal Bull. PLC London* (2002).

284. McMichael, B. Aluminosilicate minerals. Refractories steel the Show. *Ind. Miner.* 27–43 (1990).

285. Skoog, A. J. & Moore, R. E. Refractory of the past for the future: mullite and its use as a bonding phase. *Am. Ceram. Soc. Bull.* **67**, 1180–1185 (1988).

286. Aryal, S., Rulis, P. & Ching, W. Y. Density functional calculations of the electronic structure and optical properties of aluminosilicate polymorphs (Al_2SiO_5). *Am. Mineral.* **93**, 114–123 (2008).

287. Zhang, W., Meng, Q. & Dai, W. Research on application of kyanite in plastic refractory. *Chinese J. Geochemistry* **32**, 326–330 (2013).

288. Belogurova, O. A. & Grishin, N. N. Carbidized heat insulation materials from kyanite ore. *Refract. Ind. Ceram.* **53**, 26–30 (2012).

289. Schneider, H., Schreuer, J. & Hildmann, B. Structure and properties of mullite—A review. *J. Eur. Ceram. Soc.* **28**, 329–344 (2008).

290. Schneider, H. & Komarneni, S. Basic properties of mullite. in *Mullite* 141–155 (Wiley Online Library, 2005).

291. Ohuchi, F. S., Ghose, S., Engelhard, M. H. & Baer, D. R. Chemical bonding and electronic structures of the Al_2SiO_5 polymorphs, andalusite, sillimanite, and kyanite: X-ray photoelectron-and electron energy loss spectroscopy studies. *Am. Mineral.* **91**, 740–746 (2006).

292. Burnham, C. W. Refinement of the crystal structure of sillimanite. *Zeitschrift für Krist.* **118**, 127–148 (1963).

293. Yang, H., Hazen, R. M., Finger, L. W., Prewitt, C. T. & Downs, R. T. Compressibility and crystal structure of sillimanite, Al_2SiO_5, at high pressure. *Phys. Chem. Miner.* **25**, 39–47 (1997).

294. Yang, H., Downs, R. T., Finger, L. W., Hazen, R. M. & Prewitt, C. T. Compressibility and crystal structure of kyanite, Al_2SiO_5, at high pressure. *Am. Mineral.* **82**, 467–474 (1997).

295. Klein, C. & Hurlbut, C. *Manual of mineralogy (by James D. Dana).* (John Wiley Sons, Inc., NY, 1995).

296. Whitney, D. L. Coexisting andalusite, kyanite, and sillimanite: Sequential formation of three Al_2SiO_5 polymorphs during progressive metamorphism near the triple point, Sivrihisar, Turkey. *Am. Mineral.* **87**, 405–416 (2002).

297. Atherton, M. P. & Brotherton, M. S. Metamorphyic index minerals in the Eastern Dalradian. *Scottish J. Geol.* **9**, 321–324 (1974).

298. Kerrick, D. M. *The Al_2SiO_5 polymorphs.* vol. 22 (Walter de Gruyter GmbH \& Co KG, 2018).

299. Oganov, A. R., Price, G. D. & Brodholt, J. P. Theoretical investigation of metastable Al_2SIO_5 polymomorphs. *Acta Crystallogr. Sect. A Found. Crystallogr.* **57**, 548–557 (2001).

300. Evans, B. W. & Berti, J. W. Revised metamorphic history for the Chiwaukum Schist, North Cascades, Washington. *Geology* **14**, 695 (1986).

301. Lux, D. R., DeYoreo, J. J., Guldotti, C. V. & Decker, E. R. Role of plutonism in low-pressure metamorphic belt formation. *Nature* **323**, 794–797 (1986).

302. Pattison, D. R. M., Tracy, R. J. & Kerrick, D. M. Contact metamorphism. in *Contact Metamorphism* vol. 26 105–206 (1991).

303. Sepahi, A. A., Whitney, D. L. & Baharifar, A. A. Petrogenesis of andalusite-kyanite-sillimanite veins and host rocks, Sanandaj-Sirjan metamorphic belt, Hamadan, Iran. *J. Metamorph. Geol.* **22**, 119–134 (2004).

304. Gervais, F. Three modes of isograd formation in the northern Monashee Complex of the Canadian Cordillera. *Geol. Soc. London, Spec. Publ.* **478**, 373–388 (2019).

305. Hiroi, Y., Kishi, S., Nohara, T., Sato, K. & Goto, J. Cretaceous high-temperature rapid loading and unloading in the Abukuma metamorphic terrane, Japan. *J. Metamorph. Geol.* **16**, 67–81 (1998).

306. Palin, R. M., Searle, M. P., Waters, D. J., Horstwood, M. S. A. & Parrish, R. R. Combined thermobarometry and geochronology of peraluminous metapelites from the Karakoram metamorphic complex, North Pakistan; New insight into the tectonothermal evolution of the Baltoro and Hunza Valley regions. *J. Metamorph. Geol.* **30**, 793–820 (2012).

307. Gibson, G. M., Peljo, M. & Chamberlain, T. Evidence and timing of crustal extension versus shortening in the early tectonothermal evolution of a Proterozoic continental rift sequence at Broken Hill, Australia. *Tectonics* **23**, TC5012 (2004).

308. Baharfar, A.-A., Whitney, D. L., Pang, K.-N., Chung, S.-L. & Iizuka, Y. Petrology, geothermobarometry, and P-T path of spinel-bearing symplectite migmatites from the Simin area, Hamedan, Sanandaj-Sirjan Zone, Iran. *Turkish J. Earth Sci.* **28**, 275–298 (2019).

309. Ali, A. The tectono-metamorphic evolution of the Balcooma Metamorphic Group, north-eastern Australia: A multidisciplinary approach. *J. Metamorph. Geol.* **28**, 397–422 (2010).

310. Allaz, J., Maeder, X., Vannay, J. C. & Steck, A. Formation of aluminosilicate-bearing quartz veins in the Simano nappe (Central Alps): Structural, thermobarometric and oxygen isotope constraints. *Schweizerische Mineral. und Petrogr. Mitteilungen* **85**, 191–214 (2005).

311. Likhanov, I. I., Reverdatto, V. V., Kozlov, P. S. & Popov, N. V. Kyanite–sillimanite metamorphism of the Precambrian complexes, Transangarian region of the Yenisei Ridge. *Russ. Geol. Geophys.* **50**, 1034–1051 (2009).

312. Kim, H. S. & Ree, J. H. P-T modeling of kyanite and sillimanite paramorphs growth after andalusite in late Paleozoic Pyeongan Supergroup, South Korea: Implication for metamorphism during the Mesozoic tectonic evolution. *Lithos* **118**, 269–286 (2010).

313. Sayab, M. Decompression through clockwise P-T path: implications for early N-S shortening orogenesis in the Mesoproterozoic Mt Isa Inlier (NE Australia). *J. Metamorph. Geol.* **24**, 89–105 (2006).

314. Whitney, D. L. & Samuelson, W. J. Crystallization sequences of coexisting andalusite, kyanite, and sillimanite, and a report on a new locality: Lesjaverk, Norway. *Eur. J. Mineral.* **31**, 731–737 (2019).

315. Hietanen, A. Kyanite, andalusite and sillimanite in the schist in Boels Butte quadrangle, Idaho. **41**, 1–27 (1956).

316. Carey, J. W., Rice, J. M. & Grover, T. W. Petrology of aluminous schist in the Boehls Butte region of northern Idaho; geologic history and aluminum-silicate phase relations. *Am. J. Sci.* **292**, 455–473 (1992).

317. Grover, T. W., Rice, J. M. & Carey, J. W. Petrology of aluminous schist in the Boehls Butte region of northern Idaho; phase equilibria and P-T evolution. *Am. J. Sci.* **292**, 474–507 (1992).

318. Garcia-Casco, A. & Torres-Roldan, R. L. Disequilibrium Induced by Fast Decompression in St−Bt−Grt−Ky−Sil−And Metapelites from the Betic Belt (Southern Spain). *J. Petrol.* **37**, 1207–1239 (1996).

319. Ralph, R. L., Finger, L. W., Hazen, R. M. & Ghose, S. Compressibility and crystal structure of andalusite at high pressure. *Am. Mineral.* **69**, 513–519 (1984).

320. Oganov, A. R. & Brodholt, J. P. High-pressure phases in the Al_2SiO_5 system and the problem

of aluminous phase in the Earth's lower mantle: ab initio calculations. *Phys. Chem. Miner.* **27**, 430–439 (2000).

321. Hoppe, R. Effective coordination numbers (ECoN) and mean fictive ionic radii (MEFIR). *Zeitschrift für Krist. - Cryst. Mater.* **150**, 23–52 (1979).

322. Hoppe, R. *et al.* A new route to charge distributions in ionic solids. *J. Less-Common Met.* **156**, 105–122 (1989).